SP-1311

ADM-Aeolus

Science Report

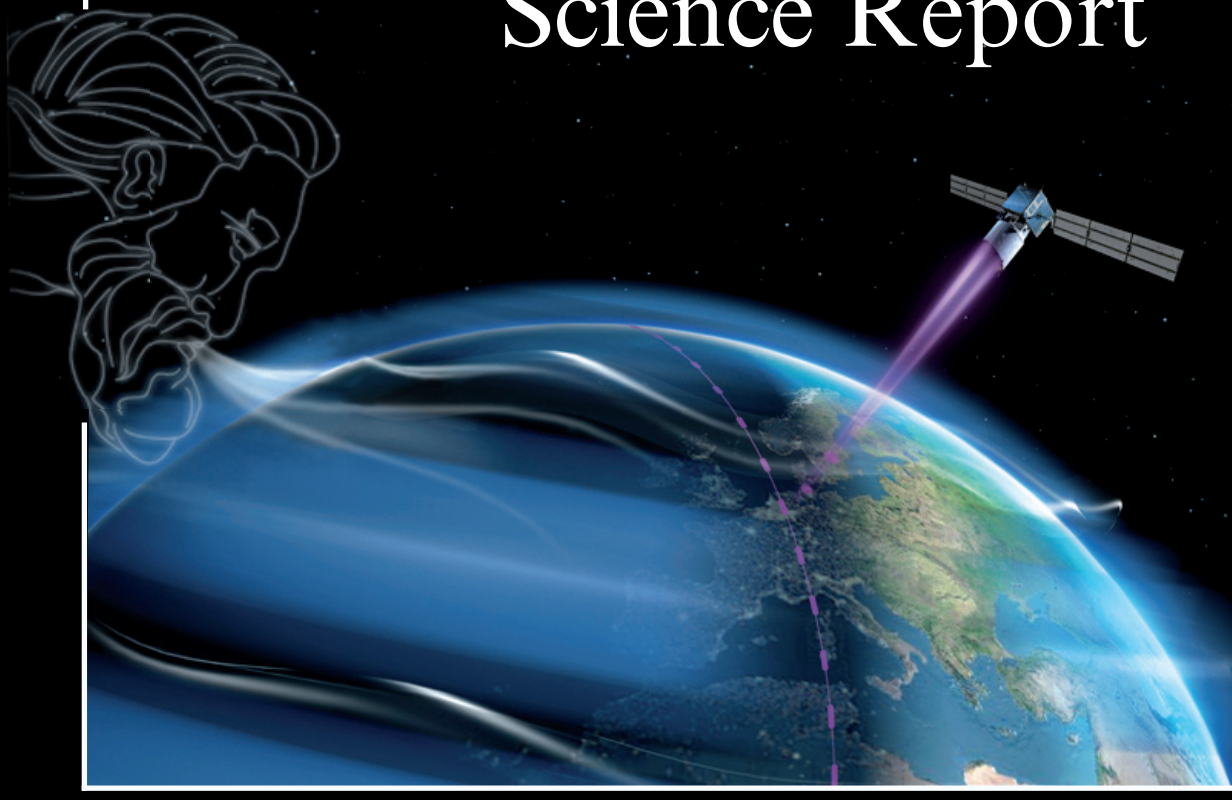

European Space Agency
Agence spatiale européenne

SP-1311
April 2008

ADM-Aeolus
Science Report

European Space Agency
Agence spatiale européenne

The contributions of the following persons are gratefully acknowledged:

Writing team
Erik Andersson
Alain Dabas
Martin Endemann
Paul Ingmann
Erland Källén
Dave Offiler
Ad Stoffelen

Review team
Paul Ingmann
Anne Grete Straume-Lindner

ADM-Aeolus Mission Advisory Group
Erik Andersson
Alain Dabas
Pierre Flamant
Michael Hardesty
Erland Källén
Paul Menzel
Dave Offiler
Oliver Reitebuch
Lars-Peter Riishøjgaard
Harald Schyberg
Ad Stoffelen
J. Michael Vaughan
Werner Wergen
James G. Yoe

Publication:	SP-1311, 'ADM-Aeolus' April 2008 ISBN 978-92-9221-404-3 ISSN 0379-6566
Coordinated by:	Paul Ingmann, Mission Science Division, Atmospheric Unit
Published by:	ESA Communication Production Office ESTEC, PO Box 299 2200 AG Noordwijk The Netherlands
Editor:	Peter Clissold
Design and Layout:	Rory van Haarlem
Copyright:	© 2008 ESA

Printed in The Netherlands

Contents

Foreword

The European Space Agency has been dedicated to observing the Earth from space since the launch of its first meteorological mission, Meteosat, in 1977. Following the success of this first mission, the subsequent series of Meteosat satellites, together with ERS-1, ERS-2, Envisat, and MetOp, have provided a wealth of valuable data characterising meteorological conditions as well as the Earth's climate and changing environment.

ESA's Living Planet Programme (*http://www.esa.int/livingplanet*) has subsequently established the framework for the development of science-driven Earth Explorer missions. The Earth Explorers are designed to address critical and specific issues that are raised by the science community, while at the same time demonstrating breakthrough technology in observing techniques.

The first European satellite-based wind LIDAR (Light Detection and Ranging) concepts were developed by the Doppler lidar working group. These preparatory activities, including theoretical studies, technical developments and field campaigns, are described in the ESA "*Report for Mission Selection*" (ESA SP-1233(4)). This report was presented to the Earth Observation community at the Earth Explorer User Consultation Meeting in 1999, after which the ADM-Aeolus wind mission was selected by ESA for implementation as the second Earth Explorer core mission.

ADM-Aeolus will demonstrate the capability of a spaceborne high spectral resolution Doppler wind lidar to make accurate global measurements of vertical wind profiles in the troposphere and the lower stratosphere (0–30 km). The mission thus addresses one of the main identified deficiencies of the current Global Observing System. Additional geophysical products that will be retrieved from the Aeolus measurements are cloud and aerosol optical properties. The technical pre-development started in 2000 and, with the signature of the industrial development contract in 2002, the project entered its implementation phase. The critical design review was completed in September 2005.

Both scientific studies and campaign activities are being performed in parallel to the technical and data processing development, including the optimisation of the ADM-Aeolus operational parameters. In particular, ongoing scientific activities have led to new in-depth insight into the benefits of the ADM-Aeolus mission for numerical weather prediction and climate research. Thus, it is an opportune moment to release this dedicated ADM-Aeolus Science Report as an update the 1999 Report for Mission Selection in a form that reflects these latest scientific findings and developments.

This report has been prepared by the Mission Science Division, with contributions from members of the ADM-Aeolus Mission Advisory group. The scientific coordination was performed by the ADM-Aeolus Mission Scientist in close cooperation with the ADM-Aeolus Project.

Volker Liebig
Director, Earth Observation Programmes

1. Introduction

1.1 The roots

Although it is known that the Egyptians and other early cultures took great steps to understand the signs from the sky, the first attempts at using science as a tool in weather forecasting probably date back to the Greeks. In Greek philosophical literature, Aristotle (384–322 BC) made the greatest progress in describing and explaining the nature of the wind. The methods were deductive, based upon Presocratic[1] writings and his own observations. Aristotle wrote a treatise called '*De Meteorologica*', dealing with the "*study of things lifted up*". It was a collection of writings that attempted to explain everything to do with the natural Earth, including the weather. About one third of the treatise is devoted to atmospheric phenomena and it is from this work that the modern term 'meteorology' is derived.

Aristotle rejected the Presocratic view that wind is air, for the same air persists both when it is in motion and when it is still. His understanding of wind was that it is caused by 'dry exhalation' and rain by 'moist exhalation' (or evaporation). They both have a birth and a death, like a living thing, caused by the sun and the moon. The Aristotelian wind rose, explained at length in '*De Meteorologica*', was used as a model for all other wind roses of antiquity. It uses a duodecimal classification of the winds; being based on the directional points N, NNE, NE, ENE, E, and so forth, although the duodecimal classification of the winds seems to be of Babylonian origin. Aristotle makes reference to the twelve children of Aeolus in *The Odyssey* written by Homer in about 800 BC (Book X):

> *"Thence we went on to the Aeoli island where lives Aeolus, son of Hippotas, dear to the immortal gods. It is an island that floats (as it were) upon the sea, iron bound with a wall that girds it. Now, Aeolus has six daughters and six lusty sons, so he made the sons marry the daughters, and they all live with their dear father and mother, feasting and enjoying every conceivable kind of luxury…"*

Meteorology has developed a lot from these ancient roots to the creation of the World Meteorological Organisation (WMO), which started as the International Meteorological Organisation in 1873 and now has over 180 members and three main centres in Melbourne, Washington and Moscow. This body sets global standards for procedures and weather-related agreements. Its members collect information from ground-based measurement stations located all over the world, and from many satellites. Members of WMO produce maps and forecasts at least every 6h and these are distributed across the world.

1.2 The challenge

Together with temperature, pressure, and humidity, wind is one of the basic variables describing the state of the atmosphere. Wind speed and direction observations are needed in support of weather forecasts and for the prediction of long-term climate change. Improved knowledge of the global wind field is widely recognised as fundamental to advancing the understanding and prediction of weather and climate. Winds profiles are measured by ground-based networks, but due to the limited coverage (mostly Northern Hemisphere extra-tropics) measurements by satellite are essential to get a more uniform global coverage. The possibility to measure global wind profiles from space was studied using various techniques. It was finally concluded that only an active optical system (lidar) could provide data of the required accuracy globally. This basic concept was first studied by NASA in the 1980s (e.g. NASA 1987, Baker *et al.*, 1995), leading to the Laser Atmospheric Wind Sounder (LAWS) concept. The starting point was that wind vectors had to be provided to make the observations

[1] i.e. the philosophers 'before Socrates'

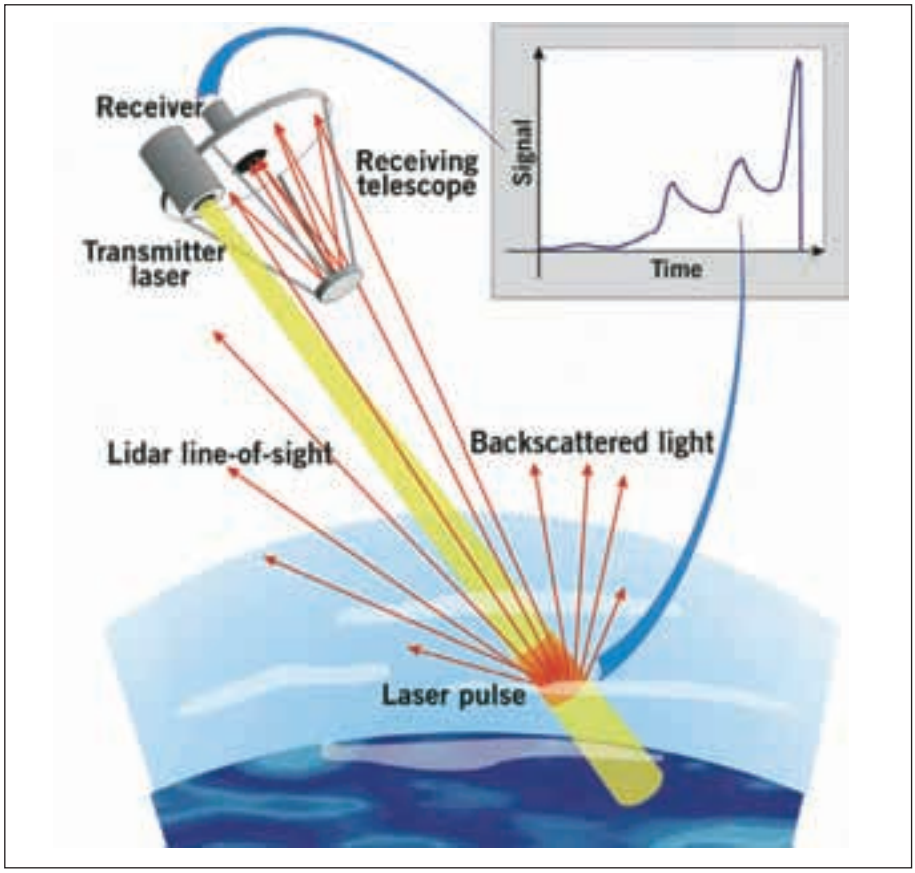

Fig. 1.1. Doppler wind lidar principle - the lidar emits a laser pulse towards the atmosphere, then collects, samples, and retrieves the frequency of the backscattered signal. As shown on the right-hand panel, the signal is backscattered from clouds, aerosols, molecules and the Earth's surface. The lidar measures the wind projection along the laser line-of-sight, using a slant angle off nadir.

beneficial for Numerical Weather Prediction (NWP). European scientists started from similar ideas (e.g. BEST, Bilan Energétique du Système Tropical, CNES 1988), but it soon became obvious that the LAWS concept would be extremely difficult to build and to launch into space. In parallel, scientific studies were performed assessing the impact of Doppler Wind Lidar (DWL) observations in data assimilation systems widely used for NWP. The results of a study conducted by Meteo France (Courtier *et al.*, 1992) and the UK Met Office (Lorenc *et al.*, 1992) supported the basic idea that a wind lidar providing single-component wind measurements would still provide useful information in the context of a data assimilation system, while complementing other existing observations.

During the past 15 years ESA has been evaluating the prospects of using space-borne DWL for measurements of global wind fields. Successive advisory committees, composed of meteorologists and lidar scientists, have helped direct the work. Many supporting contracts for lidar research and technology development were placed with research institutes and industry.

A first assessment of the potential of a DWL had been carried out in the frame of the atmospheric laser Doppler instrument report (ESA, 1989). A workshop, where the ideas carried forward in the US and Europe were presented, took place in 1995 (ESA, 1995). The workshop results, together with the 1989 report, laid the foundations for the ADM *"Report for Assessment"* (ESA, 1996) in which a first feasibility assessment was presented for a demonstration mission on the successful use of a spaceborne DWL for meteorological application.

Technological capabilities, the WMO user requirements and the experience with existing ground-based wind-profile measurements made measurement

accuracy and reliability the main mission drivers. The observation rate was set so as to achieve more uniform global wind profile observation coverage, to be able to demonstrate beneficial meteorological impact.

The baseline at that time had been the use of a 10 μm wavelength lidar and accommodation on the International Space Station (ISS). However, due to various limitations of this concept a revised implementation was elaborated. New studies revealed reasonable expected observation capabilities in cloudy scenes and end-to-end simulation studies indicated that improved meteorological analyses would indeed be feasible. The results were presented to the European Earth Observation community at a meeting held in Granada, Spain in October 1999 and in the corresponding *"Report for Mission Selection"* (ESA, 1999). In the context of the Earth Explorer missions being the science and research element of ESA's Living Planet Programme (ESA, 1998), four candidate Earth Explorer missions were considered. In 1999, the Atmospheric Dynamics Mission for wind profile measurement was selected as one of the first two Core Missions to be implemented, with a target launch date in 2007.

1.3 The measurement principle

The DWL is an active instrument, which emits laser pulses towards the atmosphere and measures the Doppler shift of the collected return signal, backscattered at different levels in the atmosphere. The frequency shift results from the relative movement of the scatter elements along the line-of-sight (LOS) of the instrument. This movement relates to the mean wind in the observed volume. The concept is shown in Figure 1.1.

The measurement volume is determined by the maximum ground integration length of 50 km, the required height resolution and the width of the laser footprint. Such measurements are continuously repeated at distances of about 200 km.

Light is scattered either by interaction with aerosol or cloud particles (Mie scattering) or by interaction with air molecules (Rayleigh scattering). The two scattering mechanisms exhibit different spectral properties and different wavelength dependencies, such that instruments evaluating only one signal type or both in separate processing chains can be constructed.

For aerosol (Mie) backscattering, the spectrum of the received Doppler shifted light equals the transmitted spectrum slightly broadened by the LOS wind velocity variation within the measurement volume (Figure 1.2). In case of molecular (Rayleigh) scattering, the Brownian motion of the air molecules significantly broadens the received spectrum to a width equivalent to a LOS wind speed range of several hundred ms^{-1}. The mean Doppler shift resulting from the actual LOS wind speed therefore represents a much smaller fraction of the spectral width as compared to the broadening caused by Mie scattering. Thus, for molecular scattering, a much higher signal is needed to achieve the same velocity measurement performance (i.e. the same wind error).

The return signal strength from aerosol and cloud scattering depends on their concentration, which varies greatly over different locations, altitudes, and time. Aerosols are most concentrated in the lower 4 km of the troposphere and diminish above the troposphere. Therefore, a system relying only on aerosol backscattering cannot consistently provide measurements at higher altitudes. On the other hand, ground return signals useful for ground speed calibration and signals from clouds exhibit the same spectral properties as the aerosol signal and can hence be processed by such a receiver system.

In contrast to the Mie signal, the molecular backscatter signal under clear atmospheric conditions is only weakly dependent on aerosol content (attenuation) and exhibits sufficiently small variation with altitude to allow more consistent

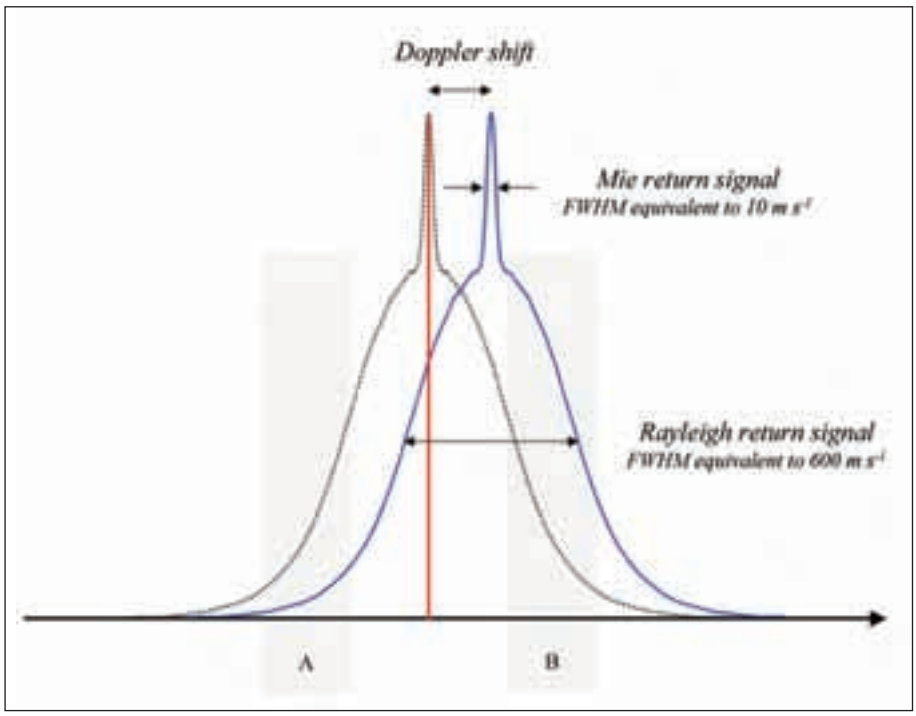

Fig. 1.2. Schematic spectrum (blue) of the light collected by a lidar in the UV to near-visible region, showing the scattering from aerosols (Mie return) and molecules (Rayleigh-Brillouin return). The received spectrum is shifted with respect to the emitted laser light (red line). The dotted curve represents an unshifted spectrum (zero wind speed). The molecular return signal is broad due to thermal motion. The thermal motion of the much heavier aerosol and cloud particles is negligible, resulting in a narrow return signal. Also shown is the position of the receiver's spectral filters A and B, used for the double edge detection technique.

measurements up to altitudes above 20 km. However, Rayleigh receivers suffer from accuracy limitations at low altitudes (< 2 km) due to aerosol absorption.

This complementary behaviour of Mie and Rayleigh return signals suggests combination of two dedicated receivers in a single instrument, in order to allow accurate measurements over the entire altitude range.

Two measurement techniques are available for the measuring of Mie and Rayleigh backscattering effects, namely coherent heterodyne systems and direct detection, interferometric systems. The operating principle of the two measurement systems is very different. Coherent heterodyne systems operate by beating the scattered and Doppler shifted radiation with an optical laser oscillator at the surface of a detector. The detected electrical beat-frequency signal is then analysed to produce the Doppler frequency. The direct detection methods analyse and disperse the optical signal field in an interferometric filter prior to detection. Both systems require interferometric precision in the optical manipulation of the signal beam. However, due to the very different physics of the schemes, the performances are in principle very different. For heterodyne systems, the key parameter is the photon degeneracy – that is the number of photo-detections per optical mode (i.e. in a single coherence area and coherence time). In low backscatter conditions this requires the available laser power to be distributed into pulses of the largest possible energy. However, for direct detection interferometric systems, the accuracy depends only on the total scattered signal and is not dependent on the energy of individual pulses, only on the total laser energy.

There is a considerable heritage of ground and airborne laser Doppler systems for wind measurement, particularly with the coherent detection of aerosol scattering at 2 and 10 μm. Validation and calibration studies were carried out and showed that the coherent laser system performance was very close to the expected quantum limit. The validation studies included measurements throughout the troposphere, studies of valley drainage, boundary layer phenomena and movement

of pollution, studies of aircraft wake vortices, and airborne measurements of clear air turbulence, wind shear, and backscatter strength around the Atlantic and Pacific oceans. Direct detection systems have been developed more recently. Very promising performance has been demonstrated with both the multichannel (MC) and double-edged (DE) variants of the basic interferometric filtering technique. These include scattering from both aerosol and molecular sources. Both the heterodyne and direct detection systems and their variants have the potential for application to spaceborne operation, and detailed investigations have been undertaken to model such application.

1.4 The contributors to the report

The lead for the Earth Explorer Core mission ADM-Aeolus lies in the hands of the Agency. The scientific support is provided by the ADM-Aeolus Mission Advisory Group. This report was prepared by six book captains who acted as coordinators for the various chapters, namely Erik Andersson, European Centre for Medium-Range Weather Forecasts (ECMWF), Reading, UK; Alain Dabas, Centre National de Recherches Météorologiques (CNRM), Toulouse, F; Erland Källen, Meteorologiska Institutionen Stockholms Universitet (MISU), Stockholm, S; David Offiler, The Meteorological Office, Exeter, UK; Ad Stoffelen, Koninklijk Nederlands Meteorologisch Instituut (KNMI), De Bilt, NL. They were supported by the other members of the advisory group, namely Pierre Flamant, Laboratoire de Meteorologie Dynamique (LMD) du CNRS, Palaiseau, F; Paul Menzel, NOAA-NESDIS, Madison/WI, USA; Oliver Reitebuch, Deutsches Zentrum für Luft- und Raumfahrt (DLR), Institut für Physik der Atmosphäre (IPA), Oberpfaffenhofen, D; Lars-Peter Riishojgaard, NASA Global Modeling and Assimilation Office (GMAO), Greenbelt/MD, USA; Harald Schyberg, Meteorologisk institutt (Met.No), Oslo, N; J. Michael Vaughan, Microwave Management Associates, Cadmore End, UK and Werner Wergen, Deutscher Wetterdienst (DWD), Offenbach, D.

1.5 The structure of the report

This report discusses the ADM-Aeolus mission. The aim of the report is to present the scientific rationale, instrument and mission concepts, data processing and scientific products, validation and impact in sufficient detail for the scientific reader.

Chapter 2 presents the scientific rationale and derived mission objectives. This is followed by the observational requirements in Chapter 3. The instrument and mission/system concepts are presented in Chapter 4, with an emphasis on the details necessary to understand the technical concept and operation. ADM-Aeolus data products and data processing are discussed in Chapter 5. This includes the scientific data processing and a discussion of the geophysical retrieval approach. Chapter 6 outlines the planned data validation activities before and after launch. Impact studies are the topic of Chapter 7.

Overall, it can be concluded that ADM-Aeolus is the first mission that will measure atmospheric wind profiles directly from space using an active optical technique and will open new avenues using a novel remote sensing technique for exploring the Earth's atmosphere.

2. ADM – Scientific Justification

2.1 Introduction

Winds are blowing everywhere on our planet. Tropical hurricanes and mid-latitude storms are manifestations of particularly violent wind phenomena that can have a very serious effect on human lives and property. However, in general winds are not violent or damaging but form the basis of the atmospheric circulation that governs weather and climate on Earth. The driving force behind atmospheric circulation is the differential solar heating between the Equator and the poles. The winds form as a result of this differential heating, and their large-scale variability has a dominating influence on the changing weather patterns as well as the long-term evolution of the Earth's climate.

In the tropics, large-scale monsoon systems determine the annual evolution of rainfall and temperature. The monsoons are triggered by changes in the solar heating of land and ocean; they are manifested through changes in the large-scale wind systems near the equator. Another very pronounced tropical circulation change is the El Niño phenomenon. During an El Niño event, the east-west circulation over the tropical Pacific Ocean is drastically changed and this results in an oceanic temperature change as well as a large-scale redistribution of precipitation patterns. Normally, there is a precipitation maximum over Indonesia associated with high ocean surface temperatures. During an El Niño event the wind patterns change, resulting in a heating of the tropical Pacific Ocean west of South America. The precipitation maximum is shifted eastwards from Indonesia to the central, tropical Pacific Ocean and the relative dryness in Indonesia and the warming along the South American west coast has a dramatic effect on tropical weather systems, tropical rain forests, the fishing industry and crop growth in South America. To determine the onset of El Niño events and to predict their intensity and time evolution, the atmospheric flow in tropical regions is decisive.

In the extra-tropics there is a general westerly flow, fairly weak at the surface but very strong in the upper part of the atmosphere. At an altitude of around 10 km we have the jet stream, streaks of very high wind speed that are experienced every day by commercial aircraft that typically fly at these altitudes. The prediction of the position and strength of the jet stream is very important for the planning of long distance commercial flights. Also, the pollution consisting of exhaust particles and gases introduced by aircraft is carried around in jet streams. The particles may act as cloud condensation nuclei and thus affect both cloud formation and radiative energy transfer. The heating/cooling introduced by upper level clouds has a marked influence on the radiation budget and thus on surface temperatures. Observations of winds are needed to assess the transport of particles and clouds at the jet stream level.

The upper atmosphere wind patterns have a dominating, steering influence on the weather patterns experienced at the Earth's surface. Shifts between stormy, rainy low-pressure systems and fair weather high pressure systems are steered by the upper level wind patterns. To predict the evolution of large-scale weather systems we need observations of temperature, pressure and wind fields. The wind field is particularly needed in areas of rapid change, i.e. where storm systems intensify and lead to extensive areas of precipitation and storminess at the surface. Precipitation is normally connected with fronts, i.e. regions with large temperature gradients. Fronts form in connection with storm developments and the dynamics of fronts is to a large extent governed by the wind field. The first attempt to make a mid-latitude cyclone conceptual model was done by Bjerknes and Solberg (1922) (Fig. 2.1).

A frontal region is typically associated with a rapid wind variation with height, leading to jet streams at high altitudes (around 10 km). There is thus a close coupling between jet streams, fronts and precipitation areas. To predict storm

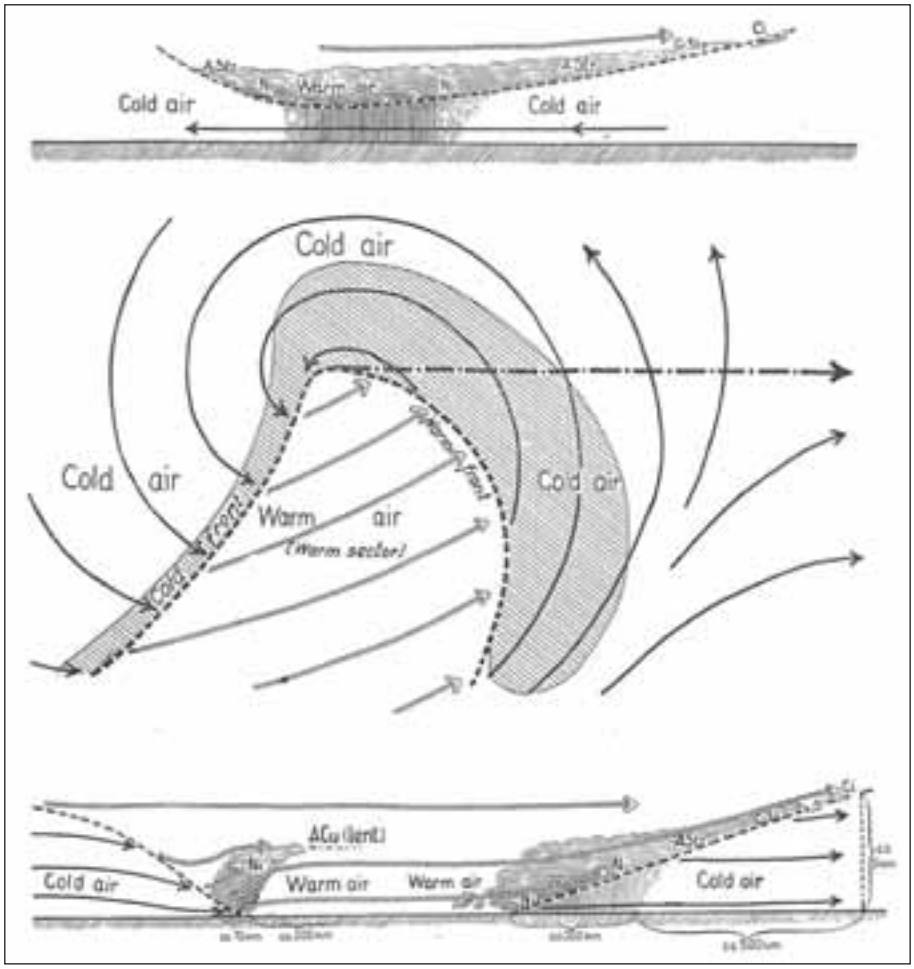

Fig. 2.1. Mid-latitude cyclone model ('Bergen school') (Bjerknes and Solberg 1922). Reproduced/modified by permission of the Norwegian Geophysical Society.

developments we need wind observations where, in particular, vertical profiles of wind speed and direction define the spatial structure of a storm. Good predictions of storms rely on an accurate analysis of storm structures in their initial stages of development.

Close to mountains, the wind blowing up the slope determines the intensity of precipitation. On the leeward side of a mountain, the descending flow acts to dissolve clouds and to decrease precipitation. Climatological patterns of precipitation are thus determined by the wind flow in relation to the dominant orographic features, with precipitation maxima and minima on the windward and leeward sides of mountain complexes. Changes in the general wind patterns will thus have a large effect on precipitation. A global warming due to an increasing concentration of greenhouse gases will also affect the global circulation patterns and thus may change the geographical as well as seasonal distribution of precipitation. To obtain accurate simulations of possible precipitation changes a necessary prerequisite is to have faithful simulations of changes in the winds.

Accurate wind field analysis is necessary to obtain reliable calculations of transport of air pollution and trace gases. Pollution transport occurs over large distances, e.g. jet streams can carry polluted air across the world oceans from North America to Europe. Also, volcanically generated particles that are injected into the upper troposphere or lower stratosphere can be transported over long distances by jet streams.

Our ability to observe and analyse winds is far from adequate; both *in situ* as well as remote sensing observing systems suffer from being incomplete and in some cases the accuracy of the wind measurements is inadequate. The World Meteorological Organisation (WMO) states in an evaluation of user requirements and satellite capabilities that for global meteorological analyses, measurement of wind profiles remains most challenging and most important (WMO, 2004). In NWP, winds are analysed together with observational information about pressure, temperature and humidity. Through the dynamics governing the atmosphere we can derive physically based laws that determine relations between the observed variables. Observations of temperature and pressure, defining the atmospheric mass distribution, can give us information about the wind field and vice versa. In the extra-tropics, the physical coupling between the wind and the mass field is strong; the rotation of the Earth forcing the mass and the wind field to be in a so-called geostrophic balance. In the tropics there is no such geostrophic coupling. Instead, characteristic atmospheric wave features determine the time dependent coupling between mass and wind. The mass-wind coupling is also scale dependent. Large-scale mid-latitude flow features are strongly geostrophically coupled, while mid-latitude flow features on a smaller horizontal scale are uncoupled. For features where the coupling is strong, mass field observations can be used to determine the wind field. Mass field observations are more abundant than wind field observations and NWP has been relying on mass field observations as the basis for atmospheric analyses. It is well known, however, that the wind field information has a very strong impact on the quality of the atmospheric analyses. This is particularly true in the tropics as well as for small-scale circulation features in the extra-tropics such as fronts and orographically generated flow features. Several examples of the impact of wind information are discussed in this report, both in this chapter and in Chapter 7, where data assimilation impact results are given. Additional wind information will increase the accuracy of atmospheric analyses.

Deficiencies, including coverage and frequency of observations, in the current observing system are impeding progress in both climate-related studies and operational weather forecasting. There is a clear requirement for a high-resolution observing system for atmospheric winds with full global coverage.

There is a synergy between advances in climate-related studies and those in NWP. Indeed, climate studies are increasingly using analyses of atmospheric (and other) fields from data assimilation systems designed originally to provide initial conditions for operational weather forecasting models. Understanding of the atmosphere and its evolution is based to a large extent on the analysed fields from continuous data assimilation carried out at operational weather centres, so that progress in climate analysis is closely linked to corresponding progress in NWP. In line with this, extended atmospheric re-analysis projects, such as ECMWF Re-Analysis (ERA15, ERA40) and the NCEP/NCAR (National Centre for Environmental Prediction - National Centre for Atmospheric Research) re-analysis, are being carried out to provide the climate and research community with consistent data sets.

The present chapter is organised as follows. The need for atmospheric winds for NWP analyses is first discussed in Section 2.2. The benefits that NWP analyses would draw from enhanced wind observations are then discussed in Section 2.3. Sections 2.4 and 2.5 address the impact of wind observations in climate and atmospheric chemistry studies, while Section 2.6 presents products from ADM-Aeolus that can be retrieved in addition to the primary wind product. These products concern aerosols and clouds and are particularly interesting for the scientific community.

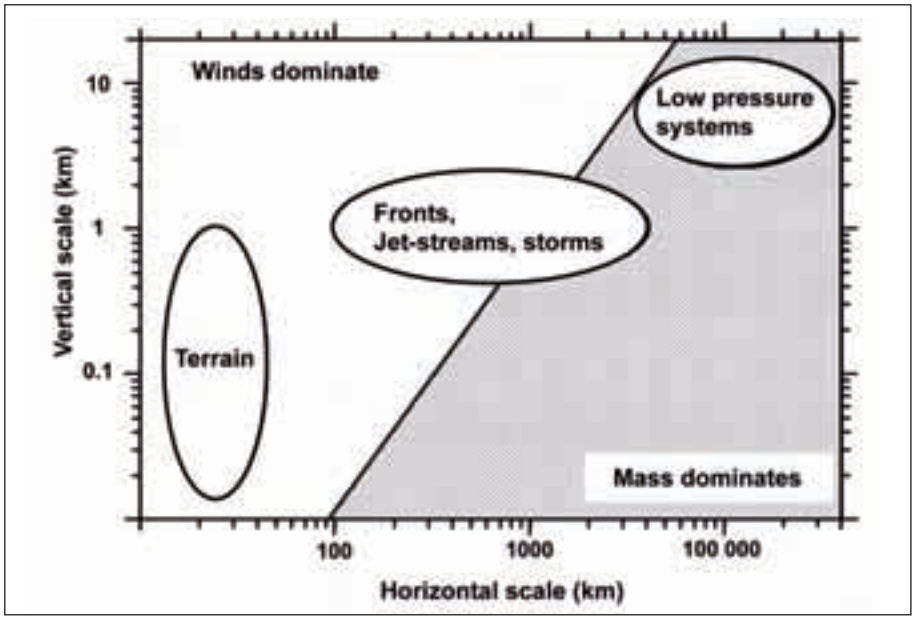

Fig. 2.2. Vertical and horizontal scales of some extra-tropic atmospheric motion systems. The straight line separating the open and shaded areas is defined by the Rossby radius of deformation (R) for a latitude of 45° as a function of the vertical scale (h). The open area denotes the range within which the wind field dominates the atmospheric dynamics and three-dimensional wind measurements are important. The shaded area denotes the range where mass information dominates.

2.2 The need for wind profile observations for atmospheric analyses

2.2.1 Background

As mentioned above, analyses of the atmospheric state are needed for a wide range of climate-related studies and for NWP. Such meteorological analyses provide a complete, physically consistent, three-dimensional picture of the dynamic variables of an atmospheric model at a particular time. They are obtained by combining in an optimal way the state of the atmosphere predicted at that time by a model with all the observations available in a time slot of a few hours ending at the start of the analysis.

In an operational data assimilation system, the analyses are produced continuously and in sequence. In NWP, medium-range forecasts, which predict the evolution of the global atmosphere typically up to ten days ahead, are generally started twice a day, at 00:00 and 12:00 UTC. Often embedded in the global models are high-resolution, limited-area models for high-resolution analyses and for short-range predictions up to 2 to 3 days ahead, which are started from initial times usually only 6 or 3 hours apart. The most common prognostic model variables are: the horizontal wind components, temperature, humidity and surface pressure. In the future, more and more atmospheric models will require additional initial values, such as cloud water content, cloud ice content, cloud amount, turbulent kinetic energy and densities of various constituents, such as ozone and aerosol.

Similar models are used for climate change studies. The basic forcing of the climate system is the thermal driving resulting from a balance between incoming solar radiation and outgoing long-wave radiation. A local thermal forcing is compensated by heat transports that are governed by the dynamics of the climate system, while the radiative balance is determined by fluxes of electromagnetic radiation. Observations from space are dominated by measuring systems determining the radiation fluxes, while parameters governing the flow properties are mainly obtained from *in situ* measurements. Both heat transports and the climate system dynamics respond to changes in the radiative forcing. To understand the processes determining the total change of the system, we need independent observations of radiative fluxes, the mass field and the motion field.

2.2.2 The importance of wind profile observations

In order to analyse the relative importance of wind data, the notion of a Rossby radius of deformation is very useful (Holton, 2004). The Rossby radius of deformation defines a horizontal length scale above which the wind and mass field are in approximately geostrophic balance. For motion systems narrower than this length scale, the wind and mass field are not directly coupled and independent wind observations are crucial. The Rossby radius helps one to understand the wind profile observation deficiency in certain regions and for certain phenomena (in particular in the context of NWP). The results of observation impact studies and the potential impact of new wind measurements can be interpreted physically using the Rossby radius concept.

Under some simplifying assumptions, the Rossby radius of deformation (R) can be expressed as

$$R = \frac{\sqrt{gh}}{2\Omega \sin \Phi} \tag{2.1}$$

where g is the acceleration due to gravity, h the vertical scale of an atmospheric motion system, Ω the angular velocity of the Earth and Φ the latitude (see Fig. 2.2).

For horizontal scales smaller than R, the wind is the essential information and the atmospheric mass field adjusts to it. For horizontal scales larger than R, the wind adjusts to the mass field. For mid-latitudes a typical value of R is 1000 km. The following general statements can be derived from Fig. 2.2:

— At the equator, R goes to infinity, so in the tropics information on the wind field is essential as it governs tropical dynamics on all length scales. In the extra-tropics, wind data are the primary source of information for small horizontal scale features (length scales $L << R$) and deep vertical structures (large h).
— Mass field information is important for large horizontal scale features ($L >> R$) and shallow vertical structures (small h).

Between these two extremes, there is a wide range where both mass and wind data are required.

From this simple theoretical analysis it is expected that wind profile observations have a major impact on forecasting in the tropics and the prediction of small-scale structures in the extra-tropics (deriving small-scale winds from height field observations does not reflect the true dynamics). Having wind profile observations in the tropics would help considerably in advancing understanding of tropical dynamics and, probably, the forecasting of severe events such as tropical cyclones.

In the extra-tropics, the availability of more wind profile data is expected to lead to capturing, much better and much earlier, initial instabilities of the flow in the storm tracks, and subsequently to improve considerably forecasts of storm developments (especially the intense ones). Even for large-scale structures in the extra-tropics, when the wind field adjusts to the mass field data, wind data are still needed. For very large planetary scales, the geostrophic relation between mass and wind is not exactly valid. As a consequence of this, wind fields derived from observed mass field data, with relatively small observation errors in the mass field data, can lead to significant errors in the derived wind. Therefore, it is important to measure the three-dimensional wind field directly also on very large scales in the extra-tropics.

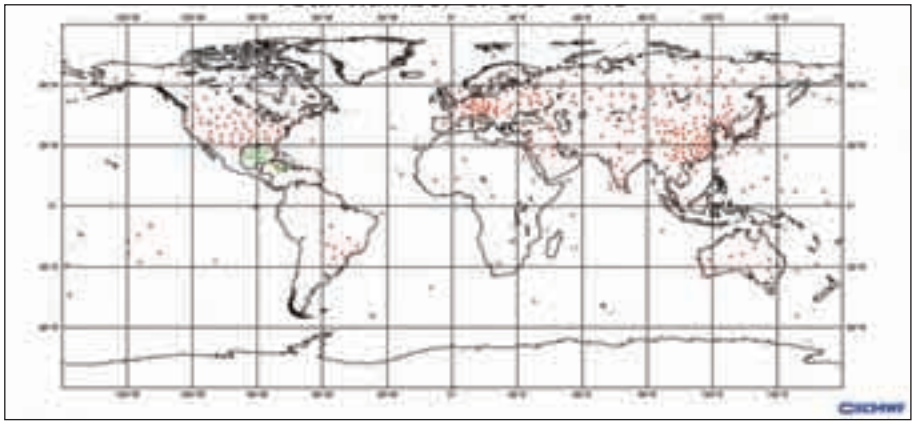

Fig. 2.3a. The radiosonde network – radiosonde/pilot ascents containing wind profile information that were available at ECMWF for the 6 hour time window centred around 00:00 UTC, 20 August 2007. This is a typical distribution and wind profile information is generally lacking over all ocean areas.

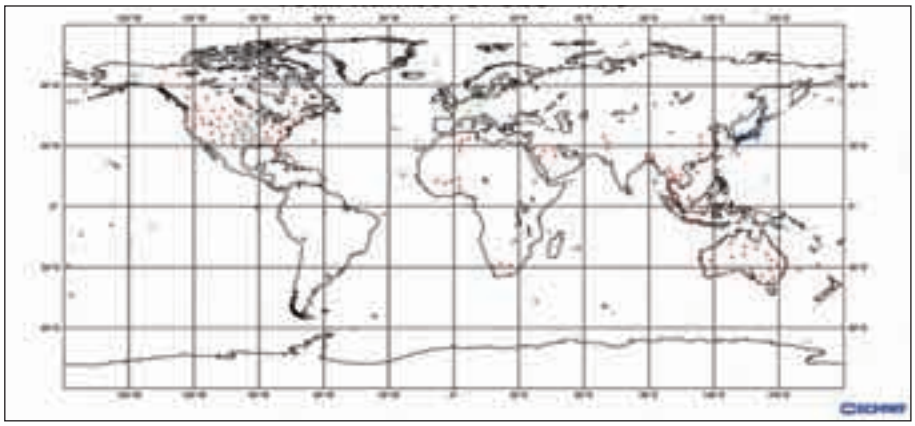

Fig. 2.3b. Pilot balloon ascents (red) and wind profiler data (blue, green and turquoise) containing wind profile information that were available at ECMWF for the 6 hour time window centred around 00:00 UTC, 20 August 2007. Wind profilers are only available at selected locations in Japan, USA and Europe. Pilot balloon ascents are mainly made over tropical areas and some sites in North America.

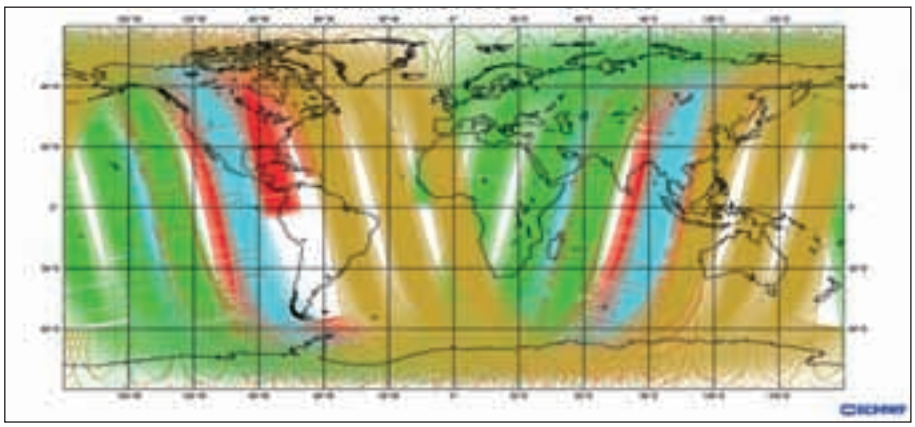

Fig. 2.3c. ATOVS satellite soundings – temperature and humidity soundings from Polar orbiting satellites (NOAA-15/16/17/18 and AQUA) as available at ECMWF for the 6 hour time window centred around 00:00 UTC, 20 August 2007 Temperature and humidity profile information from satellites provides reasonably uniform coverage.

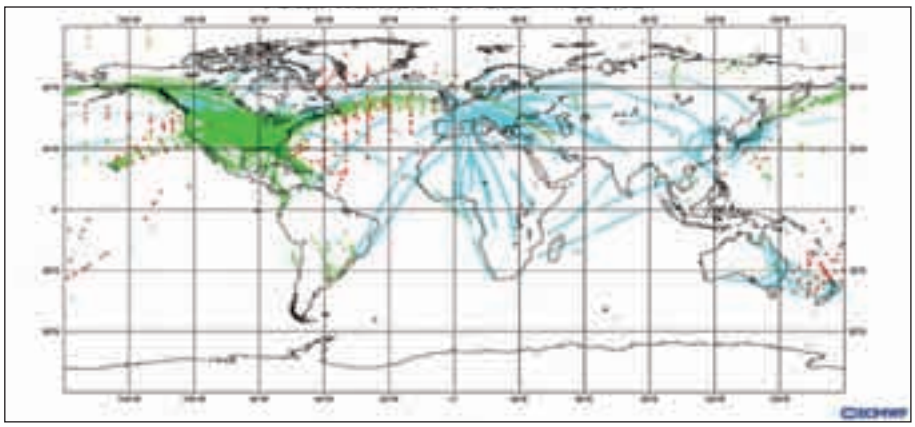

Fig. 2.3d. Aircraft data as available at ECMWF for the 6-hour time window centred around 00:00 UTC, 20 August 2007. Over the oceans, aircraft data are only available around the 10 km level; at airports vertical profiles are also transmitted.

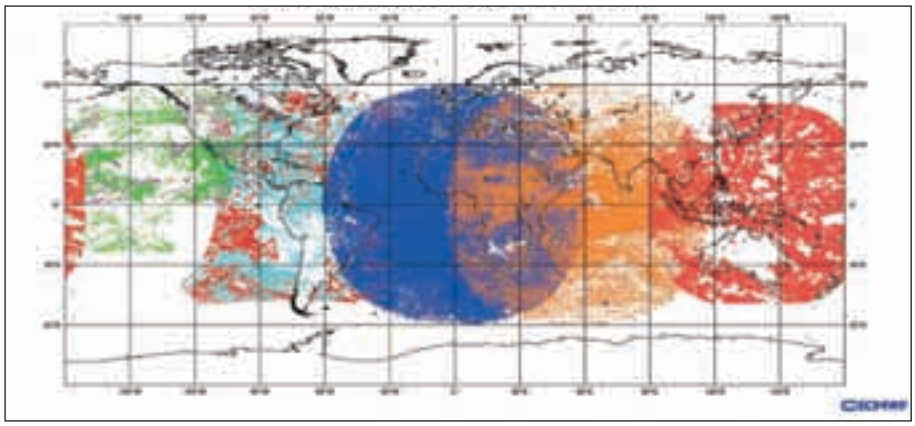

Fig. 2.3e. Atmospheric motion vectors (AMV) as available at ECMWF for the 6 hour time window centred around 00:00 UTC, 20 August 2007. The main data source is cloud track winds over tropical regions as observed from geo stationary satellites. Over Polar Regions, water vapour channels on Polar orbiting satellites are also used to track winds.

2.2.3 Deficiencies in the global observing system

In order to obtain an appropriate description of the atmosphere, a composite operational observing system has been established under the auspices of the WMO. The World Weather Watch (WWW) of the WMO is a well-established system coordinating the operational provision of meteorological data. It consists of a number of different observing platforms which take observations either at pre-specified times (synoptic hours) or quasi-continuously. They can be grouped further into *in situ* or remote-sensing measurements. They either provide information for one level only (surface or upper-air) or give profiles for a number of levels in the vertical.

The different types of observations currently available and constituting the Global Observing System (GOS) can be classified in the following way:

Surface data – the synoptic reports from land stations and ships, buoys (moored and drifting), and scatterometer winds from satellites (such as ERS, European Remote Sensing satellite). They are all single level data, and cannot provide any information on atmospheric profiles.

Multi-level upper-air data – radiosondes (Fig. 2.3a), profilers (Fig. 2.3b) and operational polar orbiting sounder data (Fig. 2.3c). Radiosondes and wind profilers are the only current observing system providing vertical profiles of the wind field, but they are available mainly from the continents in the northern hemisphere. The radiosonde network has been gradually reduced in recent years. As such, three-dimensional wind measurements remain relatively scarce. Satellite sounders provide a global coverage of radiance data, which can only be used indirectly for the definition of the mass field (temperature and humidity).

Single-level upper-air data – mainly aircraft reports (Fig. 2.3d) and cloud motion winds (Fig. 2.3e) derived from geostationary satellite imagery. More and more aircraft observations (wind and temperature) are being made during ascent and descent phases, thus tending to become 'multilevel'. Their main deficiency is the poor data coverage: observations are provided only along the air routes and they never provide any profile-type information over the oceans. Satellite cloud (or water vapour) winds are derived from the motion of some targets like clouds, assuming that this target is advected by the atmospheric flow, an intrinsic assumption that is not always true. Compared with other single-level data, they have another deficiency: the significant uncertainty in knowledge of the level.

2.3 Improvement of meteorological analyses by enhanced wind observations

Global atmospheric circulation models, used for NWP and climate simulation, typically contain more degrees of freedom than the number of observations in

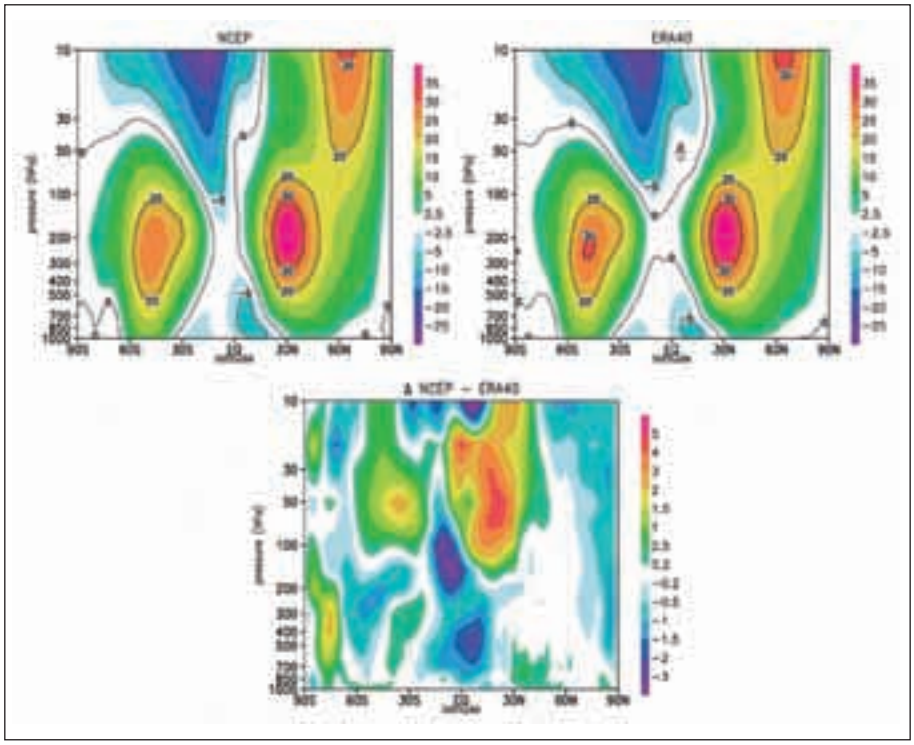

Fig. 2.4. Comparison of NCEP and ERA-40 (ECMWF reanalysis) derived zonal wind. The winds are December to February means (DJF) from 1979/1980 to 2001/2002. Major differences are found mainly in the tropics and in the lower stratosphere. Courtesy H. Körnich, MISU.

the present GOS. A large fraction of the total number of observations is provided by satellite observations (presently more than 60%), and these are, as mentioned above, dominated by mass field information. Wind information primarily comes from radio soundings; at present radio soundings only contribute less than 0.1% of the total data volume. In addition, the radio soundings mainly cover densely populated land areas in the Northern Hemisphere (Fig. 2.3a). Only a small fraction of the radio soundings come from the area 30°N–30°S, although this area constitutes 50% of the surface of the Earth. Furthermore, as discussed in Section 2.2.2, the tropical region is where wind observations have the largest potential impact. We thus find that additional wind observations are likely to have a significant impact on the quality of the GOS.

Modern data assimilation systems are quite efficient in making optimal use of the relatively sparse, current operational observations. Through error estimation theory and variational assimilation techniques, *a priori* information from short range forecasts is combined with observations to obtain optimal estimates of initial states for atmospheric circulation models used in NWP (see Bengtsson, 1981; Daley, 1991; Atlas, 1997 and the Special Issue on Data Assimilation, *J. Met. Soc. Japan*, 1997). In particular, three- and four-dimensional variational data assimilation techniques (Courtier *et al.*, 1998; Rabier *et al.*, 1998; Andersson *et al.*, 1998) are used in modern NWP systems. The main idea is that all observational information can be analysed in a dynamically consistent manner by using *a priori* information from the dynamics provided by the NWP system. For horizontal LOS (HLOS) winds measured by ADM-Aeolus, the assimilation system is vital because:

— ADM-Aeolus probes only one component of the wind (mainly East-West component). The assimilation will provide the second component, thus making possible the derivation of a complete dynamic field.

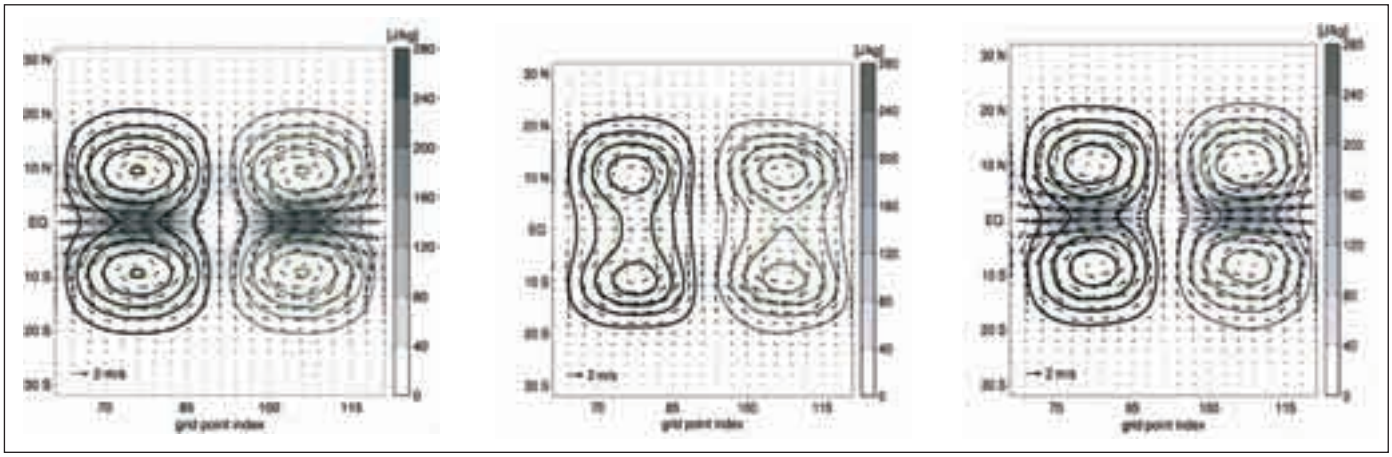

— A part of the wind measurement technique is temperature and pressure dependent (collision broadening of molecular light scattering and Rayleigh-Brillouin scattering, see Chapter 4), which must be corrected before they can be used for weather prediction or climate studies. The correction will be applied in the initial step of the assimilation by using the temperature information provided by the model.

A dynamically based assimilation system is thus a necessary requirement to produce meteorologically useful information from the observations given by the ADM-Aeolus system.

To combine the observations with background information provided through short-range forecasts, some assumptions must be made about the relation between characteristic errors of the observations and the errors of the forecasts. In particular, the spatial correlation structures of the errors are used to extract information about model parameters that are not directly provided by a particular set of observations. For instance, if only mass field information is observed, the wind field in a short-range forecast can also be corrected through the use of a geostrophic relation to determine characteristic correlations between mass and wind field errors. As mentioned in Section 2.2.2, this relation works well in the extra-tropics for synoptic scales, but it is not suitable for small-scale wind field structures in the extra-tropics or for tropical regions (see Fig. 2.2). At present, most operational data assimilation systems are designed to be optimal for synoptic scale motions in the extra-tropics. This design is consistent with the dominance of mass field information in present day observations and the need to forecast mid-latitude, synoptic disturbances accurately as these mostly affect the densely populated, industrialised regions on Earth. Over tropical areas the NWP forecasts are less accurate and this is to some degree due to the fact that less wind profile information is available in these areas. Also, small-scale wind fields in the extra-tropics are not accurately analysed because mass field observations are not sufficient to determine these structures.

In the tropics, most present day NWP systems use so-called univariate assimilation schemes. This means that the wind and mass fields are almost uncoupled and wind observations are necessary to obtain an accurate tropical wind analysis. With only mass field observations the NWP model analysis is likely to be dynamically unbalanced and the forecast quality may be seriously affected. In many studies it has been demonstrated that wind information

Fig. 2.5. Example of simulation of a tropical wave using simulated ADM-Aeolus winds. (left) 'truth': mass and wind field of an equatorial n=1 Rossby wave, 3D-Var simulation wave solution based on (middle) height-field information only, (right) height field and ADM-Aeolus HLOS winds. Solid lines are isolines of the height field, where thick lines denote positive deviations from the mean and thin lines negative deviations. Arrows denote wind vectors. Shadings indicate regions of maximum wind speeds. Thick green dashed lines correspond to the potential energy. From Žagar (2004). © Copyright 2004 American Meteorological Society (AMS).

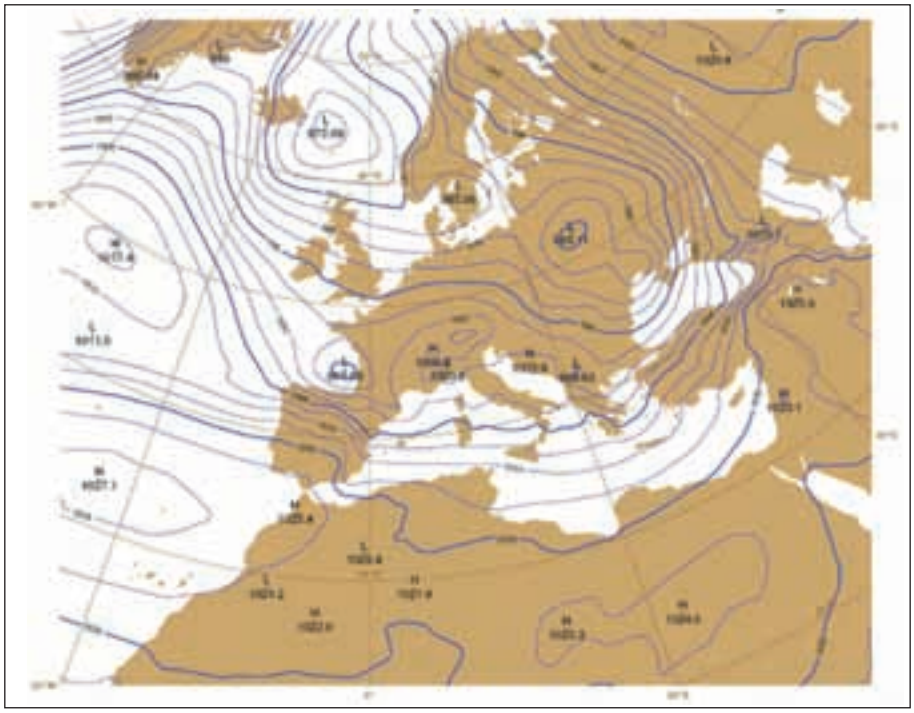

Fig. 2.6. ECMWF 48 hour operational forecast of mean sea level pressure (MSLP) valid for 27 December 1999 18:00 UTC. A shallow depression (central pressure 994 hPa) over the Bay of Biscay was predicted.

will improve tropical forecasts (Gordon *et al.*, 1972; Baker *et al.*, 1995) and a comparison between the two independent re-analyses performed at ECMWF and NCEP clearly shows the large uncertainty present in tropical winds when using present day observations (Kistler *et al.*, 2001). Fig. 2.4 shows an updated comparison of the ECMWF and NCEP re-analysis winds, with respect to the comparison shown by Kistler. This wind uncertainty directly affects tropical rainfall determination (Lim and Ho, 2000) and some recent investigations even show that humidity observations have very little influence on the global humidity cycle, but that evaporation and precipitation are primarily determined from the wind field (Bengtsson *et al.*, 2004).

In a recent series of papers, Žagar and co-authors have proposed a new assimilation technique based on tropical wave dynamics that can be used to optimise the information retrieved from mass and wind information in the tropics (Žagar *et al.*, 2004a, 2004b). The technique has also been applied to HLOS wind information as will be provided by the ADM-Aeolus system (Žagar, 2004) and it is shown that a combination of mass and wind data assimilated with a variational technique will improve the performance of present day, almost univariate tropical assimilation systems. It still remains to be shown how the tropical wave assimilation technique (Žagar *et al.*, 2004b) can be generalised to a global assimilation system.

The influence of independent mass and wind field observations on simulated tropical waves is shown in Figures 2.5a, b & c (Žagar 2004). In Fig. 2.5a, the winds and mass field of a pure equatorial Rossby wave are shown. Equatorial Rossby waves are responsible for a significant fraction of the observed variability in the tropics (Wheeler and Kiladis, 1999; Yang *et al.*, 2003). In Fig. 2.5b, the wave is simulated using only height observations, whereas in Fig. 2.5c both height and HLOS winds are included. Height observations are representative of mass field observations, such as temperature and humidity observations, which can be derived from satellite radiance measurements. Apparently a combination of

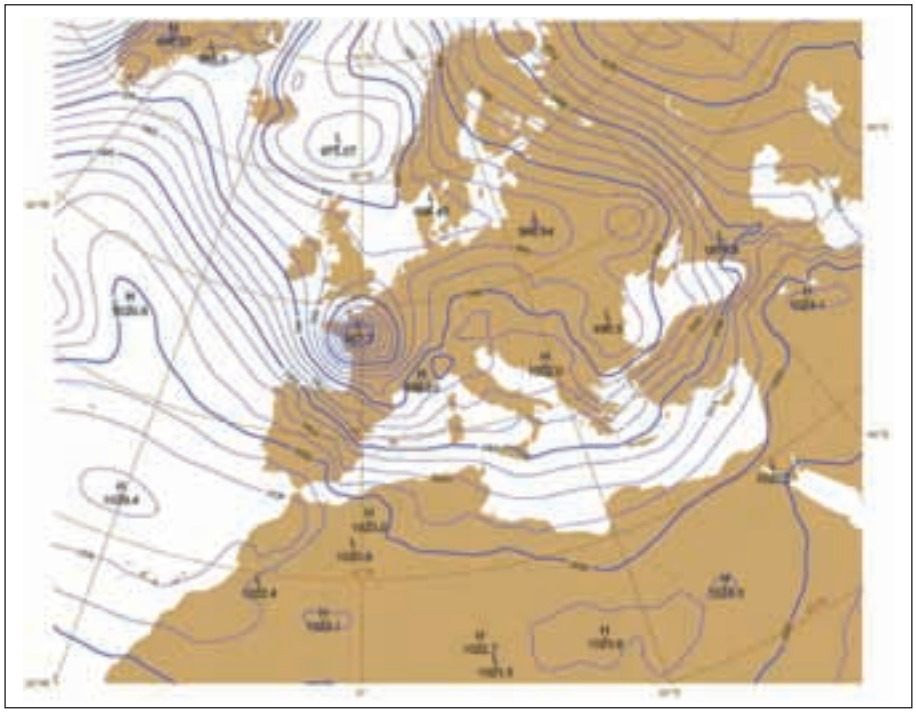

Fig. 2.7. Verifying analysis of the MSLP for 27 December 1999 18:00 UTC. A strong depression could be found over Brittany (central pressure 967 hPa).

Table 2.1. ECMWF Ensemble Prediction System (EPS) output, showing the number of 54h forecasts out of 50 members where the maximum wind speed is larger than 10 Bft or the minimum mean sea level pressure (MSLP) is below 980 hPa, indicating a storm. Three experimental sets are shown, one representative of the operational EPS (no DWL), one with assimilating wind profiles from two ADM-Aeolus satellites (DWL), and a best skill reference experiment (Pseudo-truth).

Verification *00 Z 28 Dec 1999* *+54-h forecasts*	*Number out of 50 members* *Wind speed > 10 Bft or* *MSLP < 980 hPa*
no Dwl	5
DWL	15
Pseudo-truth	35

height data with single direction wind data is adequate to reconstruct both the height and the wind field, while only height data is not enough to reconstruct the wind field. An unbalanced height field, as found in Fig. 2.5b, will give rise to inaccurate forecasts in the tropical region.

For extra-tropical forecasts, wind information is required to define small-scale flow structures, particularly relevant in situations with rapidly developing storms and/or orographically forced disturbances. Two well-studied examples in this respect were the so-called Christmas storms of 1999. The two most severe storms during the 1990s hit the Southwest and central part of Europe. On Boxing Day, 'Lothar' raced over northern France, southern Germany and Switzerland in a few hours leaving a path of destruction. The following day, 'Martin' followed on a more southerly track hitting central and southern France and the northern parts of Spain and Italy. What was common to both storms

was that the operational forecasts of many of the prediction centres failed in forecasting the storm position and intensity. As an example, Fig. 2.6 shows the ECMWF operational two day forecast of the mean sea level pressure initiated on 25 December 1999 at 18:00 UTC. This forecast for 27 December at 18:00 UTC shows a moderate low with a central pressure of 994 hPa over the Bay of Biscay.

The analysis of 27 December at 18:00 UTC showed a strong storm depression over Brittany with a central pressure of 967 hPa (Fig. 2.7). After the event, analyses were carried out investigating the causes for the failures. It quickly became apparent that the basic development took place over the western Atlantic. Based on the analysis of 27 December at 18:00 UTC (Fig. 2.7) and analysis fields from earlier cycles, the corresponding atmospheric fields 48 hours up-stream were calculated (the so-called pseudo truth). Simulated observations by a tandem ADM-Aeolus configuration were then created for an 84 hour period up to 25 December at 18:00 UTC. The feeding of these pseudo observations into a 48 hour forecast led to the rectified ensemble prediction system (EPS) storm forecast shown in Table 2.1. The DWL EPS provides an intense storm in 30% of the cases, while the no DWL (operational rerun) provides an intense storm in 10% of the cases only, according to the storm criteria.

To assess the importance of wind information in a NWP forecast system a number of different impact studies have been performed in recent years. Cress and Wergen (2001) determined the impact of wind profile observations over North America on the forecast quality over Europe. Using an operational NWP model they found a significant deterioration of the quality of weather forecasts over Europe when North American wind observations artificially were removed. In particular they found that wind profile information from radiosondes had a large impact on the cases that were analysed. Similar results assessing the overall global quality of NWP forecasts have been obtained by Stoffelen and Marseille (1998). Examples of severe storm forecasts highlight the sensitivity of storm intensity and position to subtle differences in initial states of NWP systems. Wernli *et al.* (2002) and Nielsen & Sass (2003) show how the above mentioned severe storm 'Lothar' was affected by the presence of potential vorticity anomalies in upper and lower level flows in the initial stage of the storm development. To observe potential vorticity anomalies, wind as well as temperature profiles are required. Intense storms develop on small horizontal and deep vertical scales; the Rossby radius of deformation concept, described above, suggests that wind information is more important than mass field information to define the initial structure of these storms. The potential vorticity anomalies are clearly dependent on wind field structures and severe storms form in regions with high wind speeds and strong horizontal wind shears naturally associated with vorticity anomalies.

Orographically generated small-scale flow structures can be well captured if an NWP model adequately resolves the small-scale orography, but the flow features that develop are crucially dependent on the large-scale flow across the orographic complex. Because the large-scale flow is defined by the synoptic situation, wind observations can be crucial in defining low level jets and other phenomena that directly interact with the orography. Precipitation structures and other meteorological phenomena associated with orography are, by and large, determined by the flow field. Wind information is thus essential for a correct prediction of orographically forced phenomena. In a recent study, Walser *et al.* (2004) investigated the predictability of small-scale precipitation structures in the Alpine region. They find that even if the chaotic dynamics of convection limit the predictability time scales for precipitation in many cases, there is also a clear influence from larger scale flow structures that are inherently more predictable. Small-scale convection together with orographic forcing may create organised, larger scale structures that are potentially observable and thus more predictable.

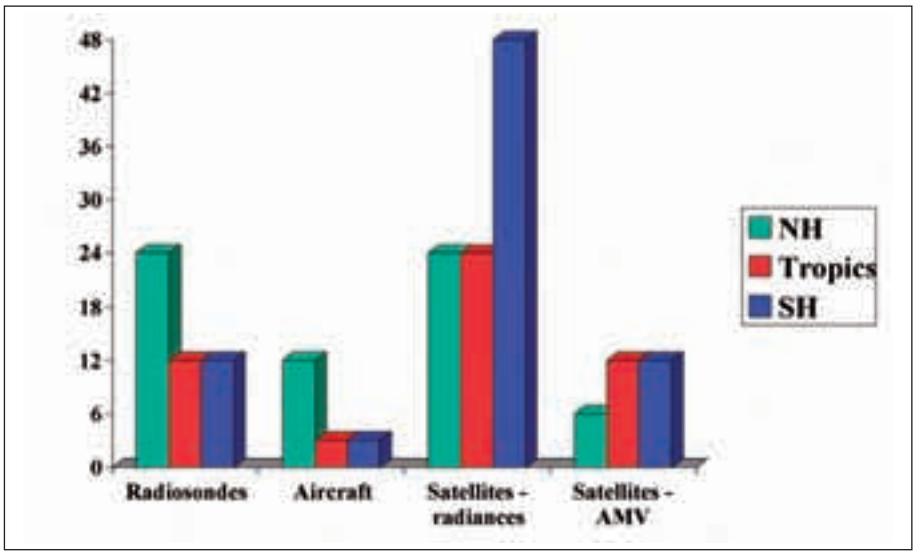

Fig. 2.8. Maximum observed contribution of present day observing systems to useful forecast length (hours) divided into three different geographical regions (NH = Northern Hemisphere, SH = Southern Hemisphere). Only the improvement in useful forecast length is plotted, the useful forecast length is typically around one week when all available observations are used. The satellite-based observations are separated into two categories, radiance measurements giving the mass field, and AMVs giving the wind field. The Figure is based on a subjective evaluation of NWP based forecast systems taken from WMO (2004).

Wind observations are crucial in this context as the larger scale structures are still well below the Rossby radius of deformation.

Gravity waves in the atmosphere are generally excited through flow over mountain complexes and in connection with convective cloud formation. Even if the gravity waves at mid-latitudes are relatively small in terms of total kinetic energy and wave amplitudes, they nevertheless can have a strong influence on atmospheric circulation in certain areas. Over mountainous terrain as well as in regions of strong convection, the gravity waves generated at low altitudes propagate upwards, and at some altitude they may break and transfer momentum and energy to the large-scale flow. Most of the gravity wave energy is concentrated on small scales and in general the waves are not directly observable or assimilated in a NWP system. Through special observation campaigns the general characteristics of the gravity wave field have been obtained and this information has been used to determine how to incorporate implicitly the effect of gravity waves in NWP and climate models. It has been shown that it is necessary to include this process in order to depict the large-scale atmospheric flow correctly. Much of the gravity wave energy is tied to the wind field. Because of the scarcity of wind information, in particular on small scales in the free atmosphere, we only have a limited understanding of how to include gravity wave effects in atmospheric models.

All the findings discussed above are in line with conclusions of earlier studies of the relative importance of wind and mass field information. A summary of results from a number of present day NWP systems can be found in WMO (2004). Assessments of the relative importance of the components of the global observing system were made and are summarised in Fig. 2.8. The maximum gains in terms of useful forecast lengths are plotted in the figure, which is adapted from WMO (2004). Conventional radiosondes are still of major importance for forecast quality in the Northern Hemisphere extra-tropics despite the very low data volume compared to satellite radiances. In the Southern Hemisphere extra-tropics, satellite radiances give a very large contribution to forecast quality. This effect has become very clear in the past decade as the quality and quantity of satellite radiance data has increased dramatically. Southern Hemisphere radiosonde data continues to be very sparse, hence the comparatively low impact. Aircraft data are concentrated around the tropopause level. Their significant impact over the Northern Hemisphere is due to their abundance over extra-tropical ocean areas

where very few other conventional observations are available. AMVs, mainly derived from cloud motion observations, have a low impact over the Northern Hemisphere while they are more important in the tropics and over the Southern Hemisphere. In general, satellite data is most important in regions where conventional, high quality observations are unavailable. The overall conclusion emphasised in WMO (2004) is the need for wind profile data, in particular in tropical regions.

2.4 The need for atmospheric winds for climate studies

Climate change issues have received substantial attention in recent years due to the increasing awareness that human activities may modify the Earth's climate. The globally averaged temperature has increased by about 0.6 degrees Celsius over the past hundred years (Jones and Moberg, 2003) and 1998 was the warmest year in the temperature records covering the past 150 years. A probable cause for the temperature increase is an increased greenhouse effect due to human activities. Carbon dioxide, released to the atmosphere through burning of fossil fuels, is the dominant contributor to an increased greenhouse effect (IPCC, 2001). Other gases in the atmosphere also contribute to the greenhouse effect, the most important one being water vapour. Water vapour dominates over carbon dioxide in terms of the total greenhouse warming. An increase in carbon dioxide is, however, significant since it can both give rise to a direct heating and perturb the climate system, changing other components. According to classical calculations by Arrhenius (1896), the positive feedback due to water vapour may enhance the carbon dioxide induced greenhouse forcing considerably. Other parts of the climate system can also increase/decrease the temperature response to enhanced levels of carbon dioxide. The water vapour feedback, for example, is crucial in determining climate change sensitivity, but some authors have argued that, in the tropics, feedback mechanisms involving water vapour, clouds, and circulation changes may even act to decrease climate change sensitivity (e.g. Lindzen *et al.*, 2001). Minchwaner and Dessler (2004) claim that present day models overestimate water vapour feedback. A very important question is thus to assess how a further increase in carbon dioxide and other man made greenhouse gases (e.g. CH_4) may affect the global climate system. It is not sufficient to just consider the direct radiative effects of greenhouse gases. We must also determine how atmospheric and oceanic circulation systems respond to an increased amount of greenhouse gases and calculate the total net effect of all the feedback processes involved. The most effective tool available to answer such questions is a physically based climate model. Such models very much resemble NWP models. All the benefits of wind data discussed in previous sections relating to NWP models are thus also relevant to atmospheric/oceanic global circulation models used for climate studies.

There are three major questions relating to climate change where an improved knowledge of the atmospheric wind field is required:

— How will tropical circulation patterns (i.e. El Niño, Madden-Julian oscillation and monsoon circulations) be affected by a global climate change?
— How will tropical cyclones be affected by a global climate change?
— How will mid-latitude storms be affected by a global climate change?

In all three cases, the atmospheric wind field plays an important role in determining the characteristics of the phenomena. Climate change affects the circulation structure that is determined by the wind field. Changes in the wind can occur as a consequence of climatically driven changes in the atmospheric state,

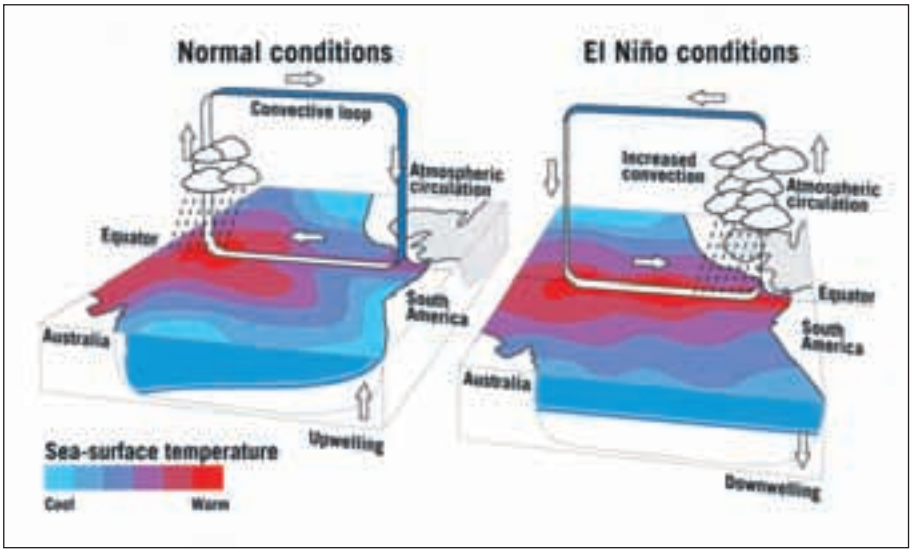

Fig. 2.9. Sketch of normal and El Niño circulation patterns over the tropical Pacific region. Under El Niño conditions convective clouds are shifted from the Indonesian region to the mid-Pacific. This shift is associated with a major change in the wind patterns as well as a change in the precipitation distribution over a large part of the tropical belt.

but the wind change also determines the climate change response. As an example, an increase in wind speed leads to an increase in evaporation over the oceans, which in turn increases the flux of water vapour to the atmosphere. Increases in atmospheric water vapour concentrations may lead to an enhanced greenhouse heating that leads to further surface warming giving rise to circulation changes and so on. Changes in the wind field are thus directly tied to climate change, both as an indicator of change and as an intrinsic part of the climate system.

Much of the uncertainty in climate simulation scenarios is related to the occurrence of tropical circulation variability and mid-latitude circulation regimes (IPCC, 2001). Changes in the frequency of extreme climate events are also closely related phenomena that depend on wind field dynamics. The El Niño/ Southern Oscillation is a particularly important example but also extreme mid-latitude storms are governed by wind dynamics. Precipitation extremes depend very much on circulation anomalies, again related to the wind field. To better judge the ability of present day climate models to simulate the phenomena, we need improved atmospheric and oceanic databases describing all aspects of the climate system. The wind field is only one component in such databases, but up to now observations of the wind field have not been as plentiful or as accurate as observations of temperature, pressure and humidity that all determine the mass field. Future compilation of climate databases through re-analysis efforts (e.g. Kalnay *et al.*, 1996; Gibson *et al.*, 1997, Uppala *et al.*, 2005) will result in improved circulation descriptions if better and more plentiful wind data is available.

Climate change simulations have been performed with a range of Atmosphere-Ocean General Circulation Models (AOGCMs) and projections of future climate change differ considerably between different models (IPCC, 2001). All models are based on the same fundamental physical and numerical principles, but they differ in the representation of physical processes that are not resolved explicitly by the calculation grid (parameterisations). Examples of such parameterised processes are cloud representation and radiation calculations. A particular AOGCM can be compared to the observed climate through control simulations of past climate change, and the parameterised processes can be compared with observations of clouds and radiation either *in situ* or from space. If discrepancies are found, changes in the formulations of parameterisations can be tested to see if the simulations improve. A fundamental difficulty with such comparisons is the

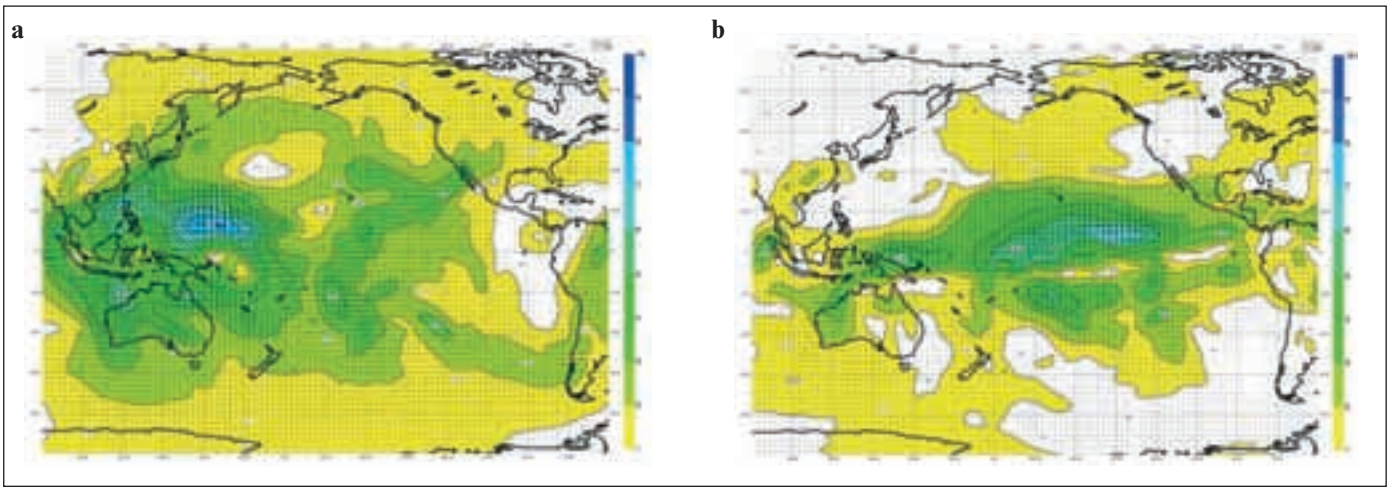

Fig. 2.10. Divergent wind field at 150 hPa – monthly mean divergent winds [in m s^{-1}] over the Pacific region for the months of March 1982 (a) and March 1983 (b). In (a) there is a divergent outflow over the Indonesian region, which is associated with normal tropical heating. In (b) the outflow has moved to the Central Pacific and this shift is associated with the El Niño event extending over 1982 and 1983.

non-trivial relation between changes in the parameterisations and the circulation response of an AOGCM. For example, a change in the heating rate in a cloud parameterisation scheme will affect the heat transfer between the ocean and the atmosphere, which in turn will change the large-scale wind divergence in the atmosphere. The climate change feedback sensitivity is largely determined by the tropical circulation systems, which is directly linked to the wind field, and the distribution of water vapour (Cess *et al.*, 1990). The water vapour distribution is mainly controlled by advection (Pierrehumbert and Roca, 1998). The interaction between cloud field heating patterns and the large scale tropical circulation may thus give rise to intricate circulation pattern changes and additional feedbacks even if only convective heating parameterisations are changed.

Model simulations of future climate change show a large spread and some of this spread is due to differences in the parameterisation of atmospheric processes. A comparison between state of the art AOGCMs shows that projected changes in temperature and precipitation differ considerably between models under the same greenhouse gas concentration change scenarios (Räisänen, 2001). These differences are even larger when regional climate change is considered. Timmerman *et al.* (1999) and Noda *et al.* (1999) have investigated the change in El Niño patterns under global warming and found contradictory results using different AOGCMs.

One of the major contributors to global climate variability is tropical circulation variability. A major reason why 1998 was the warmest year ever recorded is the occurrence of a strong El Niño event in the tropical Pacific during 1997/98. The El Niño phenomenon is coupled to a change in tropical large-scale circulation patterns as shown schematically in Fig. 2.9. In Fig. 2.10 we illustrate the change in the monthly averaged wind fields that occurred in the 1982/83 El Niño event. The wind fields shown here are derived from the ECMWF re-analysis database (Gibson *et al.*, 1997) and a marked shift in the large-scale circulation pattern over the Pacific region is apparent. The ability of climate model simulations to capture such shifts is limited (Delecluse *et al.*, 1998). One reason for this limitation is the lack of observational data that can be used to verify the ability of climate models to simulate all phases of an El Niño event properly. In particular, wind data is crucial to determine the circulation shifts associated with tropical variability. An illustration of the present uncertainty in tropical wind data can be made by comparing the re-analysis from ECMWF with the re-analysis from NCEP (Kistler *et al.*, 2001) over the tropical belt, as shown before in Fig. 2.4.

The difference between the two re-analyses datasets is substantial; with a shift in the wind field of the same order as the wind field itself. Both re-analyses use the same observation database, the differences occurring are thus due to differences in the assimilating models. As noted above, the model differences are mainly coupled with parameterisations of clouds and radiation. A conclusion from these results is that the presently available observations are not sufficient to constrain the wind field in the tropics. Model generated circulation differences cannot be judged against observations to determine which model formulation is best. We simply need better wind observations.

A particularly sensitive region for climate change is the Arctic. Here, model simulations show substantial warming (ACIA, 2004) but the geographical patterns and the warming magnitudes are very different for different models. One reason for the Arctic differences is the change in sea ice distribution. As global warming progresses, the sea ice melts, thus giving drastic changes in the ocean-atmosphere heat transfer and possibly also the ocean circulation. The geographical distribution of sea ice change is affected by the wind field in the Arctic region. The surface winds are to a large extent determined by free atmosphere winds and the surface winds directly steer ice drift. Different models have very different average wind field distributions in the Arctic and thus the sea ice melting areas are different. Observations of wind in the Arctic area are scarce and progress in the modelling of Arctic sea ice distribution depends partly on the availability of reliable Arctic wind observations. The Arctic circulation patterns are both determined by local Arctic processes and influences from propagating weather systems originating from the extra-tropics as well as the tropics. An intriguing feature of Arctic climate change is the extreme sensitivity of the region as discussed by Budyko and Izrael (1991) and also demonstrated in more recent climate change simulations (ACIA, 2004). A further understanding of this sensitivity requires improved observations of the atmospheric circulation. Several theories have been suggested to explain the sensitivity but, given the present atmospheric observations, the problem remains scientifically challenging.

The ADM-Aeolus mission will provide a much improved wind data set to be used for climate process studies. As noted before, it is necessary to assimilate the wind data in a NWP based data assimilation system to provide a dynamically consistent set of atmospheric climate states (wind, temperature, pressure, humidity, cloud, etc.) to be used for climate model development and climate process understanding. We expect the main improvements to be in tropical areas where present wind profile observations are very sparse. The impact of the wind observations is, however, not limited to tropical regions. Tropically generated disturbances propagate into mid-latitudes and can affect the circulation all the way into the Arctic and Antarctic regions. Furthermore, wind observations are crucial to determine the small-scale horizontal structure of developing mid-latitude cyclones. If climate change will affect mid-latitude cyclones, it is important to have good observations of the cyclones both in their initial and more mature stages. It has been suggested that global warming can alter the statistics of mid-latitude disturbances (Carnell and Senior, 1998; van den Brink *et al.*, 2004) and this may in turn lead to changes of larger scale circulation patterns (Brandefelt and Källén, 2004). Regional climate change very much depends on the statistics of these large-scale patterns and more comprehensive wind data will help in the understanding of processes that govern regional climate change. The basic cause of climate change due to an increased greenhouse effect is coupled to radiative transfer and thermodynamic processes, but the response of the climate system is very much governed by the dynamics of the system including wind field changes.

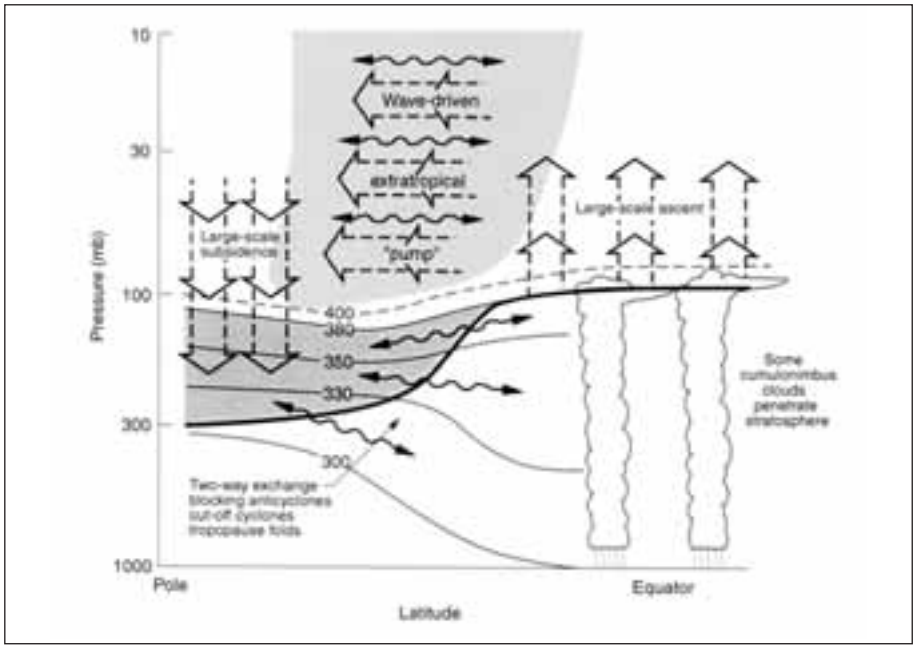

Fig. 2.11. Tropospheric/stratospheric exchange along isentropic surfaces (Holton *et al.*, 1995). Copyright 1995 American Geophysical Union. Reproduced/modified by permission of American Geophysical Union.

2.5 The role of stratospheric dynamics and chemistry

Stratospheric circulation dynamics is quite different from tropospheric dynamics. As the stratosphere generally has a high static stability, there is very little kinetic energy generated by hydrodynamic instabilities that are internal to the stratosphere. Nevertheless, we find large amplitude wave flow in the stratosphere as well as pronounced jet streams, the latter particularly in polar-regions. Dynamically, the stratospheric flow is driven by vertically propagating wave energy from the troposphere as well as radiatively forced temperature differences between equatorial and polar regions. In addition, we have a strong component of radiative forcing from ozone, which has a concentration maximum in the stratosphere. The seasonally varying distribution of ozone around the polar regions creates a thermal gradient from pole to pole. Together with momentum forcing provided by vertically propagating, breaking gravity waves, a seasonally varying zonal flow, as well as a meridional circulation cell known as the Brewer-Dobson circulation, is created as depicted in Fig. 2.11 (Holton *et al.*, 1995).

Observations of stratospheric circulation, in particular stratospheric winds, are very scarce. Standard balloon measurements rarely go above 20 kilometres. Recently, observations of ozone and other trace gases from satellite sensors have provided indirect information about the wind field. Through variational assimilation techniques, the wind field can be reconstructed from a time series of for example ozone concentration observations. This technique has several disadvantages; in particular it can be difficult to distinguish between ozone concentration changes driven by photochemical reactions versus concentration changes arising from advection by the stratospheric wind field. Sharp gradients in the ozone fields are also required in order to use ozone as a tracer for the wind field. The Brewer-Dobson circulation can only be indirectly determined via the difference between the observed temperature field and the temperature field that would result from a purely radiatively forced energy balance. Such indirect calculations give an estimate of the meridional circulation required to maintain a dynamically balanced stratospheric circulation. It may then be assumed that this circulation is driven by a combination of radiative forcing and momentum forcing

through breaking gravity and planetary waves. With direct wind observations and stratospheric wind profiles it may be possible to obtain an independent estimate of the Brewer-Dobson circulation through data assimilation techniques. Present day estimates of stratospheric climatologies in the tropical area, including the Brewer-Dobson circulation, suffer from large uncertainties (Randel *et al.*, 2002). The proposed ADM-Aeolus mission will mainly give the zonal component of the wind field, while the Brewer-Dobson circulation takes place in the meridional plane. ADM-Aeolus data will thus not give any direct measurements of the meridional circulation cell, but better observations of the zonal wind field will also improve the meridional winds through data assimilation.

The stratosphere and the troposphere are separated by a very stable layer (the tropopause), preventing vertical exchange between the two fairly distinct vertical regimes. There is, however, vertical mixing taking place in certain regions. The mixing is associated with folds in the tropopause and this occurs in regions with sharp thermal gradients associated with large vertical wind shear. Such mixing is very important for certain constituents in the stratosphere, as the troposphere is a major source region for these species (NO_X, CH_4, volcanic dust, chlorofluorocarbons (CFCs), for example). The vertical mixing in tropopause fold regions thus provides the key to estimates of stratospheric transport of such constituents. As the vertical scale of the tropopause is quite narrow, vertical temperature profiles derived from satellite radiance measurements may have too coarse vertical resolution to resolve tropopause fold features adequately. With wind profile information, such properties of the tropopause can be more easily captured. Wind profiles may thus contribute to better estimates of stratosphere-troposphere exchange.

Transport processes in the stratosphere are determined by the stratospheric wind field. In stratospheric transport models the wind field is in general derived from a balance relation between vertical wind shear and horizontal temperature gradients. This balance relation is fairly accurate in extra-tropical areas, while it does not hold in tropical regions. If transport calculations are made with a general circulation model for the stratosphere, without introducing information from observations through an assimilation process, the general dispersion characteristics of trace species are well captured. Certain constituents, such as ozone or nitrous oxide, are spread in reasonable agreement with independent observations. If, on the other hand, wind and temperature information is assimilated into a stratospheric circulation model and a new dispersion calculation is performed, the distributions of the constituents do not agree with independent observations (Douglass *et al.*, 2003; Schoeberl *et al.*, 2003). This points to a serious deficiency in the data assimilation process that could be due to inadequate assimilation methods or an incomplete data set. In particular, it appears that the lack of wind observations in the tropical stratosphere is a serious problem.

In a recent study, Lahoz *et al.* (2005) show that new, independent wind information in the stratosphere will give a marked improvement of the quality of stratospheric analyses. This is in particular true for the tropical region and the zonal wind component. In Lahoz *et al.* (2005) it is assumed that the new wind information will come from a satellite based sensor that provides both horizontal wind components with a relatively large error (5 m s^{-1}) and a coarse vertical resolution (2 km). Lahoz *et al.* (2005) also argue that in order to improve our ability to analyse and forecast ozone concentrations, we need a combination of improved ozone and wind observations.

To enhance our understanding of stratospheric dynamics, and of the interaction with chemical and photochemical reactions through radiative and thermodynamic processes, we thus need independent wind information. The

need for this understanding is not only driven by scientific curiosity about the internal dynamics of the stratosphere, it also has a strong link to the climate change problem. Global warming is mainly associated with the lower parts of the troposphere; in the stratosphere there is instead a general cooling forced by a decrease in absorption of thermal radiation from the troposphere and ozone depletion (IPCC, 2001). The height of the tropopause also generally increases with global warming, giving a lowering of temperatures in the lower stratosphere. The temperature decrease thus created can strongly affect the chemically driven ozone dynamics in the stratosphere. Strong events of ozone depletion in the Arctic region are thought to be a result of an increase in greenhouse gas absorption in the troposphere (WMO, 2002). Providing independent stratospheric wind information is a necessary condition for enhancing our understanding of stratospheric circulation and the processes associated with ozone advection and photochemical transformations. Also, other trace gas concentration distributions in the stratosphere, N_2O for example, are clearly affected by the circulation. In order to distinguish between chemical reactions and advective processes that simultaneously affect concentration distributions, we need independent stratospheric wind information.

2.6 Aerosols and clouds

Aerosols are solid or liquid particles suspended in the air. They have a direct influence on the radiative properties of the atmosphere, both through reflection and absorption of short-wave solar radiation as well as scattering and absorption of infrared, long-wave radiation. Aerosols are, furthermore, a prerequisite for cloud formation. Cloud drops and ice particles form on existing aerosol particles when the relative humidity exceeds a saturation threshold. Size distributions of aerosol particles and cloud drops and ice particles are essential factors that determine their radiative properties. The abundance of aerosol particles may also have an effect on the size distribution of cloud droplets, thus affecting the light scattering properties of clouds. This process, coupled to aerosol concentrations, is called the indirect aerosol radiative forcing effect. Atmospheric lifetime of aerosols and cloud droplets is also size dependent. Small particles have longer lifetimes than larger particles. Small water drops and ice particles remain suspended as clouds while larger drops and snow fall out as precipitation.

Regional and local aerosol concentrations depend on a balance between source strengths, advection, transformation and removal processes. The life cycle of aerosols is thus a very complex interplay between different regulating mechanisms and many of these are poorly understood. Global distributions of aerosols and clouds are a determining factor for the radiative balance of the climate system. Changes in clouds and aerosols are as important as changes in greenhouse gas concentrations in determining the factors underlying global climate change (IPCC, 2001).

Observations of aerosol concentrations and cloud properties are made using remote sensing instruments situated in space and at the Earth's surface, as well as ground-based or aircraft-based *in situ* instruments. The Lidar-In-space Technology Experiment (LITE) instrument that flew onboard the Space Shuttle in September 1994 gave essential information on atmospheric aerosol properties (Winker *et al.*, 1996). The measurement principle of a Doppler wind lidar relies on scattering of light pulses by atmospheric aerosols and air molecules. The strength of the scattering from aerosols and clouds thus gives information on aerosol and cloud properties, in addition to the wind information measured through the Doppler principle.

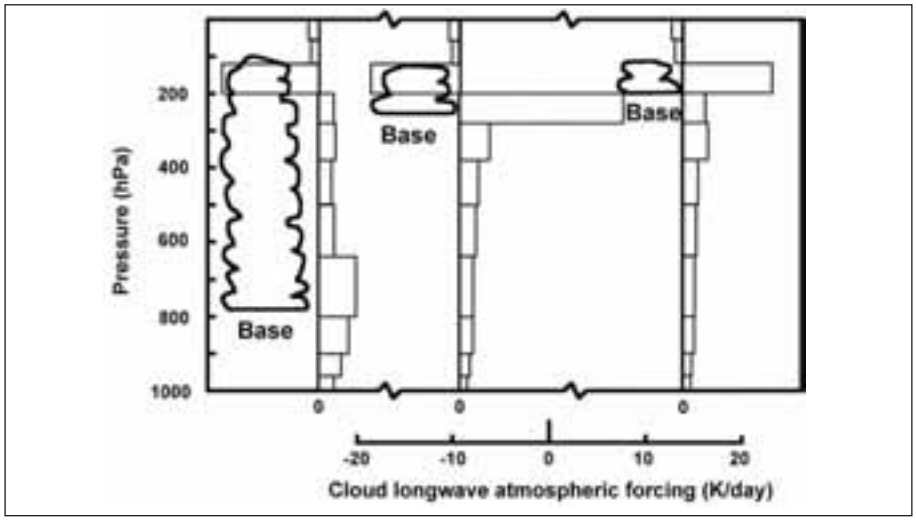

Fig. 2.12. Infrared radiative heating/ cooling profiles, calculated for three different cloud base levels (after Slingo and Slingo, 1988). These profiles demonstrate the need for an accurate knowledge of upper and, in particular, lower cloud boundaries.

2.6.1 Clouds

Clouds are the principal modulators of the Earth's radiation balance. Currently, there are global estimates of cloud cover but little information on their vertical extent or the content of condensed ice or liquid cloud water. Clouds can both absorb and reflect solar radiation (thereby cooling the surface) and emit long wave radiation (thereby warming the surface). The net radiative effect depends on cloud height, thickness and radiative properties. The concept is explained schematically in Fig. 2.12.

Clouds represent a significant source of potential error in climate simulations. Changes to the vertical distribution of clouds in a future, warmer climate could lead to large changes in the net radiative forcing. Climate models disagree as to whether the changes in cloud cover will attenuate or amplify the effect of the direct greenhouse gas warming (IPCC, 2001). Uncertainties in the vertical profiles of clouds are largely responsible for the current spread in predictions of future global warming, and also limit the accuracy of NWP. Models are able to produce the present observed top-of-the-atmosphere radiation but with very different vertical profiles of clouds and water content. To evaluate the models, observations of cloud profiles are urgently required, so that the ability of models can be improved to provide reliable weather forecasts and predictions of future global warming.

2.6.2 Aerosols

Most aerosols have a direct radiative cooling effect by reflecting solar radiation back to space. Absorbing aerosols, for example black carbon from anthropogenic sources, can lead to local heating. Aerosols also control the radiative properties of clouds and their ability to produce precipitation. Fig. 2.13 shows a sand dust outbreak over the Gulf of Oman observed by the MEdium Resolution Imaging Spectrometer (MERIS) on Envisat.

The low concentration of aerosol particles in the marine air leads to water clouds with a small number of relatively large droplets. In contrast, the high concentration of aerosols in the continental and polluted air results in water clouds with a much higher concentration of smaller droplets. Continental clouds therefore not only have a higher albedo and reflect more sunlight back to space but also are much more stable and long lived and less likely to produce precipitation. Aerosols also control the glaciation process, yet their effect on the

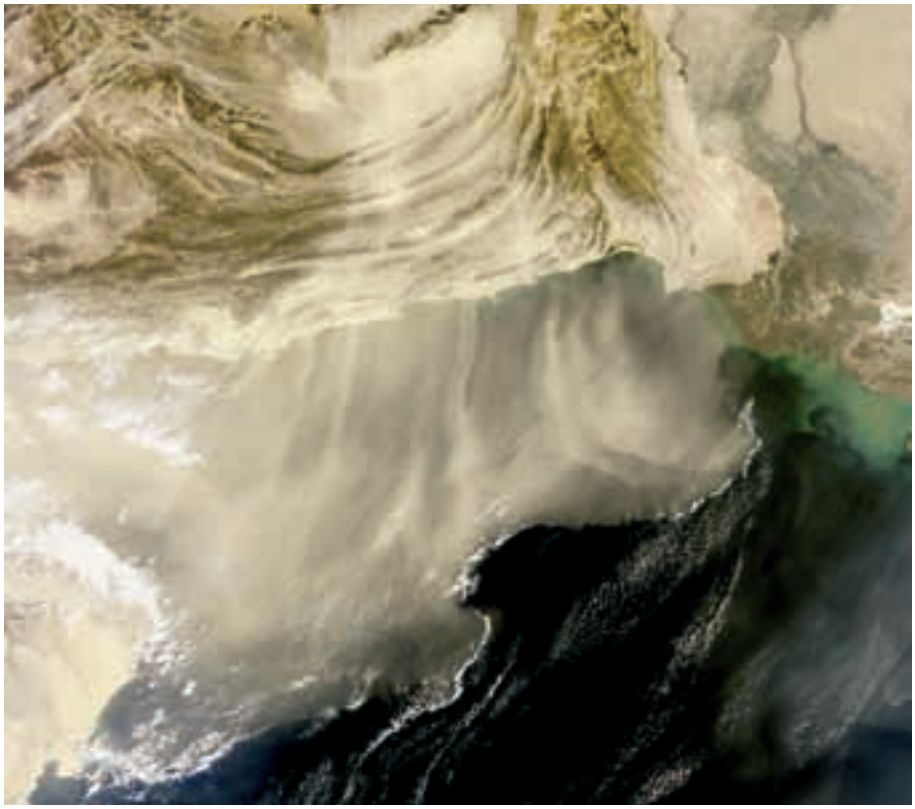

Fig. 2.13. Dust and sand storm over the Gulf of Oman (ESA, Envisat's MEdium Resolution Imaging Spectrometer, MERIS, 13 Dec 2003). The scene shows a large part of southwestern Pakistan and southeastern Iran. Dust and sand are transported for over 450 km off the coast interacting with the rather humid air present in the planetary boundary layer. This leads to a line of convective clouds at the outer edge of the outbreak.

properties of ice clouds is essentially unknown. Present observations of global aerosol properties are often limited to optical depth and a crude estimate of particle size. This is very unsatisfactory, since we need to know their chemical composition, whether they scatter or absorb, and their vertical and geographical distribution.

Changes in aerosols directly modify solar radiation reaching the ground, and also affect microphysical, biochemical and photochemical processes in the atmosphere and in clouds. In addition, increases in anthropogenic aerosols have 'indirect' radiative effects by (i) increasing the cloud albedo by decreasing the droplet size and (ii) changing the cloud lifetime. This 'indirect aerosol forcing' could be very important and must be taken into account in calculations of climate change forcing for the coming decades. However, the determination of indirect aerosol forcing is still extremely uncertain (IPCC, 2001). Unlike greenhouse gases, aerosols have short atmospheric residence times and have therefore geographically non-uniform and seasonally varying distributions. This is further complicating the evaluation of the associated forcing. Moreover, the presence of thin aerosol layers, that are difficult to detect by passive measurements, can induce strong errors in the underlying cloud property retrievals. Anthropogenic aerosol and aerosol precursor emissions are likely to vary in time and space over the coming decades, and it is essential to develop tools to evaluate to what extent extensive passive measurements can monitor the associated forcing. New active measurements of aerosol profiles are essential.

2.6.3 Doppler wind lidar contribution to aerosol measurements

As mentioned above, one of the major uncertainties in climate change predictions is the effect of changes in aerosols and clouds. By using the signal strength

information from a Doppler wind lidar, estimates of aerosol and cloud optical properties can be made. Their effects on the radiative balance of the climate system can thus be calculated and contribute to our understanding of direct and indirect radiative forcing effects of aerosols. In particular, systematic changes of cloud properties in regions with unusually high or low concentrations of certain aerosol species is a research area that has received much attention in climate change science. The uncertainties are, however, large and aerosol data with a global coverage is needed. A Doppler wind lidar can contribute to these observational needs.

The ADM-Aeolus mission, though not designed for meeting any specific objectives in terms of cloud and aerosol, can provide

— Vertical profiles on a global scale of cloud properties such as cloud cover, cloud overlap and sub grid scale cloud inhomogeneity.
— Aerosol optical depths, scattering ratio and, when possible, backscatter-to-extinction ratios. Aerosol distribution can also be derived.

At present, various satellite missions (will) carry lidars specifically designed for aerosol and cloud detection (e.g. the Cloud-Aerosol Lidar and Infrared Pathfinder Satellite Observation (CALIPSO) satellite – launched in April 2006 and EarthCARE – scheduled for launch in 2012). Although ADM-Aeolus was not specifically designed to measure cloud and aerosol properties, it can be concluded that ADM-Aeolus cloud and aerosol properties measurements will be a valuable complement to the CALIPSO and EarthCARE missions. Ongoing studies indicate that the CALIPSO, ADM-Aeolus and EarthCARE measurements can be used to establish a long-term data set of aerosol properties to the benefit of not only NWP but for climate research and prediction in particular.

2.7 Summary

The ADM-Aeolus mission will provide a global coverage of HLOS wind profiles. Wind observations are scarce in the present global observing system and this limits our ability to predict weather as well as our ability to understand fundamental processes that govern climate change. The main impact of new wind observations is expected to be in the tropics where atmospheric motions on all scales are governed by the wind field. In the extra tropics we expect the new wind information to have the largest impact on small horizontal scales and on deep vertical structures such as fronts and storm developments. Mixing processes in the tropical stratospheric region will also be better described using wind profile information from ADM-Aeolus. Finally we expect to obtain information on aerosol and cloud properties.

The main scientific objectives of the ADM-Aeolus mission are:

— Improved analysis of tropical circulation systems.
— Better predictions of intense storm developments.
— Improved understanding of circulation dynamics that govern climate change sensitivity.
— An improved understanding of stratospheric mixing processes.

In addition, ADM-Aeolus can provide information on

— Cloud properties (coverage, vertical structure, optical properties)
— Aerosol concentrations and vertical distribution.

3. Observational requirements

3.1 Introduction

The provision of more complete global wind observations for the improvement of atmospheric flow analysis are, as mentioned in Chapter 2, recognised by the WMO as a prime need (WMO, 2002). The WMO has defined different wind profile measurement requirements (WMO, 2003) depending on whether they should be used for NWP or for the modelling of climate change. Quoting from WMO (1996):

> *"Various statements of requirements have been made, and both needs and capability change with time. The statements given here were the most authoritative at the time of writing, and may be taken as useful guides to development, but are not fully definite".*

The realisation of WMO requirements would represent a major step forward for the analysis of atmospheric flows.

As mentioned in Chapter 2, current satellite capabilities for the measuring of wind profiles consist of image-derived AMVs, and spaceborne observations of the mass field together with geostrophic adjustment theory. However, it should be noted that in the absence of any appreciable wind profiling capability, the current satellite winds mainly improve wind analysis in the tropics (AMVs) and large-scale mid-latitude flow features (mass fields) (e.g. Kelly, 1997, Kållberg and Uppala, 1999). Thus the objectives, as set out in Chapter 2, are not met by these observations alone. In order to better guide developers of observation systems, the WMO has used the current satellite capability to set a threshold below which no impact is expected from additional wind measurements. Table 3.1 specifies the principal parameters for wind profile observations that have been extracted from the above-mentioned WMO requirements and capabilities documents.

The goal of ADM-Aeolus is to provide data to substantially improve the analysis of the global atmospheric flow by the provision of spaceborne wind profile observations. For this purpose, it is not necessary to entirely fulfil the optimum requirements as proposed by the WMO. ADM-Aeolus will be a useful demonstration of the beneficial impact of wind profile observations on atmospheric analyses, improving current satellite wind sensing capabilities. It is particularly important that ADM-Aeolus meets the requirements for vertical resolution and accuracy as listed in Table 3.1. Improved performance is foreseen for a potential follow-on mission.

This chapter discusses the necessary performance specifications for a global spaceborne wind profiling demonstration mission, meeting the objectives set out in Chapter 2. In order to derive useful performance specifications, it is important to assess what scales are being analysed through the current GOS and atmospheric data assimilation systems by discussing the meteorological analysis problem. Based on what is being analysed, the characteristics of complementary wind information are discussed.

3.2 Meteorological Analysis

Section 2.2 describes the general problem of meteorological analysis in the context of NWP and climate studies. Here, assimilation methodology is addressed, namely how the information contained in the GOS is projected into a spatially and temporally consistent atmospheric state.

The atmospheric state is usually discretised on a three-dimensional grid. Global models typically have an effective grid spacing (sampling) of 50 km in the horizontal and about 500–1000 m in the vertical; regional model grid scales can be a factor of two to three finer than this. A sample of the atmosphere thus has

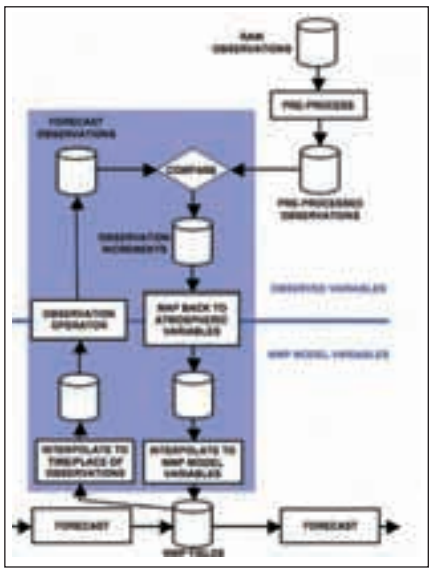

Fig. 3.1. Schematic flowchart showing how observations are used in a variational assimilation cycle. The first guess model state is transformed via observation operators (or forward models) to observation space; updates to the model state are re-mapped to model variables via adjoint operators. Adapted from a figure produced by the Met Office.

Table 3.1. Ideal and threshold requirements (indicating the likely optimum and minimal impact, respectively) for global wind profile measurements as derived from WMO (2003).

	Ideal Requirements			Threshold Requirements		
	PBL	*Tropo-sphere*	*Strato-sphere*	*Troposphere Lower*	*Troposphere Higher*	*Strato-sphere*
Vertical Domain, km	0-2	2-16	16-30	0-5	5-16	16-20
Vertical Resolution, km	0.1	0.5	2.0	5	10	10
Accuracy (Component), m s^{-1}	1.5	1.5	2	5	5	5
Horizontal Domain		global			global	
Number of Profiles, $hour^{-1}$		30 000			100	
Profile Separation, km		50			500	
Temporal Sampling, hour		3			12	
Dynamic Range, m s^{-1}		± 150			± 100	
Horizontal Integration, km		20			50	
Error Correlation		None			No requirement	
Reliability		High			High	
Timeliness, hour		1			4	

substantial spatial dimensions and only sample-mean quantities are analysed and represented in a meteorological model.

Meteorological forecast models describe the evolution of the atmospheric state. Its chaotic behaviour causes small-scale uncertainties to grow rapidly in amplitude, i.e. they form unstable small-scale atmospheric perturbations. Moreover, meteorological models may under- or over-estimate the larger-scale weather developments. It follows that observations are needed to determine the precise atmospheric circulation. The observations indicate the state of the atmosphere, but may contain detection or processing (interpretation) uncertainties and they might be in a different spatial and temporal representation than the meteorological model variables.

3.2.1 The data assimilation process

Fig. 3.1 illustrates the process of meteorological data assimilation, in which a meteorological model background – or first guess – (typically a 3- or 6 hour forecast) is combined with new observational data in an optimal way to obtain the best estimate (analysis) of the true atmospheric state. The forecast model is then run, starting from this best-estimate analysis.

The first guess contains information on past observations, which are, after incorporation into the analysis, carried forward in time by the meteorological forecast model. Fig. 3.1 shows a sequential process, where an instantaneous spatial (three-dimensional) analysis is performed at regular time intervals. The analysis step of the data assimilation cycle combines the knowledge on the atmospheric state from observations and first guess. It maximises the probability of the atmospheric state being close to reality, given the current observations and the first guess, and their respective *a priori* errors, by varying the atmospheric state until its probability is maximal (see box for more detail of the variational method).

A key point to note is that the comparison between background and observation is carried out in observation space. The observation operator for horizontal line-of-sight winds is relatively simple, being only a projection of the background field's horizontal wind components, interpolated to the observation time and location, in the lidar look direction.

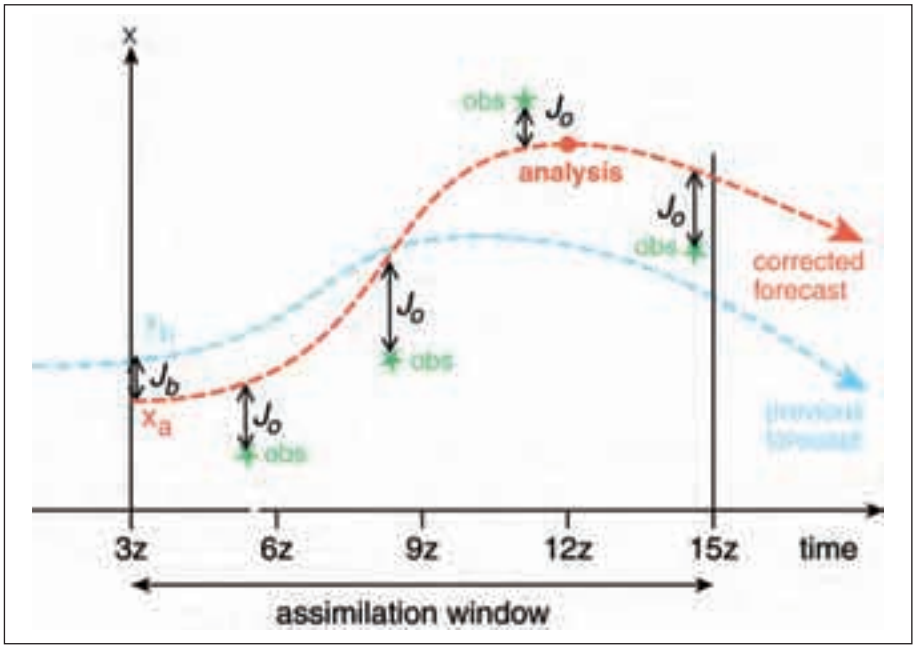

Fig. 3.2. Illustration of meteorological data assimilation using four-dimensional variational analysis. x_b: model state – background field, x_a: model state – analysis, J_b: cost function weighted fit to the background field, J_O: cost function – weighted fit to the observation. Given x_b at an initial time and observations in a 12-hour period, the assimilation calculates a corrected starting point (x_a) that produces a forecast in closer agreement with the available observations. Courtesy ECMWF.

If, at a particular location, the observation and the first guess disagree within their expected errors, then the model state is modified, such that a more likely state results. The amplitude of the modification depends on the estimated error covariance of the observation relative to the estimated error covariance of the model. The lower the relative estimated observation error, the more impact the observation will have.

Many meteorological centres are now using or developing data assimilation procedures that also take into account the dynamics during the assimilation period of the meteorological model. This is a so-called four-dimensional variational analysis (4D-Var) technique. The aim of 4D-Var is to find the closest fit to the observations that is consistent with the model dynamics over the assimilation window. The minimisation technique used in the 4D-Var scheme is conceptually similar to the technique used in the three-dimensional scheme described above, but explicitly uses the model to predict the background at the observation time, rather than using a time interpolation between previously made forecast states.

The 4D-Var process is illustrated in Fig. 3.2. Here the vertical axis represents the atmospheric state. The meteorological model first guess is modified by effectively projecting the time-varying analysis back to the start of the analysis time window. Equation 3.1 is equally applicable to 4D-Var, except in this case the terms contain the time-varying as well as the spatially-varying parameters.

3.2.2 Horizontal and vertical scales in the analysis of observations

From statistical studies (e.g. Hollingsworth and Lönnberg, 1987), it is well known that errors in the first guess are

Variational data assimilation

Obtaining the most probable state of the atmosphere is equivalent to minimising a cost function, J , given by:

$$J=J_b+J_O+J_c \tag{3.1}$$

where J_b represents a weighted fit to the background (first guess) field and J_O is a weighted fit to all of the observations. Additional model constraints, J_c – such as flow divergence limits, or a supersaturation penalty – may also be included.

It can be shown from Bayesian probability theory that in the case of unbiased conditions and with Gaussian error distributions, (and neglecting the J_c term), that the J_b and J_o terms can be written as:

$$J(x)=\frac{1}{2}(x-x^b)^T B^{-1}(x-x^b)+\frac{1}{2}(y^o-H(x))^T (E+F)^{-1}(y^o-H(x)) \tag{3.2}$$

(Rodgers, 1976, Lorenc, 1986 with notation after Ide *et al.*, 1997) where x is the current model state, y^O is a vector of the observations, B is the expected background error covariance matrix; H (x) is the forward operator, mapping the atmospheric information into observation space; E and F are the expected error covariance matrices of the measurements and the forward model respectively. The superscripts T and $^{-1}$ denote matrix transpose and inverse.

The above 'variational assimilation equation' is generic in that it can equally be applied to a vertical column (1D-Var), a surface (2D-Var) or the full atmosphere (3D-Var). Extending the analysis to include the time-dependent fields and observations allows it to apply to 4D-Var as well.

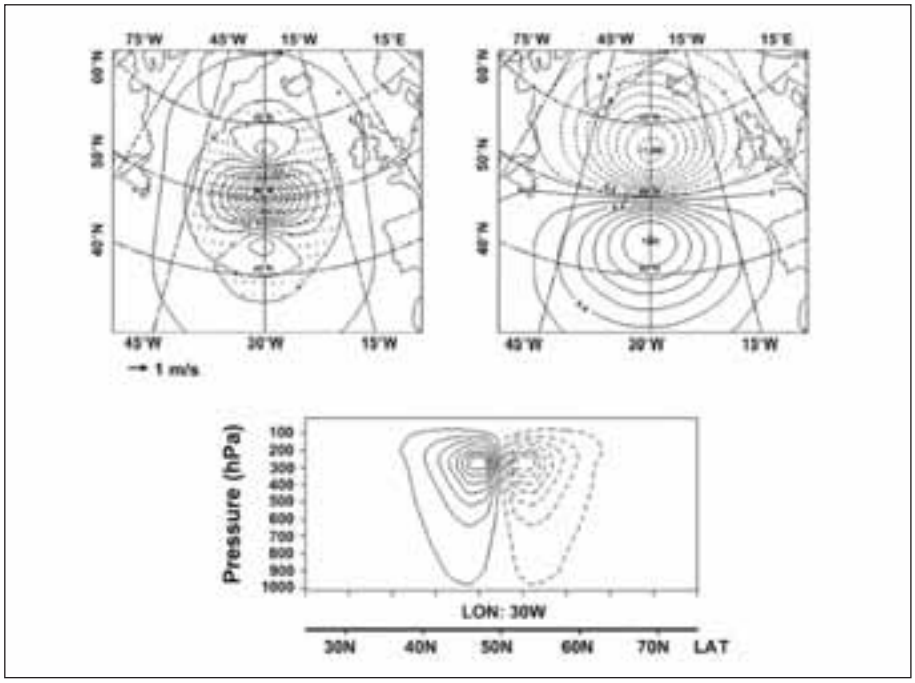

Fig. 3.3. Data assimilation response to a single isolated east-west wind observation at 200 hPa, located at 50°N, 30°W in the North Atlantic, in terms of wind vectors and wind speed (contoured) (top left) and mass (top right). The lower panel shows mass in a north-south cross section through the observation location. The horizontal and vertical scale of the analysis response to a wind observation is determined by the statistical structure of short-range wind forecast error and its known coupling with mass (i.e. pressure and temperature). Arbitrary units. Courtesy ECMWF.

spatially correlated. The analysis thus includes a spatial filter consistent with these error correlation scales (Rabier *et al.*, 1998). Moreover, errors in the mass (pressure and temperature) and wind fields are approximately in geostrophic balance, which suggests that a multivariate analysis (e.g. 3D-Var) is necessary. This means that mass observations influence the wind field and vice versa through the geostrophic balance.

An example of the multivariate spatial first-guess error structure is given in Fig. 3.3. The top-left panel shows the analysis influence from a single east-west wind observation at 30ºW and 50ºN. The scale length is typically 200–300 km, varying with latitude, with broader scales in the tropics than at high latitudes. The contours in this plot show the change in wind speed. The top-right panel shows the corresponding change in the mass field, due to the same single east-west wind observation. Mass has been reduced to the north of the observation and increased to the south to balance the observed increase in westerly wind. The typical length scale for mass is 400–500 km. The vertical extent of the mass field change (shown in the lower panel) is about 200 hPa – i.e. a vertical length scale of approximately 2 km.

3.2.3 Wind components and line-of-sight winds

In a multivariate analysis, the wind vector is decomposed into two independent horizontal wind components. Although in principle there is no problem in assimilating a true three-dimensional wind vector into an atmospheric model, the average vertical wind component is small over a typical meteorological model grid box (Courtier *et al.*, 1992) and in practice there are no regular global observations of vertical wind. The horizontal component of the DWL line-of-sight wind can be calculated using the atmospheric model information using an appropriate observation operator (see Section 3.2.1), and thus assimilated using the variational technique.

Assessing the impact of an existing observation network can be estimated by performing an observation system experiment (OSE). In an OSE, a control

experiment is run which typically uses the operational model and observation set. A second experiment is run, in which the only change is to add the new or remove the observation type under investigation. The two resulting analyses and their respective forecasts (and forecast against observations) are compared over many assimilation cycles in order to say whether the experiment resulted in better or worse forecasts than the control – the ultimate aim of course being to quantitatively improve forecasts by using the particular observation type in question.

Lorenc *et al.* (1992) have verified the hypothesis that single-component winds are sufficient by performing an OSE where none, one, or two components of the AMVs were assimilated. They found that the impact of introducing two-component wind measurements in the OSE is twice as large as the impact of introducing one wind component only. In an additional experiment, 50% of all AMVs were randomly removed, resulting in a 50% reduction of the OSE impact compared to the impact when all AMVs were used. Thus, the expected analysis-impact is the same for two collocated orthogonal components as for twice as many spatially well-separated measurements each of one single component. This study implicitly assumed that the meridional and zonal components are of equal importance (e.g. Hollingsworth and Lönnberg, 1987), though Žagar (2004) suggests that for tropical analyses, it might be better to slightly favour zonal measurements.

In a recent paper, Riishojgaard *et al.* (2004) argue that single component line-of-sight winds would have much less impact than vector observations, although the reported experiment was not very realistic in terms of the actual ADM-Aeolus scenario or modern NWP systems. Other studies, for instance Tan and Anderson (2005), show significant impact when assimilating realistically simulated ADM-type winds. It is concluded that the matching of multiple azimuth 'looks' in one geographical area is not necessary, and therefore is not a requirement for ADM-Aeolus.

On small horizontal scales (e.g. within the footprint of a DWL) and in areas with strong vertical motion (e.g. within convective clouds) the vertical component of the wind may dominate. Neglecting the vertical motion is in such cases not strictly valid; however, current NWP models cannot resolve these small scales. Therefore the vertical motion on sub-grid scales is regarded as an unwanted component of the measurement and it is rather treated as a part of the so-called representativeness error. The representativeness error is further discussed below.

3.3 Global Coverage Requirements

3.3.1 Vertical domain

The largest impact of additional observations of wind profiles are in the upper troposphere/lower stratosphere, i.e. between 5 and 16 km, the upper limit depending on latitude (Cress and Wergen, 2002). Wind profile information is still useful over the full tropospheric range between the surface and 16 km. In addition, as more forecast models are being extended into the upper stratosphere and mesosphere (to 0.1 hPa and above), wind profiles in the lower stratosphere (between 16 and 30 km) will be highly desirable, even at reduced accuracy and vertical resolution, as there are extremely few wind measurements at these altitudes; radiosondes rarely reach above 20 km.

3.3.2 Vertical resolution

In the vertical, meteorological model levels are separated by roughly 500–1000 m, and have typical error correlation lengths around 2000 m. Range integrations over 1000 m are thus appropriate to ensure proper sampling. The required resolution in the stratosphere is lower, i.e. 2000 m (WMO, 2003). In the planetary

boundary layer, the required vertical resolution is higher (<500 m) because of the small-scale vertical structure of the flow. On the other hand, observations in the lower tropopause region and close to the surface are relatively abundant in the current GOS (e.g. AMV and scatterometer wind vectors and Special Sensor Microwave/Imager (SSM/I), and wind speeds), so new DWL wind observations are not expected to have as much impact here as in the free troposphere.

3.3.3 Horizontal domain

Wind profile observations are required globally. Due to the shortcomings of the current observing system (see Chapter 2.2.2), they are particularly needed over the oceans, in the tropics, and in the Southern Hemisphere.

3.3.4 Horizontal resolution

The horizontal scale used in current meteorological analyses partly depends on the current GOS and on the data assimilation methodology. Experiments with reduced grid sizes have demonstrated positive benefits as smaller scale features are better represented (Simmons and Hollingsworth, 2002). Operational model grids scales are today in practice limited by computing resources. Although both meteorological models and analysis methodologies are evolving, it is noted that the spatial extent of the horizontal error correlation structures (e.g. Fig. 3.3) is to some extent determined by the density of the GOS observation network. If a much denser observation network were available, smaller scales could be resolved. It is difficult to achieve this by adding only single supplementary observations. The spatial extent of the error structures can be significantly reduced with the availability of an extensive and dense global wind profiling network. It should be noted that the number of upper-air stations in the observation network is in decline, which is only partially offset by satellite radiance data.

Small-scale weather is determined by coherent structures (see Fig. 3.3). The transverse wind correlation distance is roughly 200 km (half-width half-maximum), implying that one observation provides information on the error of the model state within a radius of about 200 km around the observation location. Consequently, the added value of the observation information on the model's atmospheric state is independent as long as observations are separated by at least 200 km. The horizontal sampling requirement for ADM-Aeolus is thus 200 km with uncorrelated errors at that mean separation.

There is no requirement on a particular sampling scheme, since the assimilation process is capable of handling varying spatial representation.

3.3.5 Space and time scales

The required temporal coverage of the ADM-Aeolus measurements is equal to the typical timescale of the resolved atmospheric structures. This time scale is typically one day, and a sensible requirement is full global sampling every 12 hours.

As shown in Section 3.2.2, atmospheric structures have typical horizontal scales of 200 km. If each wind profile represents a box of 200 km by 200 km on the Earth's surface, then the total Earth surface contains about 13 000 boxes. Therefore, 26 000 independent wind-component-profile observations per day would define the three-dimensional global wind vector field completely, twice a day. This would imply an idealised observing rate of about 1000 per hour. Table 3.1 showed that the threshold and ideal requirements for the horizontal spacing of the wind profile measurements varies from 500 to 50 km, which corresponds to 100–30 000 profiles per hour. The impact of additional wind profile measurements in NWP analysis is likely to be obtained by the ADM-Aeolus mission measuring 130 single-component profiles per hour. Based on the ideal requirements, it is

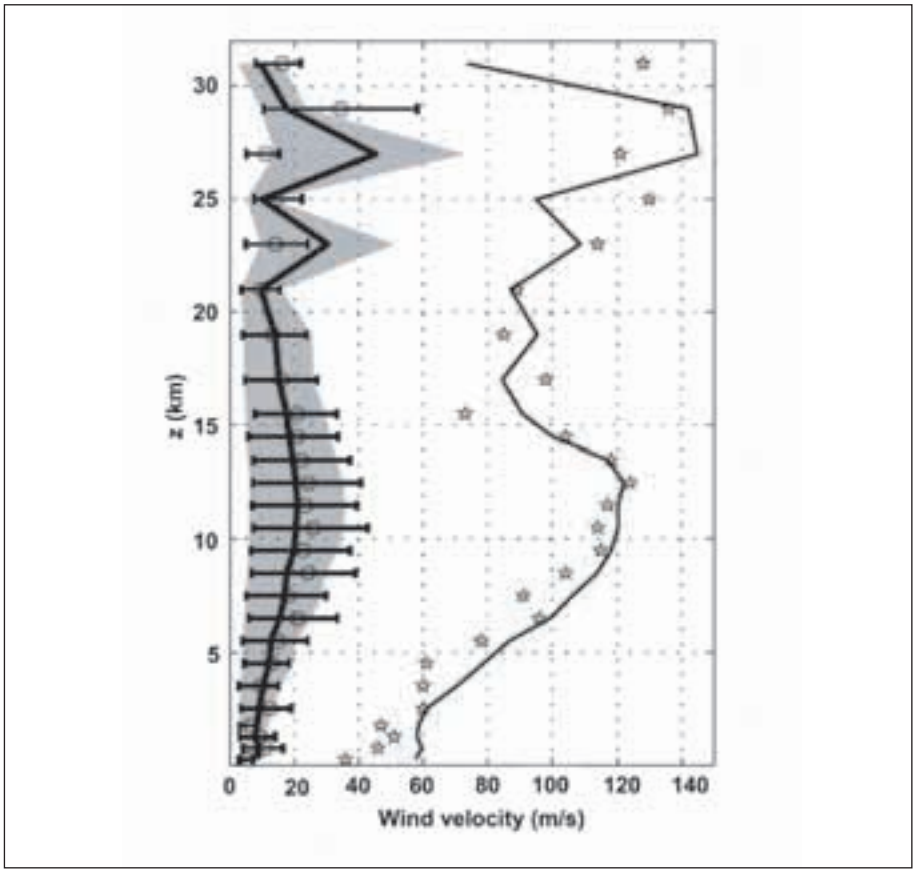

Fig. 3.4. Vertical profiles of wind velocity. Thin and thick solid lines and shaded regions indicate maximum, mean and variability around the vector mean for the analysis data set, whereas stars, circles and horizontal bars show the same quantities for the observational data set (Håkansson, 2001).

preferable that a future operational mission would be capable of measuring more frequently (temporally and spatially) than ADM-Aeolus.

An improved analysis of the atmospheric flow will lead to an improved NWP forecasting skill. OSE's with conventional radiosonde wind profiles at ECMWF (Kelly, 1997, and Ingmann *et al.*, 1999) and NCEP (Atlas, 1997) have shown that the density of the network is the key component for NWP skill improvement. However, its coverage is limited to land areas and furthermore most concentrated over Europe and the USA. The total number of wind component profiles is 1200 per 12 hours (600 vector profiles) or an equivalent of 100 per hour. Based on these findings, it is argued that the extension of the wind profile coverage to the oceans at a similar density to the current (land-based) radiosonde network would make the quality of the analysis much more uniform. Hence a requirement on ADM-Aeolus is to measure at a rate of at least 100 profiles per hour. This would improve atmospheric flow analyses and be of great benefit to NWP and climate studies.

3.3.6 Dynamic range

Fig. 3.4 shows statistics of atmospheric wind speeds as a function of height determined by Håkansson (2001) in which jet streams at 10–15 km and 25–30 km are clearly seen. In order to cover the range of wind speeds encountered in the atmosphere, ADM-Aeolus should be capable of delivering horizontal line-of-sight wind speeds over the range 0 to 150 m s^{-1}, although for the uppermost levels, the accuracy and vertical resolution requirement is more relaxed.

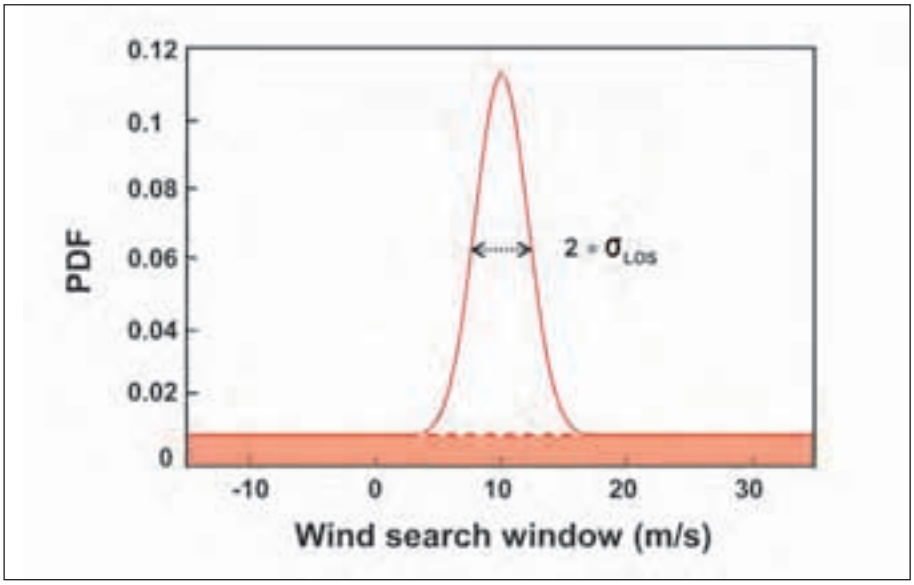

Fig. 3.5. The estimates PDF model looks like a cluster of localised good estimates (bell shape) around the true mean speed (here 10 m s^{-1}) sitting on a pedestal of uniformly distributed bad estimates (shaded zone) extending over the wind search window (mean ± 25 m s^{-1}).

3.4 Observation quality requirements

The quality of the observations can be expressed in terms of their accuracy and error correlation.

3.4.1 Quality definitions

For wind observation in the low-backscatter regime, the number of events (photons) per measurement interval, detected at receiver level, can be close to the number of 'noise' events. The retrieved wind speeds from measurements with a low signal-to-noise ratio (SNR) are less accurate, especially for cases where the noise mimics the measured signal. A probability density function (PDF) of the horizontal line-of-sight wind speed estimation (V_{HLOS}) can be estimated by retrieving the wind speed from a synthetic measurement applying the estimated error distribution. The resulting wind speed distribution looks like a cluster of localised good estimates (bell shape) around the true mean speed (V_{true}), as shown in Fig. 3.5.

An approximate model of the estimated PDF for any observing system – here with terminology appropriate for ADM-Aeolus-type horizontal line-of-sight winds – is as follows:

$$PDF(V_{HLOS}) = (1 - P_{ge})\frac{1}{V_S} + \frac{P_{ge}}{(2\pi)^{\frac{1}{2}}\sigma_{LOS}} \exp\left[\frac{-(V_{HLOS} - V_{true})^2}{2\sigma_{HLOS}^{\ 2}}\right] \quad (3.3)$$

The accuracy is the random part of the wind-speed estimation error. It is defined as the standard deviation of the estimates (σ_{LOS}) (good estimates) falling under the bell shape. The probability of gross error (P_{ge}) is the complement to unity of the percentage of estimates (bad estimates) contained in the pedestal of uniform distribution over the 'search window' wind speed range (V_S). Estimates outside the search window would always be considered 'bad' and thus rejected.

3.4.2 Accuracy

Wind speed varies with height, leading to a height-dependent accuracy requirement. The accuracy of the radiosonde wind observations is the key

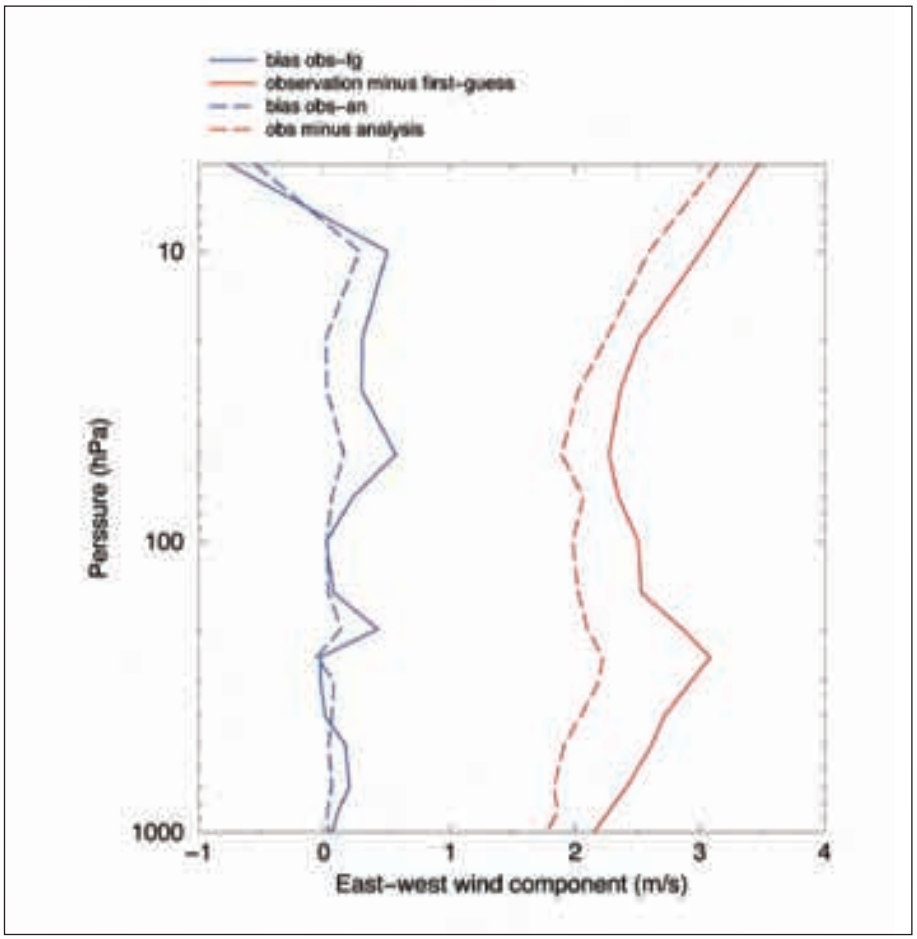

Fig. 3.6. Mean (blue) and standard deviation (red) of the difference between radiosonde wind observations (east-west component, m s^{-1}) and the first-guess (full lines) and analysis (dashed lines), for all stations in the Northern Hemisphere north of 20°N, for one day in ECMWF's data assimilation system. The graph provides indication of the combined errors in first-guess and observations. Courtesy ECMWF.

element of the GOS. Their wind component accuracy varies from 2 m s^{-1} close to the surface to 3 m s^{-1} around the tropopause level, which is close to the accuracy of the model first guess. Fig. 3.6 shows a vertical profile standard deviation and bias of the first guess minus radiosonde observations, together with equivalent analysis minus first guess profiles.

Over data-sparse areas the 2–3 m s^{-1} accuracy requirement is expected to be sufficient to provide a beneficial impact on meteorological analyses. This requirement is significantly higher than the 5 m s^{-1} threshold requirement quoted in Table 3.1. Meteorological data assimilation sensitivity studies have shown that observations with an accuracy worse than the first guess often fail to have a beneficial impact on NWP. In fact, data with a substantially poorer accuracy often have a detrimental impact.

Observations should be made with a horizontal spacing representative of the size of the meteorological model grid boxes. A typical horizontal grid box size is 50 km. However, a true mean quantity often cannot be derived for each grid box. Therefore, a spatial representativeness error remains. Lorenc *et al.* (1992) investigated this representativeness error for line-of-sight winds in detail, by considering typical wind component variability energy-density spectra. The representativeness error turns out to be height dependent (Table 3.2). The dependency of the assumed (specified) error on the mean wind speed appears not to be applicable for jet-level winds. The representativeness error should be added to the detection and processing errors (error variances) of a

Table 3.2. Spatial representativeness error for a point measurement and for a line–averaged component line-of-sight wind and a 50 km horizontal scale.

Pressure [hPa]	Point Error [m s^{-1}]	Line Error [m s^{-1}]
1000	2.1	1.5
750	2.0	1.4
500	2.4	1.7
250	3.3	2.3
150	2.4	1.7
50	2.1	1.5

wind profile measurement before attempting to validate it against the accuracy requirement. A line-averaged wind has a smaller representativeness error than a point measurement by a factor of $\sqrt{2}$. For the ADM-Aeolus, a horizontal line integration of 50 km, separated by 200 km, is required.

Observation accuracy and first-guess field accuracy are used to determine the relative weight of an observation over the first guess. An improper *a priori* specification of the observation error will therefore lead to a wrong assessment of the value of the observation, and consequently to an inferior analysis. As DWL winds have variable accuracy, it is important to develop algorithms that are able to define their accuracy prior to assimilation.

From the above considerations, an accuracy of 2 m s^{-1} over the height range from 2 to 16 km is required from ADM-Aeolus. If winds in the range 16–30 km can be provided, a reduced accuracy of 3–5 m s^{-1} would be adequate (WMO, 2003).

3.4.3 Error correlation

Spatially correlated errors are potentially very damaging in data assimilation, in particular when the error structure is *a priori* not well known. For example, the spatial error structure in satellite temperature and humidity profiles has been a problem in meteorological data assimilation for more than a decade. In particular, when the precise spatial observation error correlation characteristics are poorly known, then the analysis may have high-pass filter characteristics and the resulting analysis can be noisy (Liu and Rabier, 2002).

Any systematic error in the analysis will have the multivariate and spatial structure prescribed by the structure functions, i.e. the error is meteorologically balanced and will influence the evolution of the model state in an effective way. Air-mass-dependent errors are the most damaging, since these potentially change the way in which air masses interact.

One piece of information required from wind profiles is the vertical wind-shear. The first-guess vertical error-correlation scale is small and so, given the filter properties of the analysis, it is clear that any vertical correlation structure of error in the wind profile measurements may be potentially very damaging, since the windshear information may be lost. If the aim is to be able to measure a wind shear of 2 m s^{-1} between two adjacent levels, then a correlated error of a few tenths of m s^{-1} may already significantly blur the detection of such shear. Note that a data assimilation system can handle wind-shear measurements directly. However, in this case it is even more important to have independent measurements in a vertical wind profile.

Correlation of error between profiles, although possibly less damaging than vertical error correlation, does require attention. Experience with other satellite sensors has shown that systematic errors or errors that depend only on specific instrument characteristics or orbit phase (Sun angle), can be taken out by

calibration against a meteorological model (e.g. Stoffelen, 1998). Obviously, in this case the meteorological model is calibrated by using conventional observations. For calibration of an observing system against a meteorological model, it is an absolute requirement that the observing system is stable.

In summary, a useful and practical specification for systematic offsets is that the correlation between the error variances of any two horizontal line-of-sight wind measurements is less than 0.01 (Stoffelen *et al.*, 2002).

3.4.4 Probability of gross error

Routine data assimilation systems include quality control (QC) procedures to prevent any measurements having large errors from affecting the atmospheric analysis. When a gross error occurs, the observation does not relate to the (model) atmospheric state and can therefore potentially damage the objective analysis, leading to an incorrect picture of the state of the atmosphere. For conventional systems, gross errors are usually caused by data transmission or instrument failure, or by unrepresentative measurements. A classic example of the latter is the release of a radiosonde through a thunderstorm. Forecasts are known to be sensitive to gross-error elimination procedures in critical atmospheric conditions (ESA, 1996).

Many operational centres are using or developing variational analysis systems. The variational analysis system is quite flexible in dealing with observations with complex error characteristics. However, for the measurements to be useful, these observation characteristics have to be known in detail *a priori*. Experience with conventional observation systems and associated quality control decisions in operational meteorological analysis indicate that the rate, or probability, of gross errors presented to the analysis (after QC) should not exceed a few percent. All signal characteristics have to be used in the processing to optimally specify the observation errors in order to reject measurements containing no information on the true atmospheric state. All this is necessary to prevent random wind estimates that are, by coincidence, close to the true wind, from influencing the analysis. Based on this experience, it is required that the observations need to have a probability of gross error of less than 5%.

3.5 Data availability

In a meteorological data assimilation system, the meteorological observations provided in a timely fashion by the GOS are compared to the first-guess atmospheric state. The error characteristics of the first guess are well monitored and the first guess is a well defined reference atmospheric state. In turn, this reference atmospheric state is used to routinely monitor and control the observations. If observations are not available in due time, the routine monitoring and control is not performed. Special measures then have to be taken to collocate the observations with the meteorological model and other observations in order to characterise their error properties. The routine monitoring, collocation, and control of observations in the main near-real-time data stream is clearly preferred over offline processing.

After the error characteristics of a new observing system are determined, experimental assimilation of the data may begin. If the observations are delivered in near-real time, the operational data assimilation and forecast suite can be used as a reference or for a control experiment. If the new observing system adds to the improvement of the weather forecast of the control experiment, then the data may be a candidate for operational assimilation of the data in NWP.

Timely data delivery is required since analyses start at pre-specified times and a data cut-off time is applied. For NWP, acceptable data-delivery times for short- and medium-range forecasting vary between 30 minutes and more than

Table 3.3. Summary of observational requirements of the Atmospheric Dynamics Mission

	Observational Requirements		
	PBL	*Troposphere*	*Stratosphere*
Vertical Domain, km	0-2	2-16	16-30*
Vertical Resolution, km	0.5	1	2.5
Horizontal Domain		global	
Number of Profiles, hour^{-1}		100	
Profile Separation, km		200	
Temporal Sampling, hour		12	
Accuracy (Component), m s^{-1}	2	2-3	3-5
Dynamic Range, m s^{-1}		± 150	
Horizontal Integration, km		50	
Error Correlation		0.01	
Probability of Gross Error, %		5	
Timeliness, hour		3	
Length of Observational Data Set, year		3	

* The formal requirement is for an upper range of 20 km, but 30 km is highly desirable for stratospheric dynamics; a relaxed requirement for accuracy and vertical resolution is acceptable in the 20–30 km region.

6 hours, depending on the analysis time window and analysis cut-off delay. A data delivery requirement of 3 hours is usually specified for spaceborne data (as practicable for global NWP) and is common for polar-orbiting spaceborne operational meteorological instrumentation. Shorter cut-off thresholds are often critical for regional and local models, where 1 or 2 hour delivery is a requirement. Since satellite data is usually continuous and asynoptic, the more timely the delivery, the more data will be included in the analysis before the fixed cut-off time, and so it is desirable that at least subsets of ADM-Aeolus data be delivered with a timeliness significantly better than 3 hours.

The length of the observational dataset needed to achieve the objectives of the ADM-Aeolus demonstrator is at least three years.

3.6 Conclusion

The observation requirements for ADM-Aeolus discussed in this chapter are based on the current GOS and the synergy with it. As for many other meteorological observations, the spaceborne horizontal line-of-sight wind component profiles by themselves seem at first glance to be of limited value. However, in the context of atmospheric data assimilation systems they would in fact be an essential component of the GOS. Improved meteorological analyses are, in addition to improving weather forecasts, also useful for studying circulation and transport phenomena relevant to climate and atmospheric composition studies. Moreover, the meteorological analysis fields already provide consistent atmospheric data sets of wind, humidity, temperature, and, in the coming years, ozone and aerosol distributions. The monitoring of the quality of meteorological analyses fields is best done in near-real time by collocation with and through rigorous comparison to a wide range of realtime meteorological observations, complemented by off-line validation studies.

For a mission intended to demonstrate the feasibility of a full-scale spaceborne wind observing system to improve global atmospheric analyses, the requirements on data quality and vertical resolution are the most stringent and the most important to achieve. Under this assumption, the horizontal density of observations has a lower priority amongst the requirements discussed in this chapter. The derivation of the coverage specification is supported by weather-forecast-impact experiments, which included the inputs of the conventional

wind profile network that is spatially thin and irregular but of key importance. Moreover, the guiding coverage specification (Table 3.1) is taken from the WMO threshold requirements.

Table 3.3 provides a summary of the ADM-Aeolus measurement requirements discussed in this chapter.

As explained above, the meteorological impact in the tropics is the most certain and, from a climate point of view, also the most useful. Moreover, to improve atmospheric analysis beyond the tropics and in particular NWP in Europe, the above requirements have been chosen to allow for a positive impact of the DWL winds at high latitudes.

The implementation of ADM-Aeolus will be a major step forward, providing meteorological science with greater insight into atmospheric processes by providing, for the first time, global wind profiles. This makes this mission unique and a true explorer mission.

4. Aeolus mission implementation

4.1 Main system requirements

The mission requirements as defined in Chapter 3 were translated into system requirements to enable the implementation of the mission. In the following, the main design drivers are addressed.

4.1.1 Accuracy

The mission requires the measurement of horizontal wind velocity components from the lower part of the troposphere to the lower part of the stratosphere (up to 30 km altitude is possible). The observation of a single component of the horizontal wind velocity only is required to ease the instrument design. In Chapter 3 it was shown that the introduction of additional single component horizontal wind information significantly improves the present global observational system. Furthermore, there is no particular requirement on the direction of the horizontal wind component to be measured.

The required instrumental accuracy for the HLOS has been translated from the mission accuracy requirements (Table 3.3). The background representativeness error for a 50 km line-averaged wind component measurement was quadratically subtracted from the system accuracy requirement (2 m s^{-1} in the troposphere), yielding an instrument accuracy requirement of 1–2 m s^{-1} for the HLOS wind component. The representativeness error includes the contribution from both the horizontal and the vertical wind component.

With a direct detection lidar, the gross error is significantly smaller than the required 5% if the accuracy specification is achieved. Thus, no explicit gross-error requirement is stated.

4.1.2 Stability

While the sizing of the subsystems of the ADM-Aeolus laser instrument ALADIN (the Atmospheric LAser Doppler INstrument) is driven by the measurement accuracy requirements, the design is equally driven by the need to produce highly reproducible data throughout its lifetime. This is specified by the measurement stability requirements.

The user requirement calls for the error correlation in the horizontal, vertical and temporal domain to be below 1%. While the error correlation is well defined for the final data products, it is difficult to use this value to guide the design of ALADIN and the pointing subsystem of the Aeolus satellite. Thus, the error correlation requirement needs an interpretation to derive suitable, verifiable instrument design requirements.

From the instrument side, the key contributors to error correlation were identified as the change of the zero-wind bias value and the response slope over a time frame of several observations (Stoffelen *et al.*, 2002). Correspondingly, the zero-wind bias and the slope error have been specified to stay below 0.4 m s^{-1} and 0.7% respectively in the time frame ranging from 1 to 50 minutes.

A direct derivation of these values from the 1% error correlation requirement is not possible, but the values are considered sufficiently stringent to guarantee a very stable instrument in flight.

4.1.3 Spatial and temporal coverage

The integration length of 50 km and the measurement separation of 200 km, as specified in Chapter 3, allows the laser to be switched on for 7 s (corresponding to about 50 km observation length), and keep it switched off during the remainder of the 28 s repeat cycle (corresponding to a total ground track of 200 km). This sampling geometry over one orbit is shown in Fig. 4.1. This implies an instrument duty cycle of 25%, which leads to a reduction of the power required to drive the

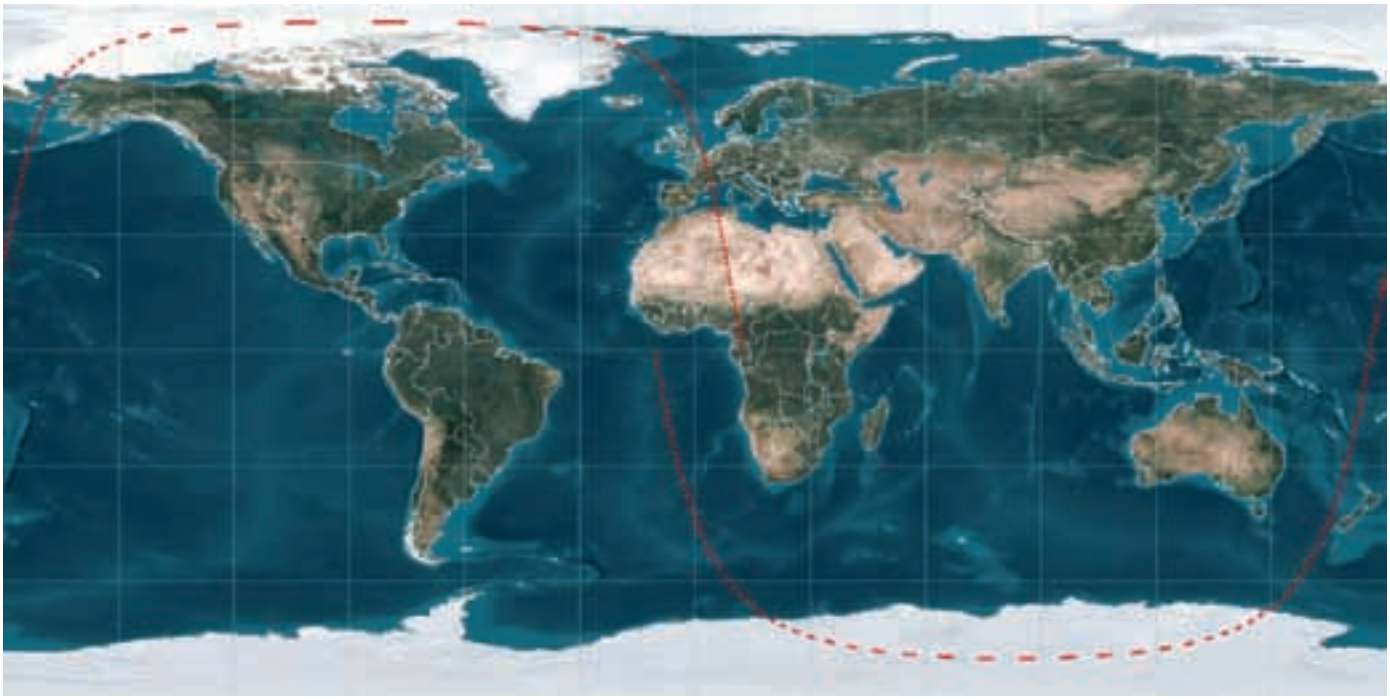

Fig. 4.1. Ground-track of the Aeolus wind observations of 50 km length and 200 km repeat spacing over an orbit. Courtesy of Astrium Satellites Ltd

laser system. The power saving from the burst mode operation is, however, less than 25% because of the required warm up of the transmitter laser.

The vertical resolution must be at least 1 km in the troposphere and the lower stratosphere, but can be increased to 2 km above about 16 km altitude. For measurements near the ground, a sampling step of 0.5 km or less is desired. Because the sampling requirements may change, it is required that the vertical sampling of the atmosphere can be adjusted during flight. Furthermore, the sampling of the Mie and Rayleigh channels must be independent, in order to allow for testing of the different sampling strategies in flight.

4.1.4 Data delivery timeliness

The requirements specify that the data should be delivered within three hours after a measurement is taken. One orbital revolution lasts about 1.5 hours, which means that it is necessary to download and immediately process the measurements once per orbit. This requires ground stations for data reception at high latitudes. Existing public data networks can distribute the data further due to its small volume.

For future applications, a shorter data delivery time is desired. An attempt will be made to deliver data for a specified region close to the ground station within 30 minutes.

The main task of the ground segment data processing centre is to derive high-quality LOS winds from the raw data. This includes the application of instrument-specific calibration procedures and instrument-specific quality control to achieve the 95% data reliability (gross error probability < 5%) requirement.

4.1.5 Summary of the main system requirements

The main system requirements, as derived from the mission requirements (Table 3.3), are summarised in Table 4.1.

Table 4.1. Aeolus main system requirements

	System Requirements	*Value*	*Origin*
Mission	Operational Lifetime	3 years	Explicit mission requirement
Instrument	Principle	LIDAR with a two-channel receiver for molecular (Rayleigh-) and aerosol (Mie-) backscatter signals	High-quality observation requirement up to 30 km altitude
	Viewing geometry	400 km altitude; 35° off-nadir looking;	System-level trade-off
	Max. altitude Vertical resolution	30 km In-flight commandable in steps of 0.25 km in range of 0.25 km to 2 km, independent for Rayleigh and Mie receivers;	
	Nominal vertical resolution profile	0.5 km in the PBL; 1 km up to 16 km altitude; 2 km above 16 km;	
	Horizontal resolution	Along-track integration 50 km, repeated every 200 km along track	
	HLOS wind-speed error (rms)	< 1 m s^{-1} from 0 to 2 km < 2 m s^{-1} from 2 to 16 km	
	Error correlation between observations (time scale up to 0.5 orbit)	< 0.4 m s^{-1} zero-wind bias < 0.7% slope error	From error correlation requirement
Velocity, Location and Pointing	Sensor LOS restitution between calibrations	< 0.3 m s^{-1}	To ensure a minimal zero wind reference error
	Yaw steering	Apparent LOS ground speed < 0.1 m/s	To make ground Doppler variation insignificant for the definition of the dynamic range of the instrument.
	Altitude uncertainty	< 250 m	Correct assignment to atmospheric layer
Data Handling, Communication	Downlink of on-board accumulated measurement and ancillary data	Once per orbit, with the capability to downlink measurement data to additional receiving stations along the orbit	System level allocation for timeliness requirement
Ground Processing	Time for generation of Level 1 data product	< 90 minutes, including time of all data transfers	

(PBL = planetary boundary layer)

4.2 Aeolus mission baseline

4.2.1 Instrument concept selection

Numerous instrument options were investigated during the early development phases, ranging from coherent lidars at 9–10 µm, 2 µm and 1.5 µm to direct detection lidars at 1.5 µm, 1 µm, 0.53 µm and 0.35 µm. Detailed performance analyses and technology reviews have been performed for all these concepts. All coherent concepts use aerosol (Mie) scattering and have similar performance behaviour, providing high accuracy at low altitude and reduced reliability above a given altitude threshold, depending on the aerosol conditions and the emitted laser energy.

4.2.1.1 Coherent detection concepts

The coherent concept at 1.5 µm was rejected because of the low transmitter maturity and efficiency. The coherent concept at 9–10 µm was investigated in more detail, but has finally been put aside, mainly because of the difficulty of developing a space-qualified CO_2 laser, coupled with low industrial interest. The 2 µm system is based on a solid-state laser that is frequently used for ground-based wind lidars.

The coherent lidar at 2 µm features high accuracy at low altitude, but is limited to medium altitudes. This restriction comes mainly from the limited potential for a significant increase in laser pulse energy for such a system. The optomechanical and thermal concept was also considered rather complex (due to the laser crystal

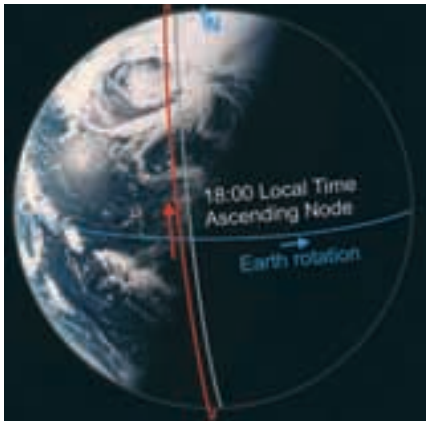

Fig. 4.2. The Aeolus dusk-dawn orbit of about 400 km altitude (red), and the measurement ground track (grey).

cooling and alignment requirements), and the programmatic risk was considered relatively high because only a single and non-European procurement source for the transmitter could be identified. Finally, the growth potential of the concept for a future operational mission is limited, since the aerosol concentration is quite low at higher altitudes.

4.2.1.2 Direct detection concepts

Concepts related to the Neodymium doped Yttrium-Aluminium-Garnet (Nd:YAG) solid-state lasers, which is the 'work horse' of pulsed laser sources, were investigated. The 1.06 μm (fundamental emission wavelength of Nd:YAG lasers) and 532 nm (first frequency harmonic, comparatively easy to obtain from the laser by adding a frequency doubling crystal) concepts were rejected because of eye-safety concerns.

The third harmonic wavelength of Nd:YAG lasers is near 355 nm. This wavelength is sufficiently far in the UV spectral region that the laser exposure limit is much higher than in the visible region, and thus much higher light energies can be transmitted towards the Earth without eye safety concerns.

In addition, the short wavelength leads to a large signal from molecular Rayleigh scattering. A direct detection UV concept at 355 nm has been developed which allows simultaneous detection of aerosol (Mie) and molecular (Rayleigh) scattering, thus allowing wind detection in aerosol rich atmospheres (e.g. in the planetary boundary layer and near the tropopause), as well as in clear atmospheres (free troposphere and the stratosphere).

The third harmonic frequency of the Nd:YAG laser output can be obtained with about 30% efficiency from a set of two non-linear crystals behind the basic laser core. This is only slightly more complex than the 1.06 μm or 532 nm concepts, and the need for eye safety makes this frequency most desirable.

The direct-detection UV concept has been selected as the baseline for Aeolus as it provides good performances up to high altitudes, and has a high potential for an operational mission. The technical and programmatic risks were evaluated as the lowest of the investigated concepts, as multiple and European supplier sources have been identified for each critical element. Finally, the growth potential for a future operational mission is sufficiently high, allowing the further development of the instrument to become fully compliant with the ideal WMO requirements (Table 3.1).

4.2.2 Orbit selection

The requirement of a global coverage calls for a high-inclination orbit. No particular requirement with respect to the local time of the wind measurements has been specified. However, measurements around sunrise/sunset may benefit from fewer cloudy observations, at least over land, because there is less convective activity than during the day. In addition, a Sun-synchronous dawn-dusk orbit provides maximum solar power and the most stable thermal environment. It has therefore been selected.

The LOS of the instrument will be 35° off nadir to ensure the best instrument performance, and 90° across the flight direction to avoid a contribution from the satellite velocity to the Doppler frequency shift. To minimise the contribution of background radiation, the instrument LOS should not point towards the Sun but in the anti-Sun direction. The selected dawn-dusk orbit will have a Mean Time of Ascending Node at 18:00 in order to provide an acceptable coverage over the North Pole. The resulting orbit geometry is depicted in Fig. 4.2.

There have been no specific requirements driving the choice of the orbit altitude. The resulting freedom has been used to optimise the mission performance while reducing the satellite and ground segment complexity. Performance simulations

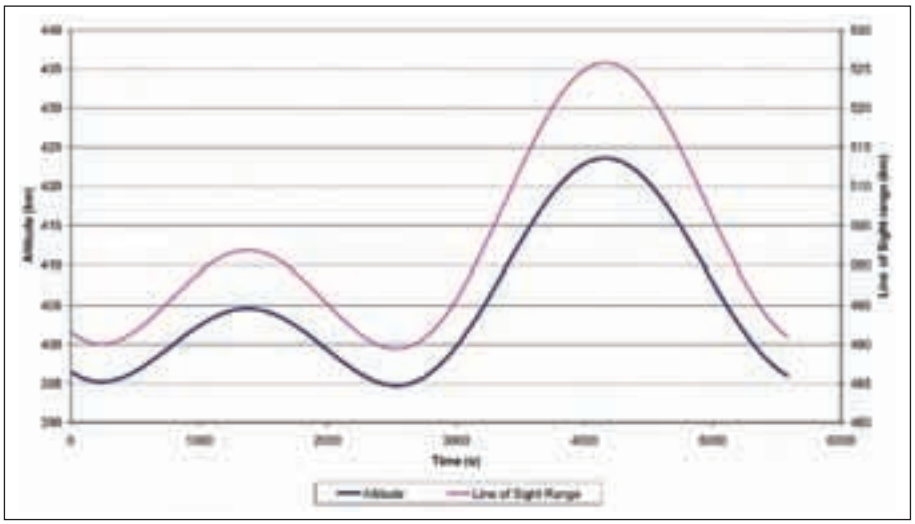

Fig. 4.3. Aeolus altitude above the Earth ellipsoid and the measurement distance throughout the selected orbit.

have been done, taking into account the main system parameters (fuel demand and frequency of orbit maintenance manoeuvres), as well as the number of ground stations required. Orbits between 350 km and 450 km altitude are best suited in order to optimise the overall system.

The selected orbit has an inclination of 97.01°. Fig. 4.3 shows the Aeolus measurement distance and the altitude above the reference Earth ellipsoid throughout a selected orbit. The mean altitude is 408 km. The orbit repeats its ground track every seven days (corresponding to 109 orbits, giving an orbit period of 92.48 minutes). With this orbit, the commanding of Aeolus is simplified, as all activities are cyclic with a weekly rhythm.

4.2.3 Overview of the Aeolus measurement concept

The measurement geometry of Aeolus is shown in Fig. 4.4. As mentioned previously, ALADIN will emit an ultraviolet light pulse (355 nm). The laser pulse will be sent towards the atmosphere in a slant angle of 35° to Nadir, orthogonal to the Aeolus ground-track velocity vector. Due to the Earth's curvature, the incidence angle at the measurement track is 37°.

In the atmosphere, a small portion of the light is scattered back by aerosol particles (Mie scattering) and molecules (Rayleigh scattering). This backscattered light is collected by the receiving telescope of ALADIN and detected as a function of time-of-flight to obtain the distance between Aeolus and the atmospheric scattering layers. The altitude of the scattering layers above the Earth ellipsoid is then computed from the known geometry.

The received signal frequency is Doppler-shifted relative to the emitted laser pulse due to the relative motion of the scatterers (including the spacecraft movement, the Earth's rotation, and the wind velocity along the line-of-sight). The spacecraft and Earth's rotation Doppler shifts are minimised by the use of a proper satellite attitude-control scheme (yaw steering mode).

The instrument thus directly measures Doppler wind shifts, which is:

$$V = \frac{\lambda}{2}\Delta f \qquad (4.1)$$

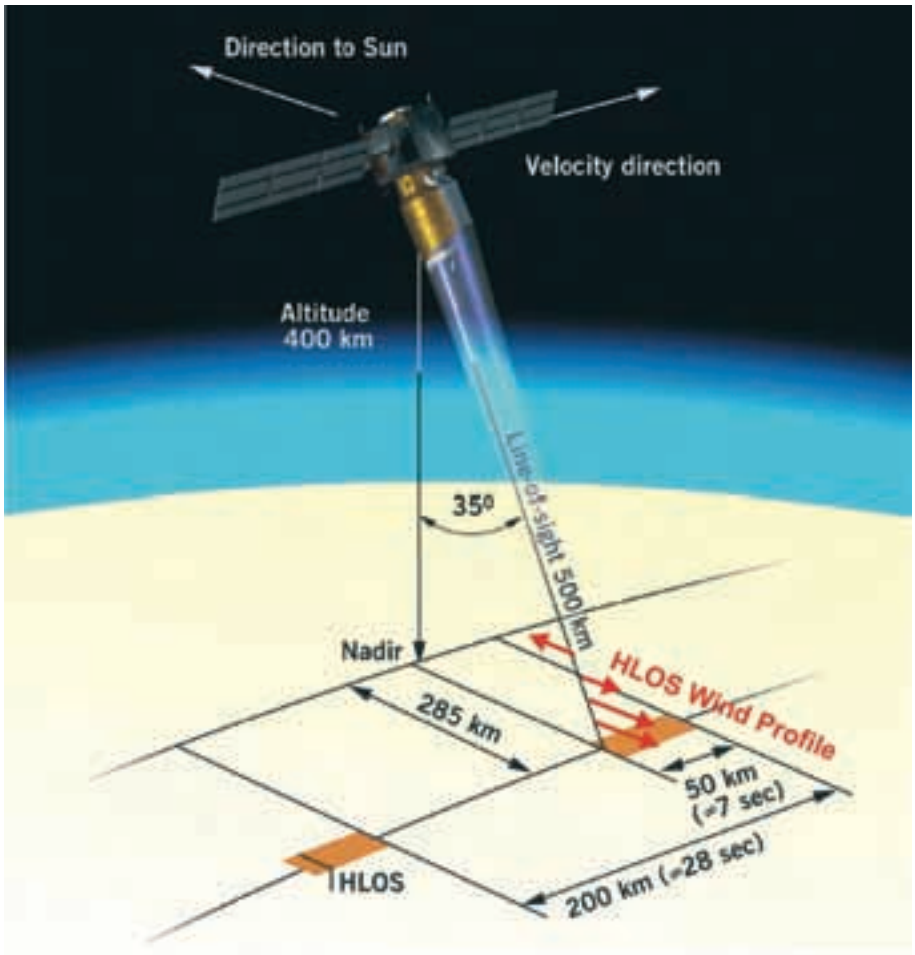

Fig. 4.4. Schematic view of the ADM-Aeolus measurement geometry.

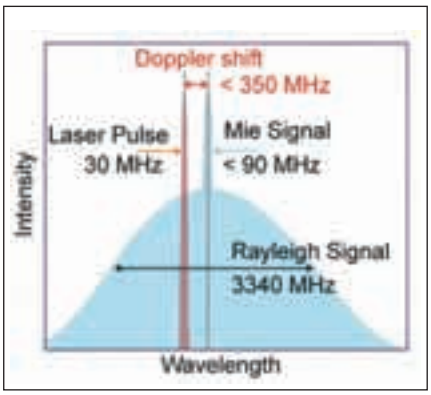

Fig. 4.5. Schematic view of the backscatter spectrum of scattering from the air molecules (Rayleigh scattering – broad blue curve), and from aerosol and cloud particles (Mie-scattering – narrow blue peak), as compared with the outgoing laser pulse (red spike).

where V (m s^{-1}) is the wind velocity along the line-of-sight, λ is the wavelength, and Δf is the frequency Doppler shift. At 355 nm, a 1 m s^{-1} line-of-sight wind velocity results in a Doppler shift of 5.64 MHz. However, because the horizontal wind in the measurement direction is projected onto the line-of-sight, a 1 ms^{-1} horizontal wind corresponds to a Doppler shift of only 3.39 MHz. With an emitted frequency of 845 THz (corresponding to 355 nm), the detection of a 1 m s^{-1} horizontal wind translates into a resolving power of 2.5×10^8 – thus very good spectrometers and a good signal-to-noise ratio are mandatory to meet the measurement requirements. Aeolus relies on pulse averaging to achieve the good signal-to-noise ratio.

The receiver samples the signal sequentially in order to determine its arrival time and hence the distance to the scattering atmospheric layer. For each layer, the spectral distribution of the return signal is analysed through a high-resolution spectrometer. Direct detection is used to measure the spectrum, requiring low-noise (quasi photon-counting) detectors, which are available for the selected ultraviolet wavelength.

As shown in Fig. 4.5, the return signal spectrum is the sum of a wide-bandwidth Rayleigh signal due to molecular scattering (about 3340 MHz FWHM (full width at half maximum) in the upper troposphere) and a narrow-bandwidth Mie signal due to aerosol scattering (less than 90 MHz typically).

Various techniques are available to measure the Mie and Rayleigh spectrum central frequency and they fall into two categories: fringe-imaging and edge techniques. An extensive trade-off was made between these two options during the early development phases, both in terms of performance and the technical implementation.

The fringe imaging technique will be used for the Mie receiver (Fig. 4.6). This concept was preferred over the edge technique as the latter is too sensitive to the Rayleigh background in the ultraviolet. It is intended to sample the received spectrum with a resolution compatible with the spectrum width. A centroid computation then provides the location of the spectrum centre. The fringe width obtained is set by the spectrometer resolution. After multichannel sampling, the fringe spreads over a few spectral intervals. The fringe is superimposed on the Rayleigh and atmosphere radiance spectra, which provide additional noise. This noise is kept negligible by making use of blocking spectral filters.

The double edge technique is used for the Rayleigh receiver (Fig. 4.7). This concept was preferred over the fringe imaging technique, which has a similar performance but whose implementation imposes tighter alignment and detector requirements. Two filters are placed symmetrically from the centre wavelength position in order to perform a differential measurement. The filter outputs (A and B) are used directly as the estimator for the frequency shift.

The receiver concept proposed for ALADIN is capable of using both measurement principles simultaneously.

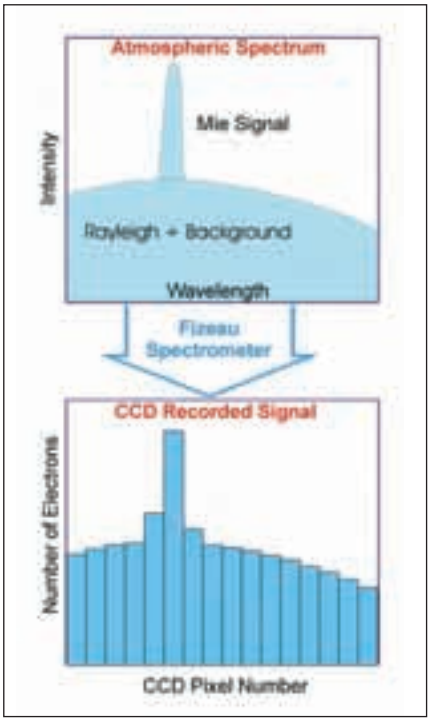

Fig. 4.6. Mie receiver fringe imaging principle.

4.2.4 Measurement averaging and spatial resolution

The mission requirements call for observations of wind profiles that are averaged over a 50 km distance. Wind profile observations should be about 200 km apart, to provide independent information to the weather prediction models (as indicated in Fig. 4.1). These requirements drive the horizontal sampling properties of Aeolus.

For a ground track velocity of 7.21 km/s, the 50 km averaging distance corresponds to a duration of about 7 s, and the 200 km spacing of the observations corresponds to about 28 s. This defines the Basic Repeat Cycle (BRC) of Aeolus observations: 7 s measurements repeated every 28 s.

For technical reasons, the maximum pulse rate of the laser is about 100 Hz; thus a wind profile observation is bound to contain about 700 individual lidar measurements. However, to limit the data bandwidth, and to improve the overall measurement performance, individual laser signals can be co-added on board to form a measurement. The onboard averaging extends over 15 to 50 laser pulses, depending on the measurement scenario. Thus a wind observation consists of 14 to 46 measurements which are downlinked to ground for further processing.

Fig. 4.7. Rayleigh receiver double edge principle.

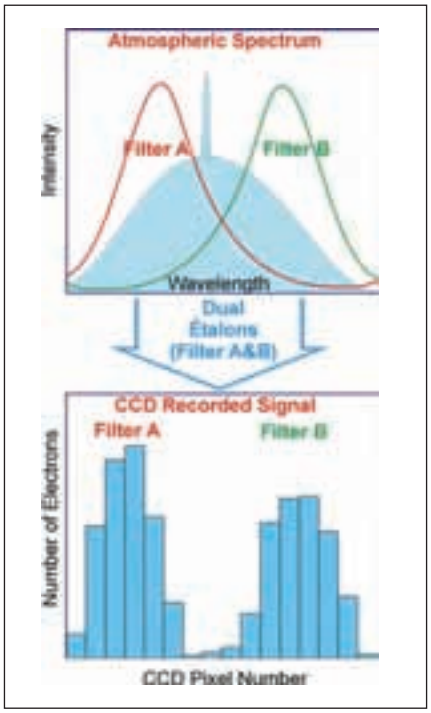

4.3 ALADIN design

4.3.1 ALADIN overview

Fig. 4.8 shows a block diagram of ALADIN, indicating all subsystems and their interfaces to the Aeolus spacecraft. The blue part is the instrument core, which comprises all optical subsystems. The electrical panel is located in the Aeolus satellite bus.

Figs. 4.9 and 4.10 show renderings of the instrument core of ALADIN. Fig. 4.11 shows the actual ALADIN Optical-Structural-Thermal Model (OSTM), which is identical in all physical parameters with the Flight Model.

The pictures give an impression of the size and complexity of ALADIN; the 1.5 m diameter telescope with its baffle dominates the instrument. Due to the powerful laser package, its average power consumption is 830 W (1030 W peak), which is a primary driver for the platform design. The mass of ALADIN

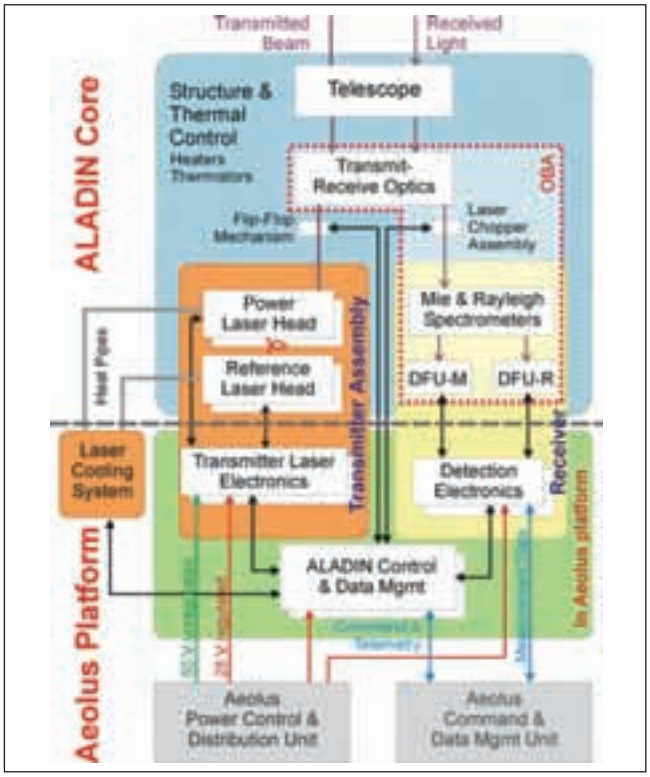

Fig. 4.8. Functional diagram of ALADIN showing the major subsystems and their key interfaces to the Aeolus platform.

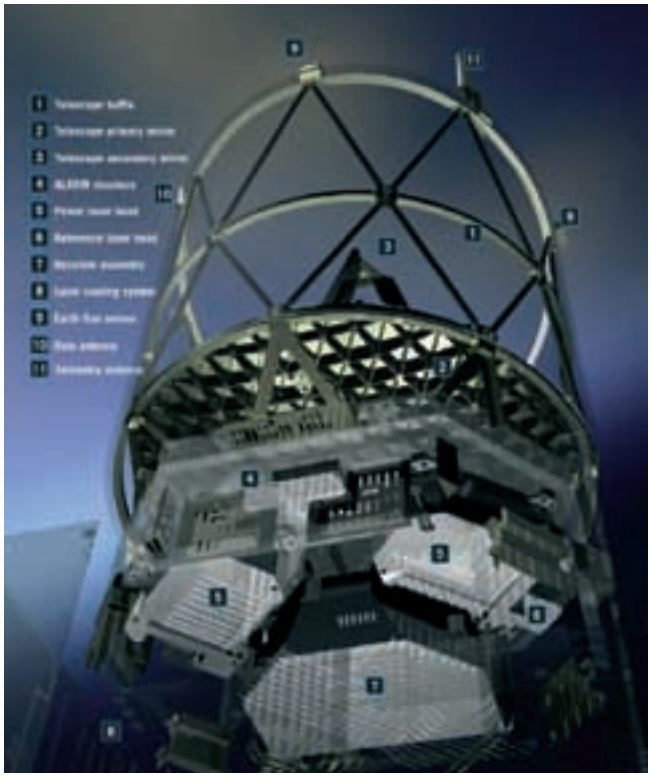

Fig. 4.9. Artist's view of ALADIN with the laser radiator attached. The laser radiators are mounted on the eclipse side of the satellite bus.

(including electronics boxes and harnesses) is about 480 kg. This is about half of the complete Aeolus satellite dry mass.

The telescope is the largest element of ALADIN; its size is limited by the fairing diameter of the envisaged small launchers for Aeolus. A baffle is required to avoid direct sun illumination of the telescope secondary mirror and the mounting struts, as well as a protection against atomic oxygen in space. The Sun-remote side is cut down to reduce mass and air drag. On the upper ring, it carries the antennas for the data downlink (X-band) and telemetry and telecommanding (S-band), as well as the Coarse Earth/Sun Sensors for the attitude and orbit control system.

Below the telescope is the ALADIN structure, which carries the laser heads and the optical bench assembly. The laser heads are coupled via heat pipes to the large radiator on the side of the spacecraft, used to control the temperature of the lasers. The Optical Bench Assembly (OBA) is a stiff carbon-fibre bench carrying the transmit-receive optics as well as the Mie- and Rayleigh spectrometers (MSP and RSP), and the detection front-end units (DFU) for each receiver, with the signal detectors. special charge-coupled devices (CCDs) with on-chip storage cells to allow signal accumulation. With accumulation, detection can approach the shot-noise limit, the ultimate detection sensitivity.

The ALADIN detector outputs are digitised and formatted for downlink in the Detection Electronics Unit (DEU). The Transmitter Laser Electronics (TLE) handles the power conditioning of the lasers as well as the overall laser thermal and logical control. The ALADIN Control and Data Management unit

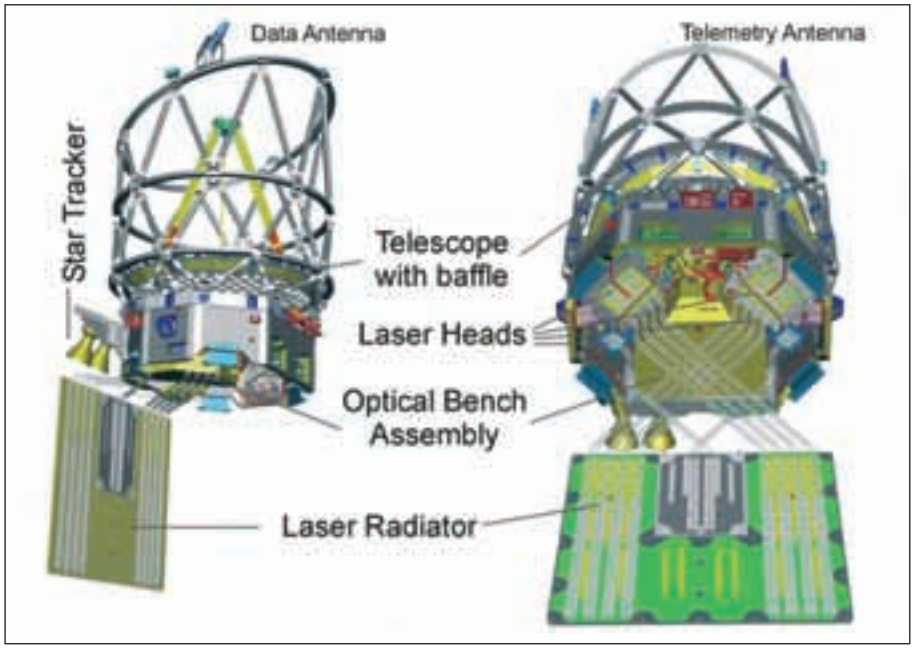

Fig. 4.10. View of the ALADIN optics module, including transmit/receive telescope of 1.5 m diameter, the transmitter laser heads with the large cooling radiator, and the optical bench assembly with the transmit/receive optics and the Mie and Rayleigh receivers. Courtesy of Astrium Satellites SAS.

(ACDM) supervises the overall functioning of ALADIN and communicates with the Aeolus Command and Data Management Unit (CDMU).

Autonomous star trackers determine the attitude of the Aeolus spacecraft. They are mounted directly on the ALADIN structure to minimise misalignment errors.

The actual arrangement of the laser heads and the OBA in the ALADIN structure (OSTM) can be seen in Fig. 4.12.

4.3.2 ALADIN optical architecture

Fig. 4.13 shows the schematic optical architecture of ALADIN. The main subgroups of transmitter, telescope and receiver are visible.

A baseline decision for the ALADIN optical architecture has been the selection of a monostatic concept; that is, the same telescope is used to transmit and receive the light pulse back from the Earths atmosphere. Here the transmitter laser beam is combined with the receiver optical path before the telescope. The overall magnification of the telescope is 150, which relaxes the angular adjustment tolerances by this factor. Thus comparatively large tolerances of 0.75 mrad are achieved for the relative alignment between transmitted laser pulses and the receiver optical axis, and no active mechanism for realignment in flight is required.

The light pulses are generated by the Transmitter Assembly (TXA), a diode-pumped frequency tripled Nd:YAG laser. It generates narrow frequency light pulses near 355 nm wavelength, with about 120 mJ energy per pulse and a pulse repetition frequency of 100 Hz. Each pulse has a duration near 30 ns (corresponding to a physical length of 9 m). Thus the optical power in each pulse is about 4 MW.

The light pulses are transmitted via a polariser and a circular polariser in the transmit-receive optics to the telescope, where they are expanded to 1.5 m in diameter. The overall magnification is about 150, achieved in two steps. This leads to a strong reduction of the beam divergence; the divergence of the transmitted beam is reduced to about 12 µrad, and the spot size of the beam on the ground in 500 km distance is only some 12 by 15 m.

Fig. 4.11. ALADIN Optical-Structural-Thermal Model (OSTM), which is identical in all physical parameters with the Flight Model.

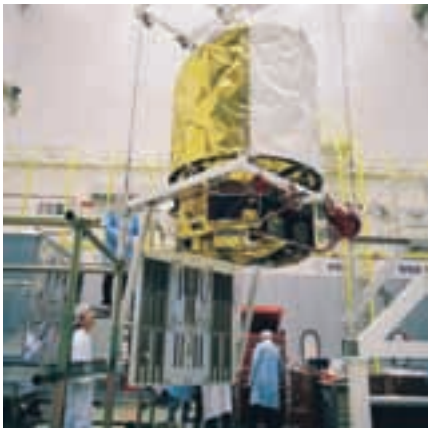

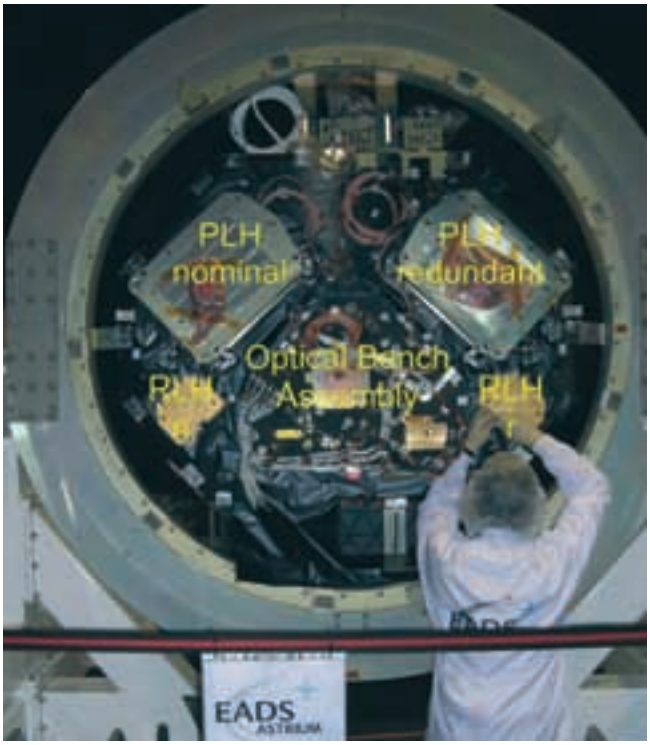

Fig. 4.12. Arrangement of the laser heads and the Optical Bench Assembly in the ALADIN OSTM.

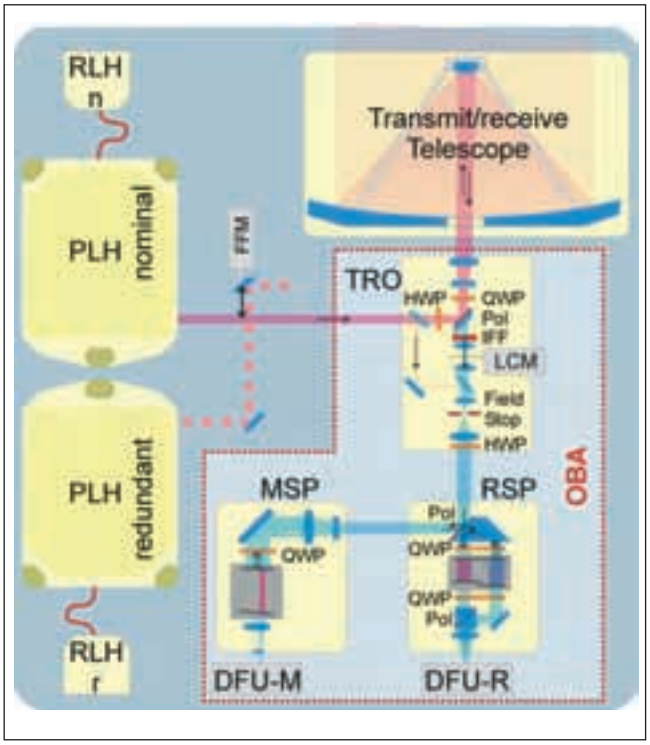

Fig. 4.13. Optical architecture of ALADIN. PLH: Power Laser Head, RLH: Reference Laser Head, FFM: Flip-Flop Mirror, LCM: Laser Chopper Mechanism, TRO: Transmit/Receive Optics, RSP: Rayleigh Spectrometer, DFU: Detection Front-end Unit, QWP: Quarter-Wave Plate, HWP: Half-Wave Plate, Pol: Polariser, IFF: Interference Filter.

About 3 ms after the transmitted light pulse has left the telescope, the received signal is collected. It is collimated in the telescope to a 36 mm beam, which passes the polariser in the transmit-receive optics. The depolarised portion of the backscatter signal is discarded. It then enters the field stop to limit the field-of-view to about 19 µrad. A chopper is located near the field stop to prevent stray light from the transmitted pulse from entering the receiver optics, where it could blind the sensitive detectors.

Another function of the transmit-receive optics (TRO) is to block broadband background radiation. A band pass filter with 1 nm spectral width and 80% peak transmission is used to filter background radiance near 355 nm wavelength, which can reach up to 160 W/m^2/sr/µm on the summer hemisphere. For broadband rejection, a low-spectral-resolution prism spectrometer is built into the TRO. Total optical transmission of the background rejection chain is over 60%.

From the field stop, the light is guided to the Rayleigh- and Mie Spectrometers (RSP and MSP). It is first reflected on the RSP to the MSP, a Fizeau spectrometer. This transmits only a fringe at a location. The location of the fringe indicates the frequency of the light signal, which is recorded by the Accumulation CCD (ACCD).

About 70% of the incoming photons are reflected back to the RSP. This is a set of two Fabry-Pérot etalons with slightly different thicknesses (Garnier and Chanin, 1992; Chanin *et al.*, 1994; Rees *et al.*, 1996; Flesia and Korb, 1999). The

Table 4.2. Summary of key performance parameters of ALADIN.

	Parameters	*Value*
Platform	Altitude	400 km
	Orbit	Sun-synchronous 6 h – 18 h
	Nadir slant angle	35°
Transmitter	Wavelength	355 nm
	Pulse energy	120 mJ
	Repetition rate	100 Hz
	Line width	30 MHz
	Duty cycle	42%
Transmit-receive Telescope	Telescope diameter	1.5 m
	Telescope magnification	41.67
	Telescope transm. (incl. obscuration)	> 80%
	Transmitter beam divergence (full angle)	12 µrad
	Receiver Field-of-View (full angle)	19 µrad
Receiver	Fizeau interferometer (Mie)	
	Free Spectral Range	2.2 GHz
	Useful Spectral Range	1.5 GHz
	Fringe width (FWHM)	145 MHz
	Double Fabry-Perot (Rayleigh)	
	Free Spectral Range	10.9 GHz
	Spacing	5.5 GHz
	Detector quantum efficiency	> 80%
Signal Processing	Altitude range (Mie + Rayleigh)	-1 to +30 km
	Vertical resolution	adjustable from 0.25 to 8 km
	Horizontal accumulation length	1 or 3.5 km
	Processing integration length	50 km

transmission of the first etalon is on the short-wavelength side of the backscatter signal, while the other one is on the long wavelength side. If they are symmetrical to the received line, the difference of the signals transmitted by the etalons is near zero. When the spectrum of the backscattered light is not symmetrical to the etalon transmission curves, the difference in the signals becomes positive or negative (see Fig. 4.7). The normalised difference is a direct measurement of the frequency shift from the central position. This response slope, however, is dependent on the shape of the incoming spectral line.

The RSP uses polarisation switches to direct the light sequentially through the two etalons. Thus all received photons are used in the ALADIN receiver.

Table 4.2 summarises the key parameters of ALADIN. The design of the key ALADIN subsystems is described in more detail in the following sections.

4.3.3 Transmitter laser assembly

4.3.3.1 Overview

The transmitter laser is the most challenging technology development of the Aeolus satellite: it has to provide powerful, near-monochromatic light pulses, with best possible efficiency, in a compact and lightweight package, conductively cooled, with a lifetime of three years of continuous operation without the possibility of any maintenance. In addition, some power reduction is expected by operating the laser in burst mode: it is switched on during the 5 s laser warm-up and (emitting at full power) during the 7 s of wind observations, and off during the remaining 16 sec of the 28 sec basic repeat cycle. The major transmitter laser requirements are summarised in Table 4.3. While all individual requirements have been met by other laser systems, no single laser has been designed before to fulfil this complete set of requirements.

The selected configuration is a diode-pumped Nd:YAG laser system operating in the near-infrared spectral region at 1064 nm, with a frequency tripling stage to

Table 4.3: Major transmitter laser requirements.

Parameters	*Value*
Type	Solid-state laser
Laser cooling	Conductively, via cold plate
Emission wavelength	355 nm
Pulse energy	120 mJ
Pulse repetition rate	100 Hz
Burst mode operation	7 s on, 28 s repeat cycle
Burst warm up	< 5 s
Pulse width	30 ns
Spectral width (FWHM)	< 30 MHz
Frequency jitter	< 4 MHz rms
Output beam diameter	7.5 mm
Output beam divergence	< 0.4 mrad full angle
Pointing jitter	< 0.04 mrad
Output wavelength tuneable	± 7.5 GHz
Lifetime in space	39 months
Burst-mode cycles	3.6 Mega-bursts
Total laser pulses	2.6 Giga-shots

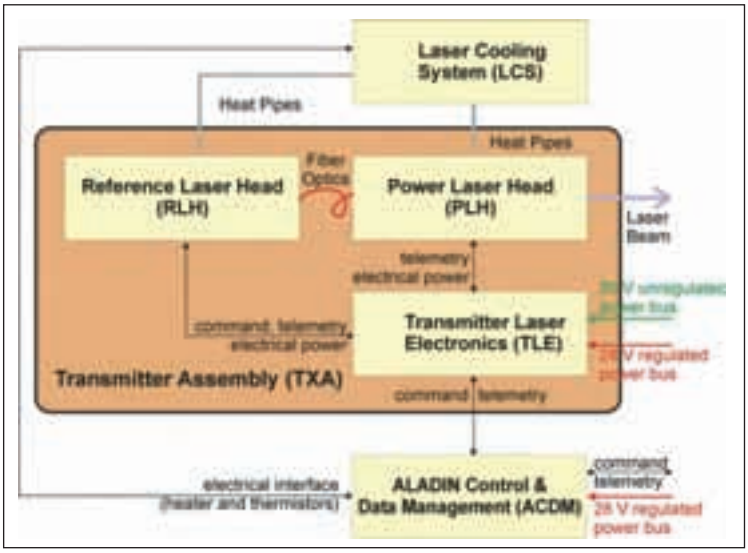

Fig. 4.14. The major building blocks of the Transmitter Assembly and its interfaces to ALADIN and the Aeolus platform.

generate the third harmonic at 355 nm. The major building blocks of this laser system are shown in Fig. 4.14.

The Reference Laser Head (RLH) is a frequency stabilised low power continuous Nd:YAG laser (1064 nm) with high inherent frequency stability. It is designed to provide frequency tunability over a range of ±2.5 GHz at the fundamental wavelength, which corresponds to the required ±7.5 GHz tuning range in the UV.

The output beam of the RLH is guided by a single mode optical fibre to the Power Laser Head (PLH) that generates the high power UV pulses. In the PLH, the RLH output is coupled into a low power master oscillator, which generates short (30 ns duration) 100 Hz single frequency laser pulses of about 8 mJ, the master oscillator is running in steady state without interruption to maintain single frequency operation. The output of the low power oscillator is then amplified in a double path preamplifier and final power amplifier. The second and third harmonic generation crystals are placed behind the power amplifier. After frequency tripling, the laser produces about 120 mJ in the ultraviolet (355 nm) (further explained in Section 4.3.3.3).

The Transmitter Laser Electronics (TLE) supplies the current to drive the pumping laser diode arrays, controls the frequency locking of the master oscillator to the RLH frequency, monitors the various electrical and optical housekeeping points, supervises the overall timing and functioning of all subassemblies, interprets the commands coming from the ALADIN control unit and returns telemetry parameters.

The Laser Cooling System (LCS) controls the temperature of the laser heads with a 1K accuracy. A set of heat pipes (8 for each PLH, two for each RLH) transports the excess heat to a large radiator on the anti-Sun side of the platform. The temperature is controlled with heaters. The heat pipes from each laser system are arranged such that the laser system can be tested on ground.

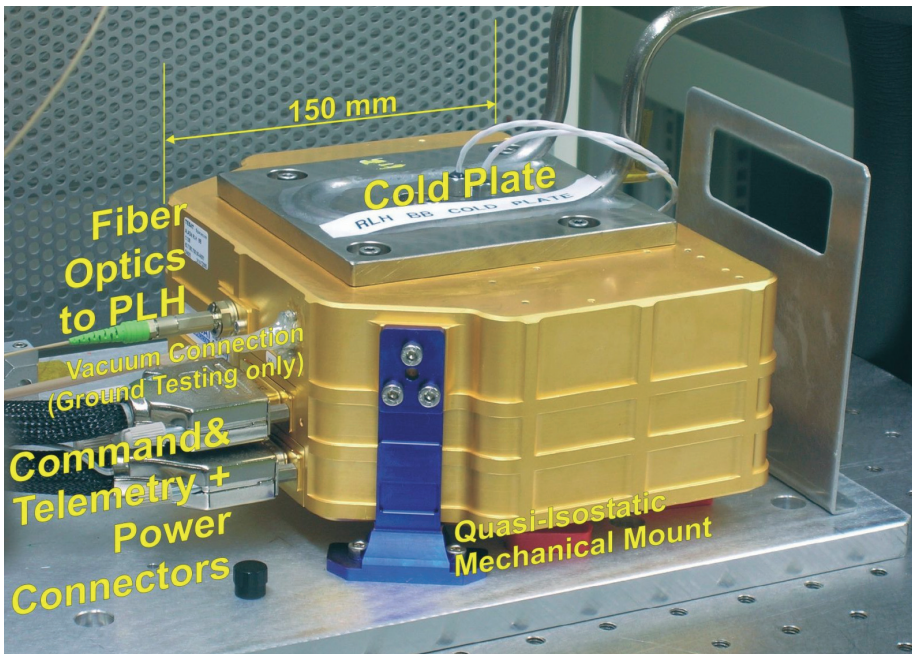

Fig. 4.15 The Flight Model of the Reference Laser Head. Courtesy of Galileo Avionica.

4.3.3.2 Reference laser head

The reference laser head is composed of two small non-planar Nd:YAG ring lasers, frequency-locked by means of a Phase-Locked Loop (PLL). The basic architecture is shown in Fig. 4.15.

One laser head is locked to an ultra-stable etalon and acts as an onboard frequency reference. The second laser is tuneable with respect to this frequency standard and acts as the seed laser for the pulsed master-oscillator laser. During measurements, the frequency is stabilised within a small portion of the receiver bandwidth. During receiver response calibration, the seeder frequency is shifted from the reference laser by a known offset in the range of 6 GHz, using the PLL. The RLH is derived from the transmitter laser of an optical communication laser for inter-satellite links.

The lasers themselves are very small monolithic ring lasers made from a single Nd:YAG crystal. They are pumped with continuous-wave Ga:Al:As laser diodes with high power stability. The laser wavelength is tuned via the crystal temperature (slow tuning) or piezo-actuator (fast tuning).

The reference laser head is an autonomous package with a mass of about 2.1 kg. Two heat pipes attached to the cold plate transport the heat to the radiator on the side of Aeolus, and heaters on the cold plate stabilise the temperature.

4.3.3.3 Power laser head

The power laser head is significantly more complex. Fig. 4.16 shows the optical architecture of this device, which is divided into different stages. Each of these stages is, in itself, a complex optical system with demanding design challenges.

The light path begins with the optical single-mode fibre (bottom) carrying the RLH output. After shaping, this radiation is phase-matched to the pulsed master oscillator cavity. The resonator of the Master Oscillator (MO) is folded by mirrors to fit into the allocated volume. A single laser diode stack pumps the low-power oscillator; a second stack is used for internal redundancy.

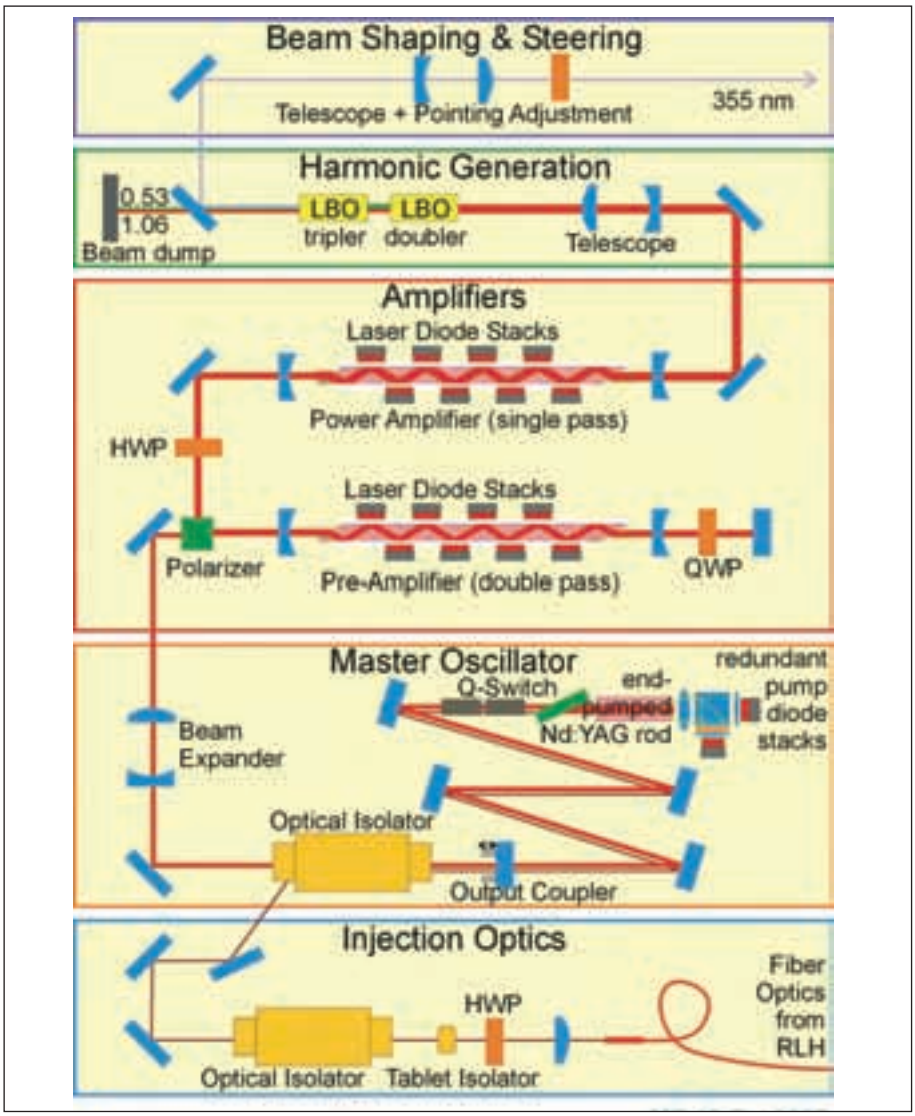

Fig. 4.16. Optical architecture of the Power Laser Head. QWP: Quarter-Wave Plate, HWP: Half-Wave Plate.

The output pulses from the Master Oscillator are amplified in two amplifiers, the first in double pass and the second in single pass. The active medium in each amplifier is a Nd:YAG zigzag slab that is side pumped by a total of eight laser diode stacks. The slabs are conductively cooled via the mounting structure. To save power, the amplifiers are operated in burst mode. Warm-up duration of 5 sec is required to reach full performance. After the second amplifier, a pulse energy of about 400 mJ at a wavelength of 1064 nm is obtained.

The pump laser diode stacks are shown in Fig. 4.17: each emits a peak power of about 700 W, with a duration of about 200 μs. Each stack is manufactured from 12 individual diode laser bars, and each bar comprises 69 multi-emitters. The typical lifetime of these diodes is about $5 \cdot 10^9$ shots which covers the in-orbit lifetime of 3 years and the on-ground integration and test time with margins. For proper pumping of the Nd:YAG crystals, the laser diode stacks have to be temperature controlled to about 1 K.

The next stage of the Power Laser Head is the harmonic generation stage, which is a set of non-linear Lithium-Triborate (LBO) crystals. If properly adjusted, these crystals have a conversion efficiency of over 30% from 1064 nm to

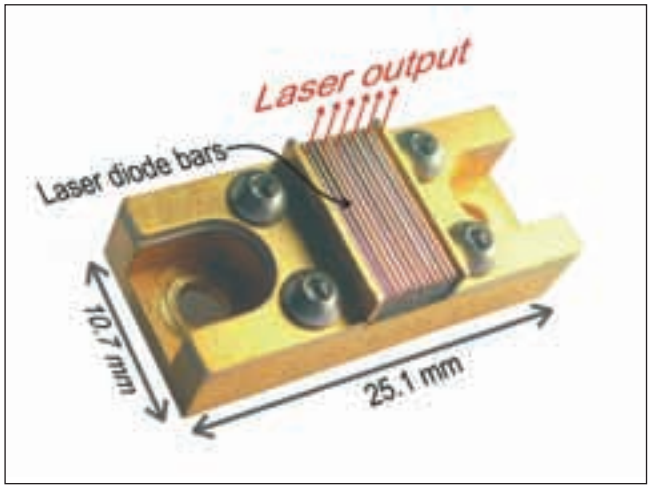

Fig. 4.17. Laser diode stack as used to pump the master oscillator and the power amplifiers to the ALADIN transmitter laser. Each diode stack is rated for 1000 W optical output power, but for Aeolus it is operated at about 700 W optical output. Each power laser head uses 18 diode stacks to pump oscillator and amplifiers. Courtesy of Quantel Laser Diodes.

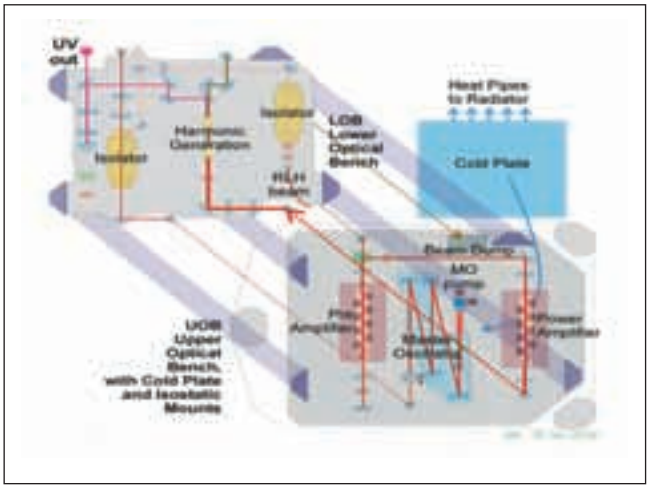

Fig. 4.18. Optical layout of the power laser head, with the active optical bench UOB (bottom), and the passive optical bench LOB (top).

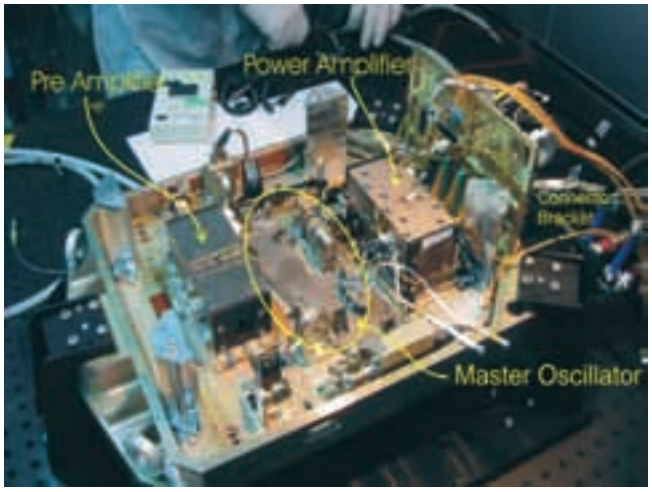

Fig. 4.19. Power Laser Head Upper Optical Bench (UOB) carrying the active elements. The UOB is the lower element during PLH integration. Photo courtesy of Galileo Avionica.

Fig. 4.20. Power Laser Head Lower Optical Bench (LOB) carrying the passive elements. The LOB is seen in the laser housing, with the lid open. Photo courtesy of Galileo Avionica

355 nm, thus generating pulses of 120 mJ energy in the UV. In a dichroic optical filter, the UV beam is separated from the residual IR and visible beams, which are absorbed in a beam dump.

In a final stage, the properties of UV beam (beam diameter, fine pointing) are adjusted to suit the ALADIN optics. In this section, an alignment beam can be coupled in to aid the alignment of the PLH with the ALADIN optics. This stage is different for the nominal and the redundant laser heads.

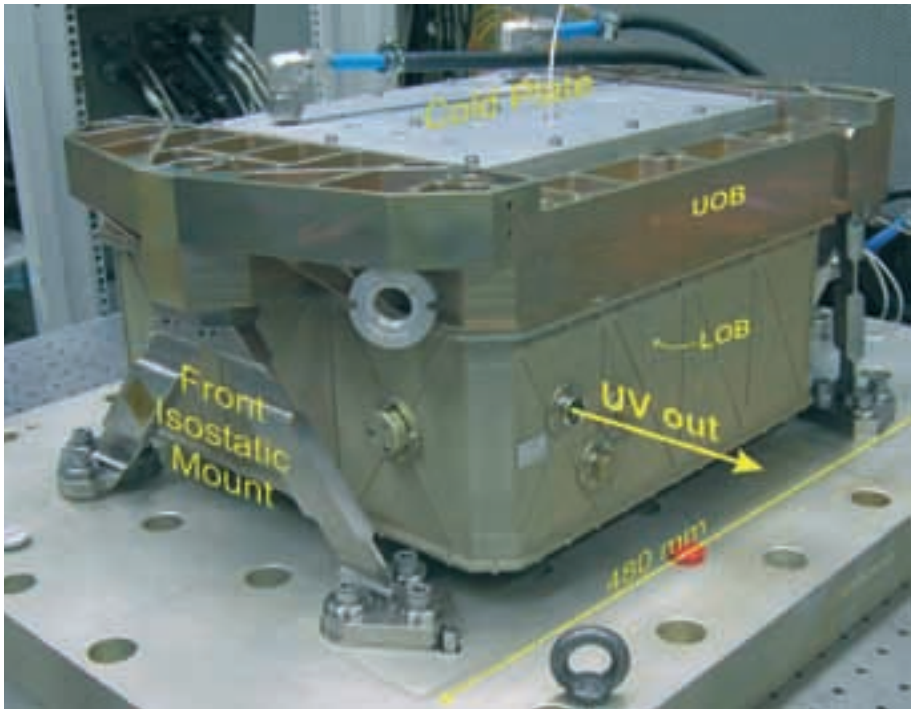

Fig. 4.21. Power Laser Head in flight configuration with the enclosure sealing the optics from the environment. Cold plate in this picture is a water-cooled plate used for ground operation; a heatpipe arrangement replaces it on satellite. The massive isostatic mounts under the UOB (now on top) are clearly visible. Mass of the PLH is 27 kg, and the maximum dimensions of the PLH box are about 480 x 350 x 180 mm. Photo courtesy Galileo Avionica.

Fig. 4.22. Exploded view of the lightweight transmit-receive telescope in SiC technology. M1: primary mirror of 1.50 m diameter, M2: secondary mirror, I/F: interface, ISM: isostatic mounting structure, MS: mounting structure. Courtesy of Astrium Satellites SAS.

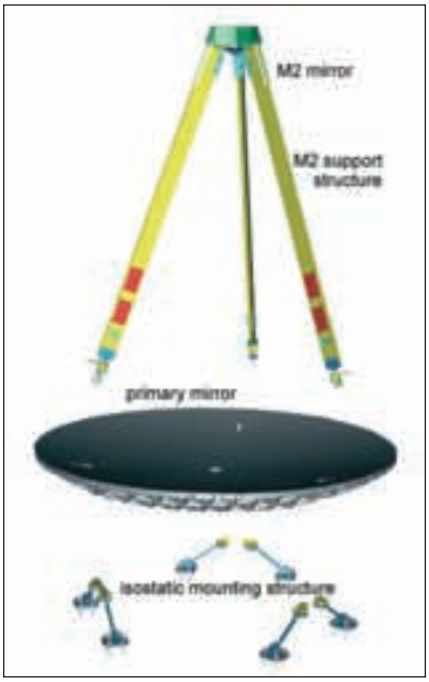

The actual implementation of the PLH is significantly more complex than indicated in the optical architecture: due to a volume constraint, the laser has to be packaged on two optical benches. The lower bench is directly coupled to the heat pipes of the laser cooling system and carries all active assemblies (the master oscillator and the two power amplifiers), while the upper bench carries the passive optics (coupling optics, isolators and the tripling stage).

Fig. 4.18 shows the optical layout of the PLH with the Upper Optical Bench (UOB) (shown on the bottom), and the Lower Optical Bench (LOB) (shown on the top). The different stages shown in the PLH architecture are divided into two optical benches in the actual laser head: the Upper Optical Bench, and the Lower Optical Bench inside the laser housing. The terms upper and lower refer to the final configuration of the PLH in the ALADIN structure; during assembly and integration of the PLH, the Upper Optical Bench is on the bottom, while the LOB is on top and often separated from the UOB by stand-offs to allow better access to optical components.

The UOB carries the cold plate, which allows cooling of the active components (Master Oscillator and the Pre- and Power Amplifiers). It also carries the isostatic mounts, which fix the PLH onto the ALADIN structure. These isostatic mounts have to maintain alignment of the output beam with respect to the ALADIN optics under the varying forces acting on the cold plate.

Fig. 4.19 shows the UOB with the Master Oscillator in the centre, preamplifier on the left and the power amplifier on the right. The folding mirrors of the Master Oscillator are mounted on an Invar substructure for additional stability.

The LOB is shown in Fig. 4.20. It carries the passive components (optical isolators and Harmonic Generation Section), and the many optical elements required for beam steering and beam shaping.

The completed and closed PLH is finally shown in Fig. 4.21. The box encloses the PLH completely and avoids contamination of the optics. During ground

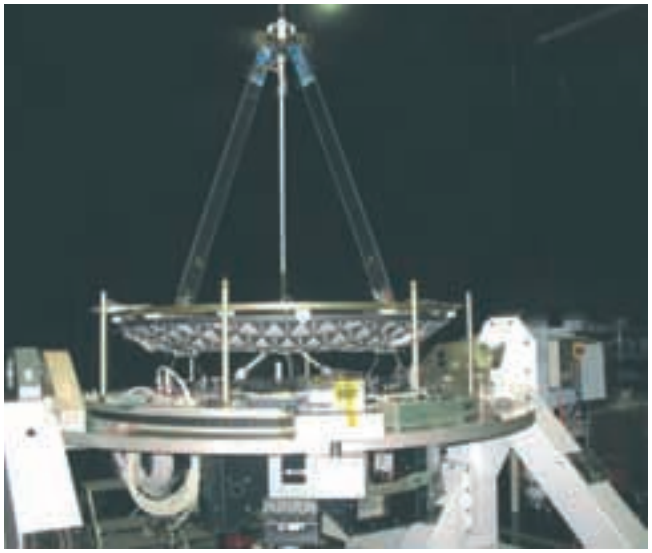

Fig. 4.23. The completed Aeolus 1.5 m transmit/receive telescope during tests in the clean room of Astrium. Courtesy of Astrium Satellites SAS.

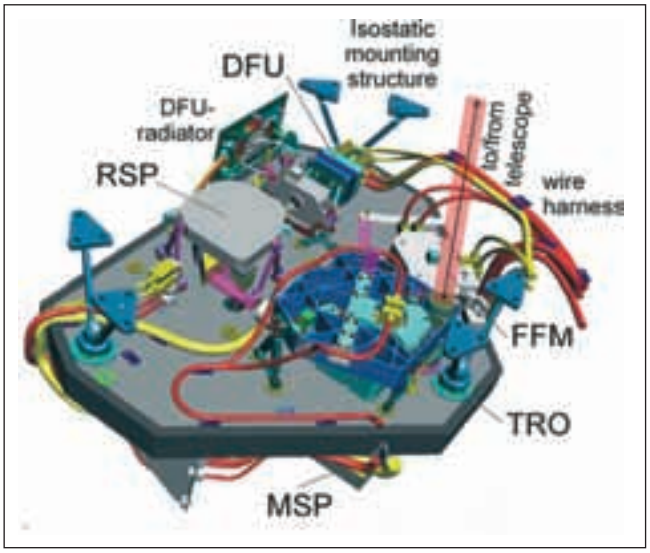

Fig. 4.24. Optical Bench Assembly with its subsystems as seen from the telescope side, including the electrical harness. DFU-R/M: Rayleigh/Mie Channel DFU, other abbreviations: see text. Courtesy of Astrium Satellites SAS.

operation, the laser head is purged with clean air. In space, the laser is operated in vacuum.

The laser electrical efficiency is about 1.2%, and the power consumption in emitting mode is near 1000 W. Due to burst operation, the average power consumption is only 450 W. The mass of the PLH is about 27.1 kg, and that of the RLH 2.1 kg. The complete TLE weighs 22.2 kg, so that the complete TXA has a mass of only 51.5 kg (without the electrical harness, which weighs an additional 6 kg m^{-1}).

4.3.4 Transmit-receive telescope

The transmit-receive telescope is the largest optical component of ALADIN. It has a diameter of 1.5 m. It is a Cassegrain optical configuration, and has an *f*- number of 0.9 for small height. It has a magnification of 41.7, thus creating a collimated output beam of 36 mm diameter. Fig. 4.22 shows an exploded view of the telescope.

The telescope is a lightweight construction using Silicon Carbide (SiC) ceramic for the primary and secondary mirrors as well as the mounting struts. SiC has a higher stiffness to mass ratio than classical materials such as Zerodur or metallic materials, and combines this with a high ratio of thermal conductivity with respect to the coefficient of thermal expansion. Thus, it is ideal for providing the best stability under global temperature variations, which is required to maintain a low wave front error of the collimated output beam under all thermal conditions.

The large primary mirror is manufactured from two SiC parts, which are brazed together after sintering. The complete mirror is lightweight, with a mass of only 53 kg. The total mass of the telescope assembly including the mounting struts is about 70 kg. Fig. 4.23 shows the completed Aeolus telescope during testing.

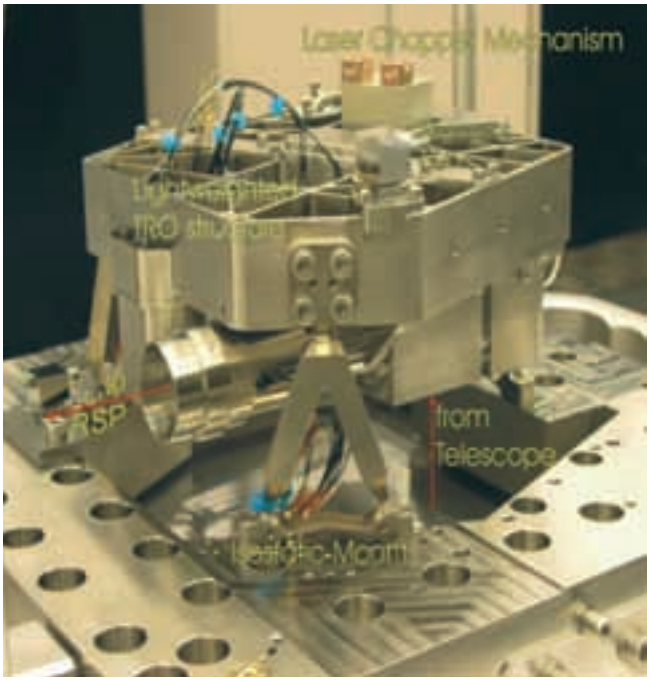

Fig. 4.25. Transmit-Receive Optics during integration in the Optical Bench Assembly. Photo courtesy of Astrium Satellites SAS / Kayser-Threde GmbH.

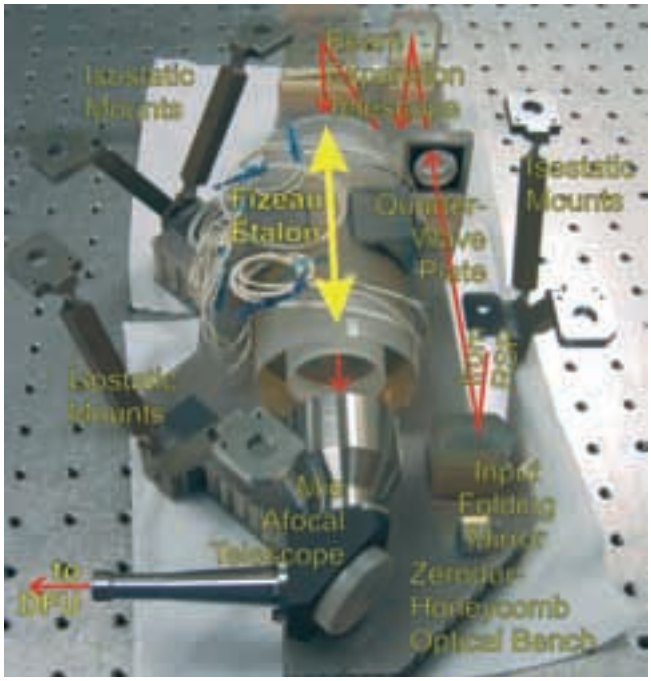

Fig. 4.26. The Flight Model of the Mie Spectrometer with the Fizeau etalon and the associated optics. Photo courtesy of Oerlikon Space.

The collimation can be adjusted in flight by tuning the temperature of the primary mirror and the struts via built-in heaters. The predicted residual wave front error stays below 300 nm, with a variation below 15 nm during the thermal cycle of one orbit, and a negligible long-term shift, which has good margins with respect to its requirements.

4.3.5 Optical bench assembly

4.3.5.1 Overview

The Optical Bench Assembly (OBA) carries the optical subsystems of ALADIN. These subsystems are arranged on both sides of a stiff carbon-fibre base plate, as shown in Fig. 4.24. The light passes from one side to the other, from the RSP to the MSP and back. Also mounted on the OBA is the Flip-Flop Mirror (FFM), which directs the nominal or the redundant transmitter laser into the transmitter light path. The figure also shows the electrical wiring harnesses and connector brackets required to provide heater and control inputs to the subsystems, and to carry the sensor readouts back to the electronics units.

The OBA is mounted onto the ALADIN structure. A carbon-fibre housing covers the OBA, to reduce the thermal gradients. Like everything in ALADIN, the OBA and all its subsystems are designed for high thermal stability to meet the stringent performance requirements.

4.3.5.2 Transmit-receive optics

The Transmit-Receive Optics (TRO) is an essential part of ALADIN: it relays the transmitter light pulse to the telescope, and shapes the received signal spatially and spectrally before it feeds it to the receiver. It must satisfy a number of criteria:

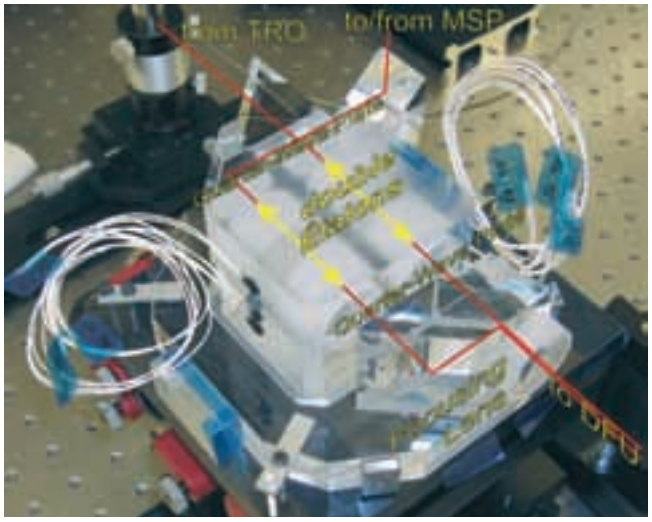

Fig. 4.27. The Flight Model of the Rayleigh Spectrometer showing the optically contacted construction. Photo courtesy Astrium Satellites SAS / Oerlikon Space.

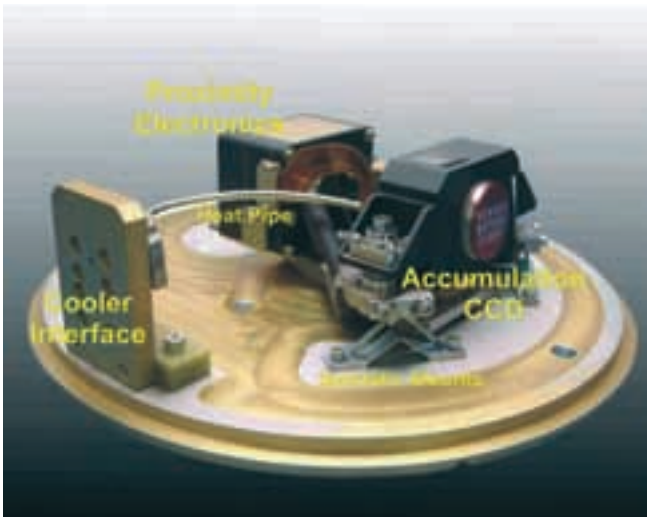

Fig. 4.28. Detection Front-end Unit with the Accumulation. Courtesy of Surrey Satellite Technology Ltd.

— high wavefront quality throughout the system,
— high optical transmission – over 75%,
— spectral filtering properties of 1 nm equivalent spectral width,
— high stray light rejection between transmitter and receiver path, and
— compact design, low mass but high stiffness.

Fig. 4.25 shows the Flight Model of the TRO. The transmitted light from the TXA is reflected by a high-reflectivity mirror, passes through the polariser, and is then directed towards the transmit-receive telescope via a beam expander. A small portion of the transmitted signal passes through the mirror and is directed via the reference path towards the receiver in order to allow measurements of the transmitter laser frequency.

The total mass of the TRO is only 2.6 kg.

4.3.5.3 Mie spectrometer

The output from the TRO is reflected in a polariser of the Rayleigh Spectrometer (RSP) towards the Mie Spectrometer (MSP) on the other side of the Optical Bench.

The Mie channel is based on a Fizeau interferometer made of two partially reflecting plates. A tilt is introduced between the plates to provide a linear spectral dispersion. In the Mie receiver, the received signal produces a linear fringe, whose position is determined by the wind velocity induced Doppler shift. Fig. 4.26 shows the Flight Model of the MSP.

The actual implementation of the MSP is visible in the ALADIN optical diagram (Fig. 4.13). the light is expanded to 36 mm input aperture in a small, afocal telescope. The actual Fizeau interferometer has a spacer of Zerodur to maintain the transmitted range with high stability. The spacing of the reflectors is 68.5 mm, giving a free spectral range of 2190 MHz. The output plate is tilted by 4.77 μrad, to give a useful spectral range of 1510 MHz. The effective spectral resolution of the Fizeau spectrometer is about 145 MHz. The interferometer is

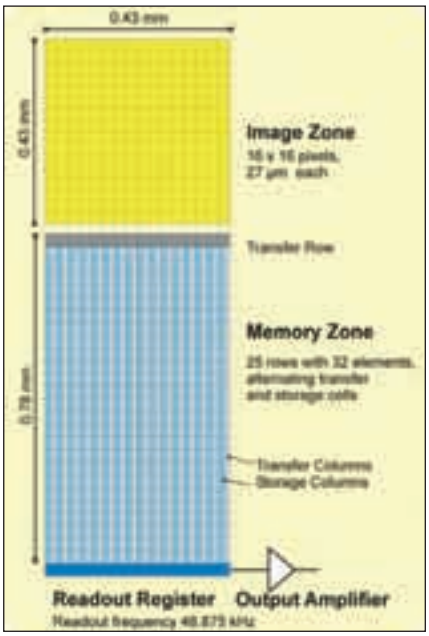

Fig. 4.29. Layout of the ACCD. The image zone comprises 16 x 16 pixels, and the memory zones have 25 lines.

Fig. 4.30. The Accumulation CCD in its package, which includes a thermo-electric cooler for operation at -30 °C. Picture courtesy of e2v.

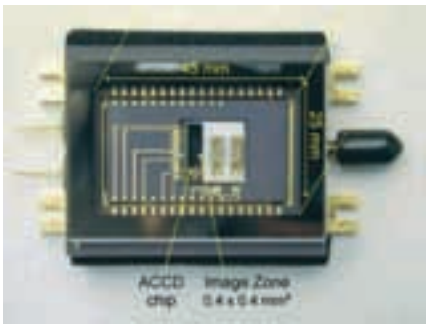

mounted in a vacuum cell to avoid spectral shifts from atmospheric pressure variations during the ground testing.

The output from the Fizeau spectrometer is a fringe. The position of this fringe on the ACCD detector indicates the Doppler shift of the received signal. A lens telescope is used to reduce the size of this output so that it fits onto the image area of the detector.

Most of the radiance onto the Fizeau interferometer is reflected back. The actual reflectivity is between 65 and 70%. This reflected light returns the same light path as the incoming light, and thus reaches again the Rayleigh spectrometer. However, it has passed twice through a quarter-wave plate in the beam path, and thus its polarisation has been rotated by 90º. It therefore now passes through the input polariser of the RSP.

4.3.5.4 Rayleigh spectrometer

The Rayleigh spectrometer is based on a double-edge Fabry-Pérot etalon. The ALADIN optical diagram (Fig. 4.13) shows the basic optical layout: the collimated light beam passes through the input polariser and enters the first etalon. Here, the spectral component of the light falling within the passband of the etalon is transmitted, while the residual component is reflected back. This part is now reflected on the polariser (it has passed twice through a quarter-wave plate), and now enters the second etalon, which has a different thickness and thus a different passband than the first etalon. The output from both etalons is focused and forms two spots on the ACCD detector.

The etalon optical parameters have been optimised to provide the same response for the broad Rayleigh backscatter as for narrow aerosol return: the spacing is 13.7 mm (10.9 GHz free spectral range), with a rather low finesse of 7, and a thickness step between the two etalons of 89 nm (spectral spacing of 5.5 GHz).

Both etalons are manufactured by optically contacting the end reflectors and the spacer, thus forming a very stable, nearly monolithic assembly. Fig. 4.27 shows the actual Flight Model of the RSP.

The crossover point of the spectral transmission from the two etalons must be tuned to be close to the centre of the Mie spectrometer useful spectral range. For this purpose, the RSP is mounted into a thermal enclosure that allows a controlled heating of the whole assembly over a 5 K wide range, which is sufficient to tune the etalons over one free-spectral range. The enclosure is designed to guarantee high thermal stability of the RSP temperature with minimal thermal gradients throughout the in-flight temperature range.

4.3.5.5 Detection front-end units with ACCD detectors

Two similar Detection Front-end Units (DFUs) are implemented for the Mie and the Rayleigh channels. Each one carries the ACCD and the timing electronics required to operate the ACCD. To limit the dark-current noise, the ACCD is cooled to -30º C with thermo-electric coolers. The excess heat from the coolers is transported via heat pipes to the DFU radiators. Fig. 4.28 shows the DFU.

The ACCD is a thinned backside illuminated Si-CCD which is optimised for high quantum efficiency – over 75% at 355 nm (over 83% have been measured for the flight models). It has a small image zone of 16 by 16 pixels, which can be read out within 1 µs. The charges from the image zone are binned in one line and stored in up to 25 rows in a memory zone, each row representing an atmospheric height bin. Fig. 4.29 shows the layout of the ACCD, and Fig. 4.30 shows the actual packaged device.

The signals are accumulated on the CCD chip. For the readout of small charges, the noise from the readout amplifier becomes the dominant noise source

and limits the sensitivity of the detection. However, with the on-chip accumulation (over several laser shots), the charges become sufficiently large that the noise contribution of the preamplifier becomes negligible compared to the shot noise from the detected signal itself. Thus the shot-noise detection limit is approached, which is the ultimate sensitivity limit.

Fig. 4.31 explains the operation of the ACCD for the two channels. The linear fringe (for the Mie-receiver) or the two image spots (for the Rayleigh receiver) are imaged in the image zone. After integration over a time corresponding to the vertical resolution of the altitude bin, the lines of the image zone are added together in the transfer row of the memory zone and clocked one line down in the transfer columns. After repetition of this procedure for each time (or vertical) bin of one echo, the fringe or spot profiles are contained in the transfer columns. Each line corresponds to one temporal (or vertical) bin. The fringe or spot profiles are then shifted horizontally by one element into the storage columns. During the next lidar return, the bins of the stored profile are sequentially transferred, via the transfer columns into the storage columns. Repetition of this sequence allows the co-adding ('accumulation') of fringe or spot profiles from successive laser shots. The image and transfer columns are cleared to eliminate stray charges each time their content has been fully transferred to the next zone.

At the end of the accumulation sequence (15 or 50 shots), the fringe or spot profiles are finally read out via the readout register. This operation mode, in which the charges are always moved in the same direction through the CCD, has been chosen to avoid pollution of the fringe or spot profiles by charges left behind by the potentially larger ground echo.

At laser emission, a part of the beam is injected into the receivers. The image zone is immediately read out before the rest of the beam is scattered back from the atmosphere. This allows the laser frequency jitter to be monitored on a pulse-to-pulse basis.

The Detection Electronics Unit (DEU) digitises the data from the two ACCD detectors and formats them into data strings. It also adds ALADIN telemetry data from the ALADIN Control & Data Management-unit (ACDM) and sends these data strings to the Aeolus platform for storage and down linking.

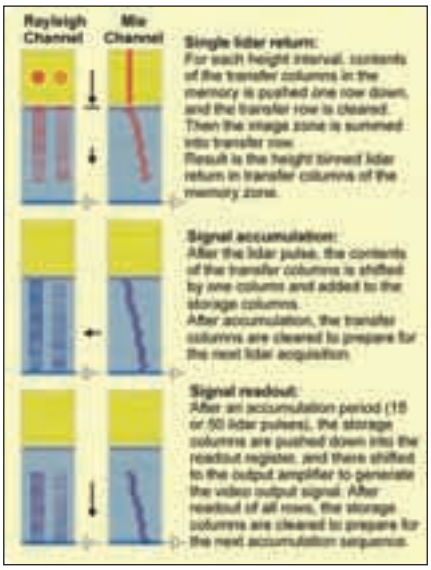

Fig. 4.31. Operation principle of the Accumulation CCD during nominal measurements. The outgoing laser pulse is read out directly without accumulation between the received lidar returns.

4.3.6 ALADIN operations

The burst-mode operation and the on-chip signal accumulation make the timing and the operation of ALADIN rather complex. All operations are organised in the burst cycle of 28 s, here called the Basic Repeat Cycle (BRC). Fig. 4.32 shows the data from several BRCs on a map to indicate the actual relations.

A BRC starts with the warm up of the laser (5 s), then the observation (7 s) with the laser operating nominally, and 16 s of no laser operation. The accumulated data are then transferred from the DEU to the spacecraft Command and Data Management Unit (CDMU), to load new parameters for the detection chain and the transmitter laser. Data taken during the last three seconds of the warm-up phase are also stored and downlinked. Thus, data from a total of about 1000 laser pulses are available for the derivation of the wind profiles.

The observation period consists of N accumulations of P shots, where $N*P \leq 1005$. P can be selected as 15 (0.15 s or about 1 km) or 50 (0.5 s or 3.6 km), where the latter corresponds to the nominal setup. The Mie and Rayleigh channels have the same number of N measurements and P shots. The two settings are expected to give sufficient flexibility in order to determine the best compromise between spatial resolution of the downlinked data and noise reduction by increasing the accumulated charges.

During each shot, the laser reference line is sent to the ACCD detector via the calibration path. The reference signal is immediately read out from the ACCD

Fig. 4.32. Aeolus wind observations and their subdivision into measurements. Each measurement corresponds to the on-board signal accumulation in the CCDs, which are co-added on-ground for each observation. In the mode shown in the figure, 50 laser shots are accumulated, corresponding to 3.5 km ground distance. In a second mode, only 15 shots (1 km) can be integrated for higher spatial resolution, but at the cost of higher signal noise.

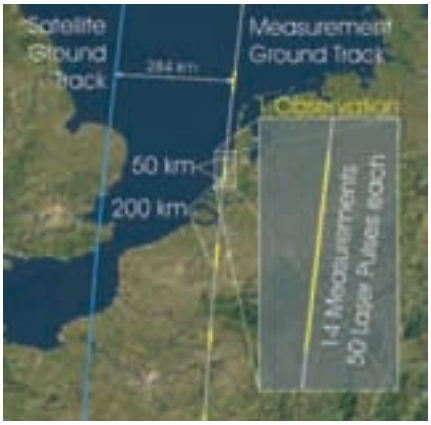

Fig. 4.33. The Aeolus satellite in-flight configuration.

and is not accumulated because the laser reference is measured at (relatively) high photon flux for a better accuracy, and because on-chip accumulation could lead to CCD saturation. Moreover, this allows for shot-by-shot monitoring of the emitted laser frequency, and potentially the elimination of measurements with aberrant frequency during the on-ground processing.

The atmospheric signals arrive at the ACCDs about 3 ms after emission. The sampling of the ACCD determines the vertical sampling of the atmosphere. The sampling profile can be updated via telecommands. A new profile can only be started at the beginning of a BRC. Each altitude sample can be set in the range from 2.1 μs (corresponding to 250 m altitude resolution) to 16.8 μs (corresponding to 2 km) in steps of 2.1 μs. A total of 24 steps can be commanded. The 25th sample is used for the background measurement. The Mie and Rayleigh channels are sampled independently so different altitude resolutions can be selected for the aerosol and molecular scattering. The Mie channel sampling can, for example, be set to start later than the Rayleigh channel sampling.

The selected accumulation sequence is repeated over *P*-2 shots. During the last two shots, the accumulated data are read out. At the end of the accumulation, the following data have been acquired:

— *P*-2 'reference data' for the Mie channel and *P*-2 'reference data' for the Rayleigh channel,
— 24 atmospheric samples for the Mie channel and 24 atmospheric samples for the Rayleigh channel, and
— 1 background measurement for each of the Mie and Rayleigh channels.

The design allows for the programming of:

— the horizontal sampling parameters (*N, P*) over an orbit,
— the vertical sampling profile (24 consecutive integration times and a background integration time), and
— the delay between the Rayleigh channel start and the Mie channel start. This set of parameters can be modified between two consecutive basic repeat cycles.

Fig. 4.34. X-ray view of the Aeolus satellite, indicating the key satellite subsystems.

The delay between the emission and acquisition of the laser return is dependent on the satellite altitude. Because the altitude changes during an observation, a correction of the time delay is necessary. Thus the vertical sampling starting time is real-time adjusted by using the data provided by the satellite between two accumulation periods.

4.4 Aeolus platform design

4.4.1 Platform description

Fig. 4.33 shows the Aeolus satellite. It points 35º into the eclipse side of the orbit in order to control the line-of-sight of ALADIN. Due to the dusk-dawn orbit, the solar arrays are fixed at about 45º with respect to the satellite body throughout the flight; only one rotation is required during deployment.

The total satellite dry mass at launch is about 1100 kg, plus up to 226 kg of fuel. Its size is 4.3 m x 1.9 m x 2.0 m in launch configuration, limited by the payload envelope. The solar arrays of 13 m span have three panels on each side. The launch can be performed by any of the small launchers, such as Vega, Rockot or Dnepr, to be selected at a later stage in the development program.

The satellite layout is shown in Fig. 4.34. The actual Aeolus satellite structure model is seen in Fig. 4.35. Its structure, consisting of aluminium honeycomb elements, uses a conventional box-shaped spacecraft design (derived from Mars Express), upon which the observation instrument is mounted via four quasi-isostatic blades. The electronic boxes of the bus and the associated satellite equipment are mounted on the side panels.

The electric power is provided by two fixed 13.4 m^2 solar arrays. The gallium-arsenide cells of the solar arrays provide over 2.4 kW of power (1.4 kW average

Fig. 4.35. Aeolus Satellite Structure Model during test preparation.

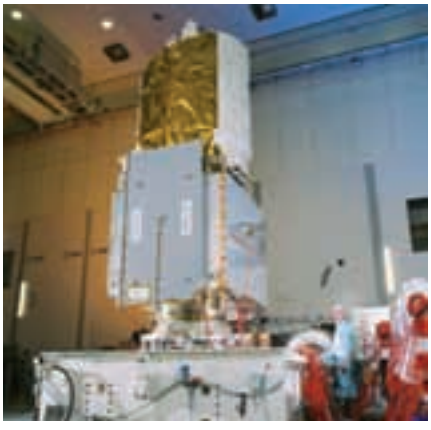

Table 4.4. Aeolus AOCS components

Type	*Equipment*	*Nr.*	*Main characteristics*	*Technology*	*Redundancy*	*Use*
Sensors	Magnetometer	2	Three-axis	Anisotropic magneto-resistor	Cold redundancy	Initial and safe mode
	Coarse Earth sun sensor	4	4 π sterad FOV	Thermal	Internal (2 of 3)	Initial, Nominal and safe mode
	GPS receiver	2	C/A GPS receiver	RF ASIC and micro processor	Cold redundancy	Nominal mode
	Autonomous star tracker	2	Large FOV	CCD	Cold redundancy	Nominal mode
	Rate Measurement Unit	1	3 measurement axes	QRS-11 Sensors	None	Safe mode
	Inertial Measurement Unit	1	3 measurement axes	Fibre Optic Gyro	Internal (3 of 4)	Initial and Nominal mode
Actuators	Reaction wheels	4	40 Nms/0.2 Nm	Ball bearings	3 of 4	Nominal mode
	Magnetic torquers	3	400 Am^2	Windings	Cold redundancy	Initial, Nominal and safe mode
	Thrusters	5	5 N	Hydrazine	Cold redundancy	Initial, Orbit control and safe mode

(FOV = field-of-view, GPS = global positioning system.)

power is required). A Lithium-ion battery of 84 Ah is used during the eclipse phases.

An ERC-32 radiation tolerant processor with 6 MByte of RAM performs on-board data handling. The subsystems are linked via a MIL-STD-1533 data bus to the central processor. A solid-state memory provides a capacity of 8 GByte of onboard data storage.

The telemetry and telecommand communications are based on standard S-band links, with an up-link data rate of 2 kbit/s and a downlink data rate of up to 8 kbit/s. The measurement data are dumped via an X-band transmitter with a data rate of about 5 Mbit/s. The spacecraft operations will be performed at ESOC (Darmstadt, Germany) using the Kiruna S-band station for uplink of telecommands and reception of telemetry. Nominally, the measurement data will be received by the ground station in Svalbard (Norway). Additional X-band receiving stations (with antenna diameters as small as 2.4 m) can easily be added to provide a shorter data delivery time.

Aeolus was designed to allow for simple inflight operation, and a five-day autonomy in case of any single onboard failure. A single operator shift is sufficient to monitor the satellite. In addition, the orbit has a seven-day repeat cycle, so that the complete operations timeline is repeated on a weekly cycle, thus minimising the effort for mission planning.

Fig. 4.36. Pointing geometry of Aeolus, indicating yaw, pitch and roll angles.

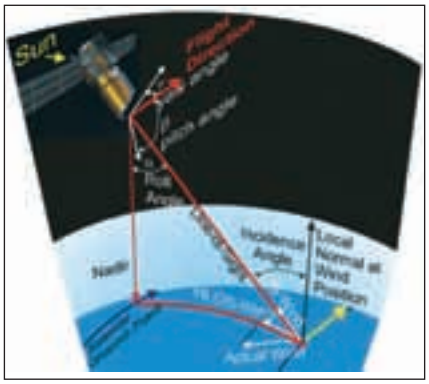

4.4.2 Attitude and orbit control system

For the overall wind profiling performance, the pointing stability plays an important role. The line-of-sight of ALADIN needs to point at a known angle with respect to the ground track velocity vector of Aeolus.

Fig. 4.36 shows the Aeolus pointing geometry and defines the relevant symbols for roll, pitch and yaw angles. The Attitude and Orbit Control System (AOCS) steers the attitude of Aeolus to keep the ALADIN line-of-sight orthogonal to the LOS ground intercept velocity vector. Through the orbit, it is turned around the yaw-axis to compensate for changes in the Earth rotation relative to the flight direction, as well as the velocity changes from the systematic orbit height variations with respect to the Earth ellipsoid ('yaw steering'). Thus, ideally, all contributions from the spacecraft orientation and motion to the observed Doppler shift vanish. In practice, the AOCS pointing is not ideal. Pointing errors around yaw, pitch or roll lead to a projection of the spacecraft velocity vector onto the ALADIN line-of-sight and, therefore, the measured wind velocity offsets. The

Table 4.5. Aeolus LOS pointing performance predictions and specifications for the various error types.

Error Type	*Budget [µrad]*	*Specification [µrad]*
Absolute Pointing, Nominal Measurement	301	350
Absolute Pointing, Calibration Measurement	299	350
Pointing Stability over 100 orbits	36	40
Pointing Stability over 28 minutes (Calibration Measurement)	27	30
Pointing Stability over 10 seconds	9	10
Absolute Measurement Error	32	46

most sensitive axis is the pitch axis ('up-down motion'), followed by the yaw axis ('left-right motion'), while roll motion causes only very small velocity offsets. For the pitch axis, a depointing angle $\delta\beta$ (in rad) causes a velocity-offset δv (in m/s) of

$$\delta v = 6280 \cdot \delta\beta \tag{4.2}$$

Thus a pointing error of 100 µrad causes a velocity offset of less than 0.63 m s^{-1}. However, the required unknown bias error is below 0.4 m s^{-1}, which means that a better pointing knowledge is required. This knowledge improvement is achieved through LOS ground return measurements.

The Aeolus AOCS is designed to meet the demanding pointing requirements (see Table 4.4). It uses a GPS receiver to determine its orbit position with an accuracy of better than 10 m, an Autonomous Star Tracker (AST) with a measurement accuracy of 13 µrad, and an Inertial Measurement Unit (a high-resolution fibre-optic gyro) for rate measurements between the AST readings.

The pointing is controlled by a set of four momentum wheels and magnetorquers for the offloading of the reaction wheels. For orbit maintenance, a set of four 5 N thrusters are used. In Safe-mode and after launch, a second set of sensors and actuators is available: the Coarse Earth-Sun Sensor determines the directions to the sun and Earth, the Rate Measurement Unit measures the satellite rotation rate, and the magnetometer obtains the local magnetic field. The attitude control is done with the help of the thrusters, and with the magnetorquers operated in parallel to reduce fuel consumption.

The performance specifications, together with the actual LOS pointing performance budget as analysed, are summarised in Table 4.5. However, to meet measurement accuracy requirements, the absolute pointing errors have to be reduced. This is done using the laser ground return, which is present in many lidar signal returns. This ground return must have a zero wind velocity. However, to meet the stringent zero-wind bias requirement of 0.4 m s^{-1}, ground returns from many orbits need to be processed to determine bias and orbital harmonics with sufficient precision.

4.5 Calibration and characterisation

4.5.1 General remarks

Calibration is the procedure for converting the instrument measurement output data into the required physical quantities. In the case of Aeolus, this is mainly the wind speed calibration, and altitude assignment calibration.

Characterisation is the determination of a set of technical and functional parameters, valid over a range of conditions, to provide data necessary for calibration, ground processor initialisation and verification. An example for characterisation data are the determination of optical transmission of the Rayleigh

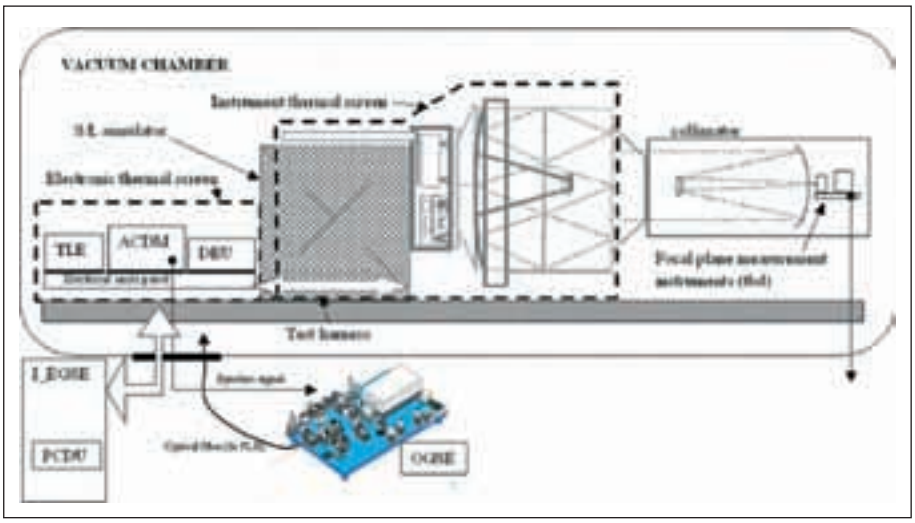

Fig. 4.37. Drawing of the test set up for ALADIN characterisation testing in the thermal vacuum chamber, with the used Optical Ground Support Equipment (OGSE) indicated.

spectrometer as function of wavelength for a range of temperatures, or the behaviour of the transmitter laser as a function of the cold plate temperatures.

To meet the demanding performance specifications for Aeolus, in particular for the bias requirements, a careful characterisation of the ALADIN behaviour is required on ground and during the early flight phases. Several calibration functions must also be regularly performed in flight.

4.5.2 On-ground characterisation of ALADIN

The ALADIN assemblies and subsystem will be fully characterised on-ground. Thus, in principle, all individual parameters affecting the overall measurement performance will be known before ALADIN undergoes integration.

After completion, ALADIN will undergo an extensive test campaign to characterise all functional and performance relevant parameters under controlled conditions on ground. Most of the measurements will be performed in a vacuum chamber with thermal shrouds surrounding the instrument, in order to simulate closely the anticipated in-flight conditions.

Fig. 4.37 shows ALADIN in the thermal vacuum chamber, with the Optical Ground Support Equipment (OGSE) required for the characterisation.

The dedicated ALADIN signal simulator OGSE is a laser system that can generate optical signals with spectral and radiometric properties identical to the backscattered signal expected in flight. It is a continuous-wave Nd:YAG laser that is frequency tripled. The output is frequency shifted in a set of four acousto-optic modulators, and the intensity is controlled with an electro-optic modulator. The simulated backscatter signal is fed into an optical fibre. This signal OGSE is shown in Fig. 4.38.

Fig. 4.38. ALADIN signal simulator OGSE set-up, showing the continuous wave Nd:YAG laser with a tripling stage, a set of four acousto-optical modulators for frequency tuning and an electro-optical modulator for intensity modulation of the UV beam. The signal is coupled into an optical fibre to guide it into the ALADIN test chamber.

The simulated backscatter signal is fed either directly into the ALADIN receiver, or into a collimator assembly to generate a large diameter test beam (0.6 m diameter) with known wave front properties. The beam is then fed into the ALADIN transmit-receive telescope via a fibre optical cable.

For practical reasons, the diameter of the collimated test beam is less than the ALADIN telescope diameter, preventing a full end-to-end testing. An analysis of the residual risk has shown that the investment in a larger collimation telescope is not justified by the more complete characterisation.

The characterisation data from the ground test campaigns will be stored in a database for use in the on-ground processing of the measurement data.

4.5.3 In-flight calibration functions

In flight, Aeolus performs several characterisation and calibration measurements. The receiver spectral properties must be known to a very high accuracy in order to meet the zero-wind bias and slope error requirements. This is done with three procedures:

— **Instrument Auto Test (IAT):** the transmitter laser is tuned through a ±5 GHz wide range in 250 MHz steps away from the centre, and 25 MHz steps within the inner ±750 MHz. This measurement allows the spectral properties of the Mie- and Rayleigh spectrometers to be characterised.
— **Mie Response Calibration (MRC)**, and
— **Rayleigh Response Calibration (RRC):** the latter two measurements are performed by rolling Aeolus by 35º so that ALADIN is pointing near Nadir (see Fig. 4.39); in fact, Aeolus is pointing about 2 mrad off-Nadir to avoid specular reflections. In this geometry, the Doppler shift is not dependent on the horizontal wind speed, and should be measured as zero for an ideally pointing spacecraft. Small depointing angles can be used to introduce a known Doppler shift and thus to verify the accuracy of the wind speed measurements. Alternatively, the laser frequency can be tuned in steps to probe the receiver response at various frequency offsets. The procedures for the Mie and Rayleigh receivers use the same principles, but contain different frequency steps and measurement durations.

Another set of on-ground and in-orbit characterisation measurements are required to update various parameters for the proper functions of ALADIN. These are:

— **Instrument Spectral Registration (ISR):** the transmitter laser is tuned across its full ±5.5 GHz wide spectral range in 25 MHz steps. On ground, the frequency setting matching the centre frequency of the Mie Spectrometer is determined and commanded to the transmitter laser for wind observations. The temperature of the Rayleigh spectrometer enclosure is tuned to bring the crossover point of the two etalons to this frequency. This characterisation has to be performed after launch.
— **Dark Current Calibration (DCC):** the dark current of the ACCD detectors must be known to a high accuracy in order to allow for a correct subtraction during the ground processing. The dark current can be measured in flight by commanding the laser chopper mechanism to stay closed during observations. About 50 observations with the chopper closed are performed to achieve the required accuracy. This characterisation is performed infrequently during flight.
— **Instrument Defocus Characterisation (IDC):** the collimation of the transmit-receive telescope can be controlled with heaters in the telescope struts and behind the primary mirror. The quality of the collimation can be observed in flight with the Rayleigh ACCD detector: For this characterisation, the ACCD is operated in the image mode (the complete return signal is integrated and then the image is read out), and the spot size of the two-etalon outputs is determined. If the size exceeds a given limit, the temperature of the telescope is adjusted to minimise the spot sizes again. This measurement takes 10 observations and should be repeated weekly.
— **Transmitter laser characterisations and settings**, like laser diode temperature check, settings of the master oscillator frequency locking loop, etc.

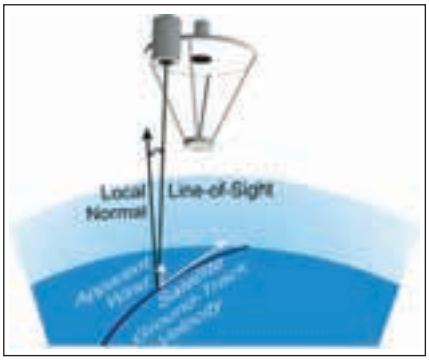

Fig. 4.39. Aeolus in end-to-end calibration mode. Due to the pointing near nadir, the Doppler shift of the received signal is not dependent on (horizontal) wind velocity, but only on the projected satellite velocity and is thus deterministic. The laser emitter and receiver are both located inside the telescope, but are for practical reasons drawn next to each other here.

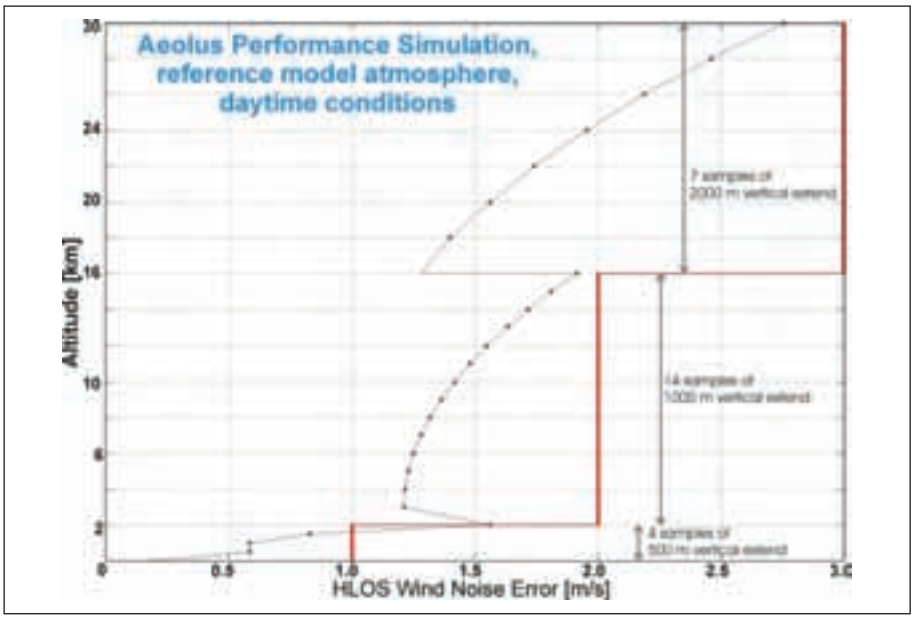

Figure 4.40: Aeolus HLOS wind error from the surface up to 30 km for a 'normal' atmosphere without clouds.

4.6 Performance budget

Although the Signal-to-Noise Ratio (SNR) of the receiver measurement is the main contributor to the error budget, various other sources of errors originate from the instrument design itself or from the processing and calibration operations. When no ground echo is available the attitude and velocity restitution errors must also be added.

The main contributors to the overall system error include:

— the *random error* related to the effect of the detection noise statistics as calculated by the wind retrieval algorithm. This is by far the biggest contributor to the overall error budget,
— the Rayleigh signal contamination of the return signal entering the Mie channel,
— the *Mie signal contamination* of the return signal entering the Rayleigh channel,
— *ground echo accuracy* relates to the calibration of the 'zero wind' using the Mie channel and the ground return,
— *internal calibration accuracy* refers to the 'zero' inter-channel calibration error using a laser pulse emitted internally and measured by both channels,
— *response calibration accuracy* refers to the error on the spectral calibration using an internal laser pulse swept in frequency over the useful spectral range of both channels, and
— the *Sensor/LOS alignment stability* refers to the determination of LOS Earth and satellite Doppler shifts extrapolated from onboard sensor data and used when the ground echo is not available. The main contribution comes from the thermo-elastic behaviour of the instrument structure as well as attitude restitution stability, over half an orbit in the worst case.

Fig. 4.40 shows the calculated accuracy of the horizontal wind component (HLOS) for a 'normal' atmosphere. The calculation includes the random error

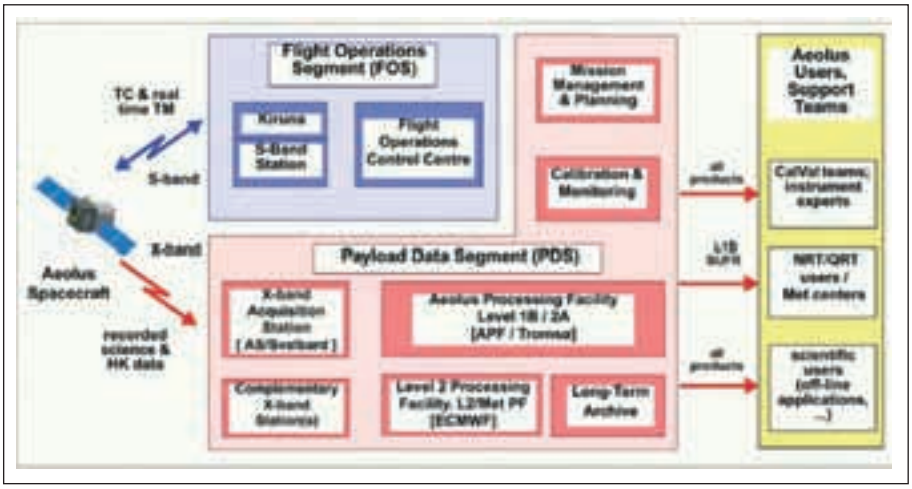

Fig. 4.41. Overall Aeolus ground segment.

for each channel at the indicated altitude range. Systematic bias errors (correlated errors between profiles) are also considered.

For the Mie channel, the LOS wind error is below the required 1 m s^{-1} from 0 to 2 km height. The reliability is around 100% in the same altitude region. For the Rayleigh channel, the LOS wind error is below the requirement.

With altitude sampling intervals increased to 2 km above 16 km altitude, the wind error stays below 3 m s^{-1} for altitudes up to 30 km. Thus Aeolus can measure meaningful wind profiles even in the stratosphere, which could be of great interest for future weather prediction models.

4.7 Aeolus ground segment

4.7.1 Overview

The Aeolus Ground Segment will control and perform the commanding and monitoring of the spacecraft as well as the acquisition, processing and dissemination of science data. It comprises the two main components, the Flight Operations Segment (FOS) in ESOC (Darmstadt, Germany) and the Payload Data Segment (PDS) in ESRIN (Frascati, Italy). Fig. 4.41 shows the overall structure of the Aeolus ground segment and the interfaces between the different units.

4.7.2 Ground station network

Ground stations are required for two different functions (see Fig. 4.42):

— telecommand uplink to Aeolus, and reception of real-time telemetry during station passes for health monitoring, performed in S-band with low data rate (2 kbit/s uplink at 2030 MHz, and 8 kbit/s downlink at 2205 MHz), and
— reception of the measurement data strings as well as the stored housekeeping data for health monitoring in the X-band (8040 MHz), a downlink with 5 Mbit/s effective data rate.

The ground station for the telecommand link is located in Kiruna (Sweden). There are up to 5 blind orbits per day. Because of the good infrastructure, including the ground data links to the command & control centre in ESOC (Darmstadt, Germany), this station is the best choice.

Due to the near real-time requirement (a part of the data product should be available within less than 3 hours after measurement), the measurement data must

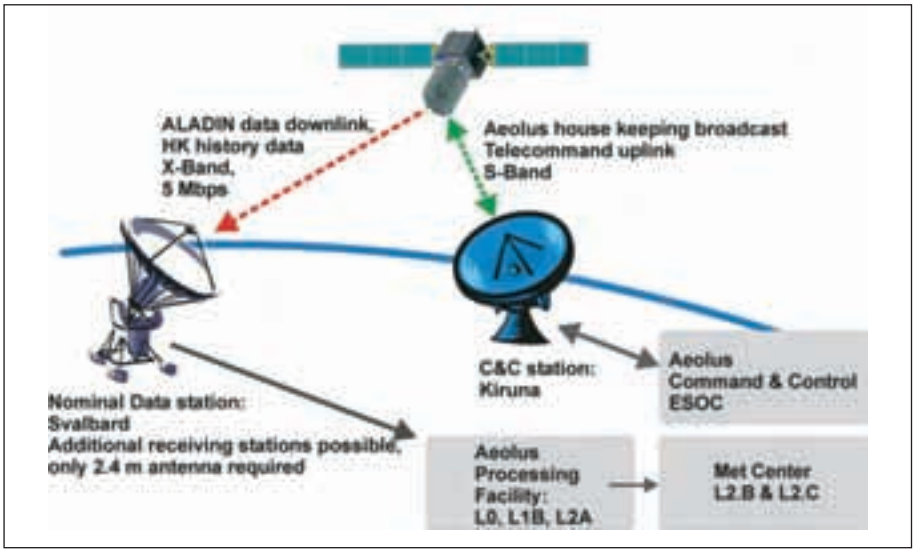

Fig. 4.42. Conceptual view of the Aeolus ground station network with command control link, and measurement data reception link.

be down linked to a ground station every orbit. For the selected orbit (400 km altitude) the satellite has a much smaller ground station visibility than the 'typical' 800-km-orbits (for example, the ERS and ENVISAT satellite orbits). However, the Svalbard ground station (see Fig. 4.43) is located far in the North, and Aeolus can be seen from the station every orbit. However, because some station passes are at very low elevation, it cannot be guaranteed that the measurement data from these orbits can be successfully downlinked. During commissioning phase, the feasibility to use this low elevation pass will be verified. All other Aeolus orbits have better station coverage.

For NWP, it is highly desirable that (a part of) the data is delivered within 30 minutes after sensing ('quasi-real-time'). Aeolus has the capability to send measurement data to other 'fill-in' ground stations to allow for quasi-real-time data delivery. However, these 'fill-in' receiving stations are not part of the ESA supported ground-station network.

4.7.3 Flight operations segment

The Flight Operations Segment (FOS) comprises two main elements:

— the Tracking, Telemetry and Command station (TTC) located in located in Kiruna/Sweden, and
— the Flight Operations Control Centre (FOCC), located at ESOC in Darmstadt/Germany.

The FOCC will perform all tasks related to the spacecraft health monitoring, the acquisition of housekeeping telemetry, and the flight dynamics analysis. It will further generate all telecommands necessary to operate the spacecraft throughout the different phases of the mission.

4.7.4 Payload data segment

The main elements of the Payload Data Segment (PDS) are:

— the X-band Acquisition Station, located in Svalbard (Norway),
— the Aeolus Processing Facility (APF), located in Tromsoe (Norway),

Fig. 4.43. The Svalbard satellite reception station in Norway. Photo courtesy Kongsberg Satellite Services, Norway

— the Level 2 Processing Facility (L2/PF), located at the European Centre for Medium-range Weather Forecast (ECMWF) in Reading (UK),
— the Archiving Facility & Inventory (ARF/INV),
— the Aeolus Calibration & Monitoring Facility (ACMF),
— the Mission Management & Planning Facility (MMPF),
— the User Service & Dissemination Facility (USDF), and
— the Long Term Archive (LTA).

The ADM-Aeolus Processing Facility will be a central element of the PDS, performing all processing tasks up to Level 1B and generating the so-called supplementary Level 2 data product (Level 2A).

The Level-2 Processing Facility will be hosted by the European Centre for Medium Range Weather Forecasts (ECMWF) that will receive all of the Level 1B data in near-real-time, for the purpose of producing consolidated Aeolus wind observations (Level 2B) and assimilating Aeolus observations in the operational weather prediction system. An additional product generated by the L2/PF will be the so-called Aeolus assisted wind product (Level 2C) that results from the assimilation of Aeolus observations combined with the other data from the Global Observation System.

The Archiving Facility & Inventory will store all data products, including the Level 2B/2C products generated by the L2/PF, throughout the mission lifetime.

The ADM-Aeolus Calibration and Monitoring Facility will be in charge of specific processing tasks, primarily for the routine in-flight calibration activities, and the performance-critical monitoring.

The Mission Management and Planning Facility will execute all essential planning tasks and send timeline and command table data to the Flight Operation Segment at regular intervals.

The User Service and Dissemination Facility will provide external users with the access to inventory information, accept orders for already generated data products, and deliver requested products to the end users.

Finally, the Long-Term Archive will store all Aeolus products for a minimum duration of ten years after the end of the mission.

5. Data products and scientific data processing

The ADM-Aeolus products contain unique atmospheric information of interest for meteorological research on dynamics, cloud and aerosol distributions, and transport phenomena (see Chapter 2). All products will be generated, distributed, and archived for the duration of the ADM-Aeolus mission. The next section provides an overview of the ADM-Aeolus processing and the output products. The subsequent sections provide more detailed descriptions of the processing steps, the measurement quality control and verification, and the improvements of the meteorological analysis fields.

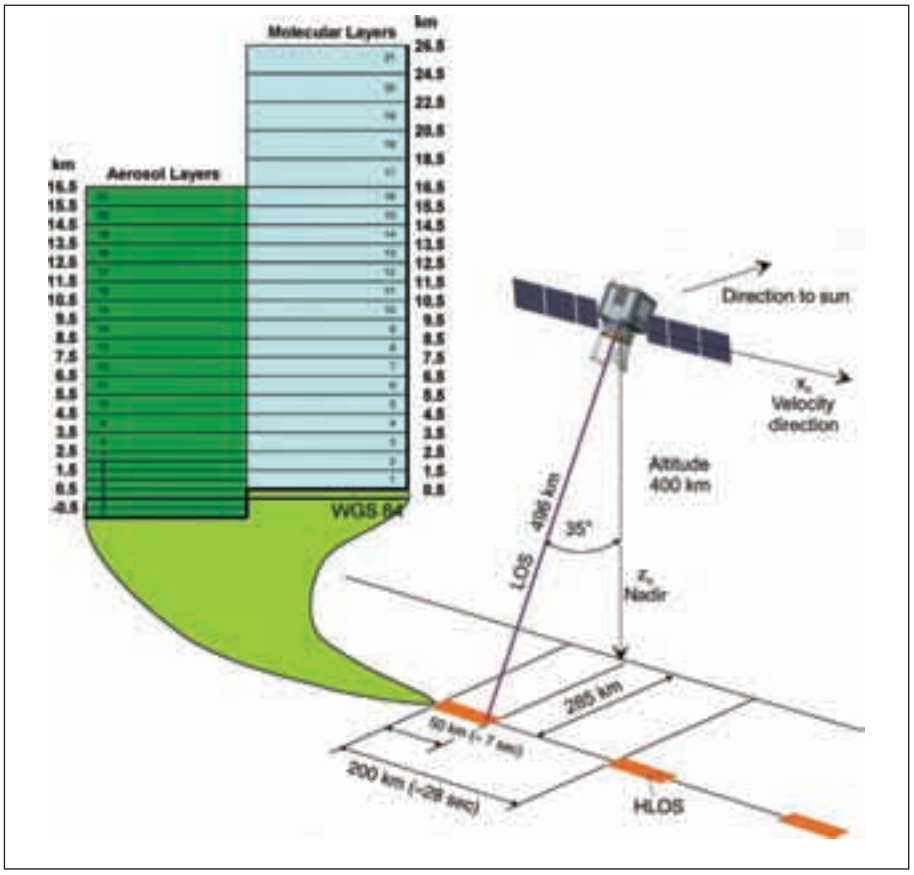

Fig. 5.1. ADM-Aeolus measurement geometry

5.1 ADM-Aeolus processing and products overview

5.1.1 From raw data to mission parameter

The instrument transmits raw data to the ground segment consisting of the accumulated spectra from the Mie receiver and the flux intensities from the Rayleigh receiver. In the baseline mode, these data are provided every 3.5 km (with the possibility to increase the resolution to 1 km), and for each altitude bin (-1 km to 16.5 km height for the Mie channel, 0.5 km to 26.5 km for the Rayleigh channel). However, the vertical sampling grid can be reprogrammed from the ground and will be optimised during flight. In addition to these data, laser internal calibration, attitude information, and receiver response calibration data are transmitted as well. The horizontal and vertical sampling is shown in Fig. 5.1.

Prior to integrating data over the observational 50 km length (see Section 4.2.4), cloud detection is performed in order to segregate the measurement in

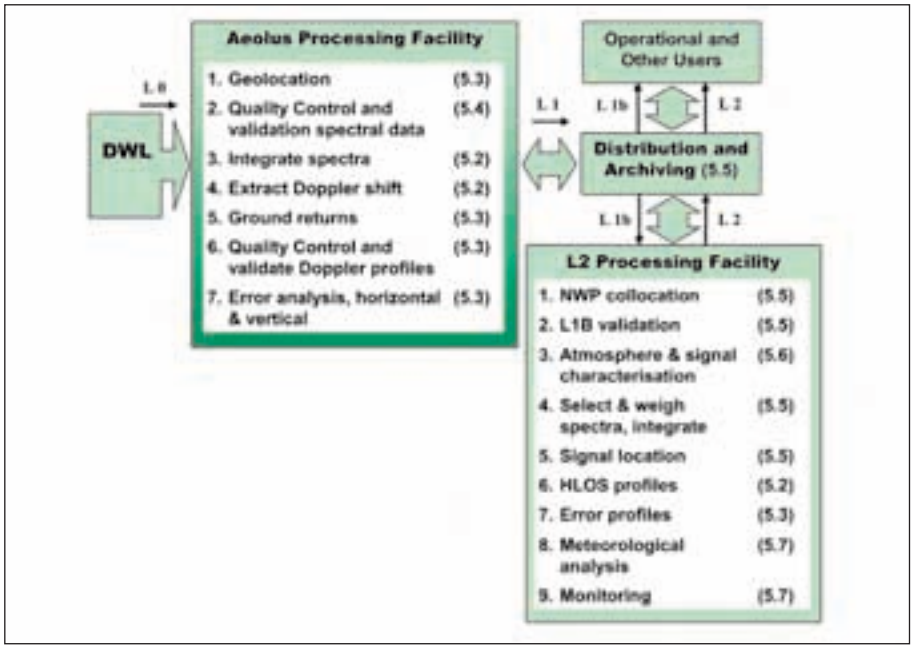

Fig. 5.2. Schematic flow diagram for the data processing, validation and calibration of the information from a spaceborne DWL.

clear air and those affected by cloud to control the processing in the presence of scattered cloud (see Section 5.4). If a LOS measurement is affected by clouds, the wind profile above the cloud, and perhaps beside it, is still obtained. A ground echo is also searched for, in order to calibrate the 'zero wind' when possible (used for subtracting the Doppler shift variation due to the movement of the satellite). If no useful ground echo is measured (e.g. when the surface is obscured by clouds), satellite sensor data will be used to derive the satellite attitude Doppler shift variations.

In order to transform raw data into wind measurements, the Mie and Rayleigh channel measurements must be further processed. The radiance background and the spectrometer spectral response, as well as calibration data, are then taken into account. The decision to use Mie or Rayleigh channel data (or both) is based on a signal-to-noise ratio threshold, associated with a wind error variance threshold. Finally, each wind measurement for each altitude layer is located in an Earth reference frame, using satellite sensor data.

A schematic flow diagram for the data processing, calibration and validation, and information dissemination for the spaceborne Doppler wind lidar is shown in Fig. 5.2. The various elements are discussed in the following subchapters, as indicated by the numbers shown to the right of each item. The particular tasks of the ADM-Aeolus Processing Facility (APF) are shown in Fig. 5.3, explaining the various processing steps.

The Earth Explorer ADM-Aeolus is a demonstration mission in several respects. Although the ground processing is not very complex, there are several aspects of the processing that will be developed during the demonstration mission by the lidar and scientific community. The most important of these are discussed in this chapter.

5.1.2 ADM-Aeolus data products

Table 5.1 summarises data products to be systematically generated within the ADM-Aeolus Payload Data Segment, including the Level 2 Processing Facility (Level 2/PF).

Table 5.1. ADM-Aeolus product levels

Product / Data Set	*Contents*	*Remarks*
Level 0	Raw data (cleaned and time-ordered): - raw instrument and house-keeping (HK) data, - platform housekeeping data - attitude and orbit control system (AOCS) data - quality control parameters	The sensing period will typically cover 1 orbit, depending on the downlink scenario
Level 1A	Geolocated, un-processed observational data: - processed geolocation and AOCS data - reconstructed instrument measurement data - fully processed housekeeping data	Stored in the PDS, but not distributed beyond the L1B processor
Level 1B	Geo-located, fully calibrated observational data: - geolocation and AOCS data - product confidence data - signal strength of Mie- and Rayleigh profiles - processed ground echo data - instrument corrected HLOS winds - processed calibration, quality control, and housekeeping data (as in Level 1A)	Preliminary HLOS winds based on standard atmospheric corrections
Level 2A	Supplementary products: - geolocation and AOCS data - product confidence data - cloud and aerosol information (cloud classification, backscatter, optical depth, backscatter-to-extinction ratio, …)	
Level 2B	Wind products: - geolocation and AOCS data - product confidence data - Mie HLOS wind profiles - Rayleigh HLOS wind profiles	
Level 2C	Assimilated wind products: - geolocation & AOCS data - product confidence data (as in Level 2B) - Mie wind profiles (as in Level 2B) - Rayleigh Wind Profiles (as in Level 2B) - Assimilation product confidence data - Mie vector-wind profiles - Rayleigh vector-wind profiles	The Level 2C data file is a superset of the Level 2B data file

Level 0
These are raw instrument data, cleaned and time-ordered. Level 0 contains source data packets with instrument and housekeeping data, and Attitude and Orbit Control System (AOCS) parameters. No processing has been performed but quality parameters are annotated.

Level 1A
Level 1A is an intermediate data product that contains geolocated, unprocessed observational data, which have been reconstructed and contain processed housekeeping information:

— Housekeeping parameters are fully processed and converted into physical units;
— Navigation/AOCS data are processed and collocated with ALADIN measurements via time stamps
— ALADIN measurements are reconstructed, but no processing of the observational data has taken place

— The annotation data consist of instrument health parameters and product confidence data

Level 1B
Level 1B is geolocated, fully calibrated observational data consisting of processed and calibrated ADM-Aeolus atmospheric scene and calibration data:

— The housekeeping data is, as in L1A, time-correlated with processed spectrometer data
— Radiometric corrections have been applied to the observational data
— Separate reporting of Mie & Rayleigh profiles, error information included
— Navigation /pointing data collocated with ALADIN measurements
— Annotation data:
  - Fully processed geolocation information
  - Product confidence data
  - Error information and quality indicators, useful for Level 2 processing
  - Spectral calibration parameters of individual ground returns and
  - corresponding statistical quantities (Root-Mean-Square (RMS) error, slope, …)

Level 2A
Level 2A contains the ADM-Aeolus supplementary geophysical products. These include:

— Presence of clouds or aerosols in each vertical range bin
— Optical depths
— Scattering ratio
— Backscatter-to-extinction ratios

Level 2B
Level 2B contains ADM-Aeolus consolidated HLOS wind observations. These are:

— Consolidated HLOS wind profiles using external atmospheric state parameters (Temperature, pressure, …)
— Profile quality information needed as input to wind assimilation processing (statistically derived using product confidence data and external geophysical information)
— Atmospheric variabilities, gradients etc. over the Basic Repeat Cycle (BRC)

Level 2C
Level 2C is a superset of the Level 2B products, and contains ADM-Aeolus assisted wind fields at locations where ADM-Aeolus observations were taken. These are:

— The full L2B data set
— Wind profiles as resulting from NWP assimilation processing, using ADM-Aeolus Level 2B data
— Profile quality information needed as input to wind assimilation processing (statistically derived using product confidence data and external geophysical information)
— Atmospheric variabilities, gradients, etc. over the BRC
— References to non-ADM-Aeolus information used in data assimilation

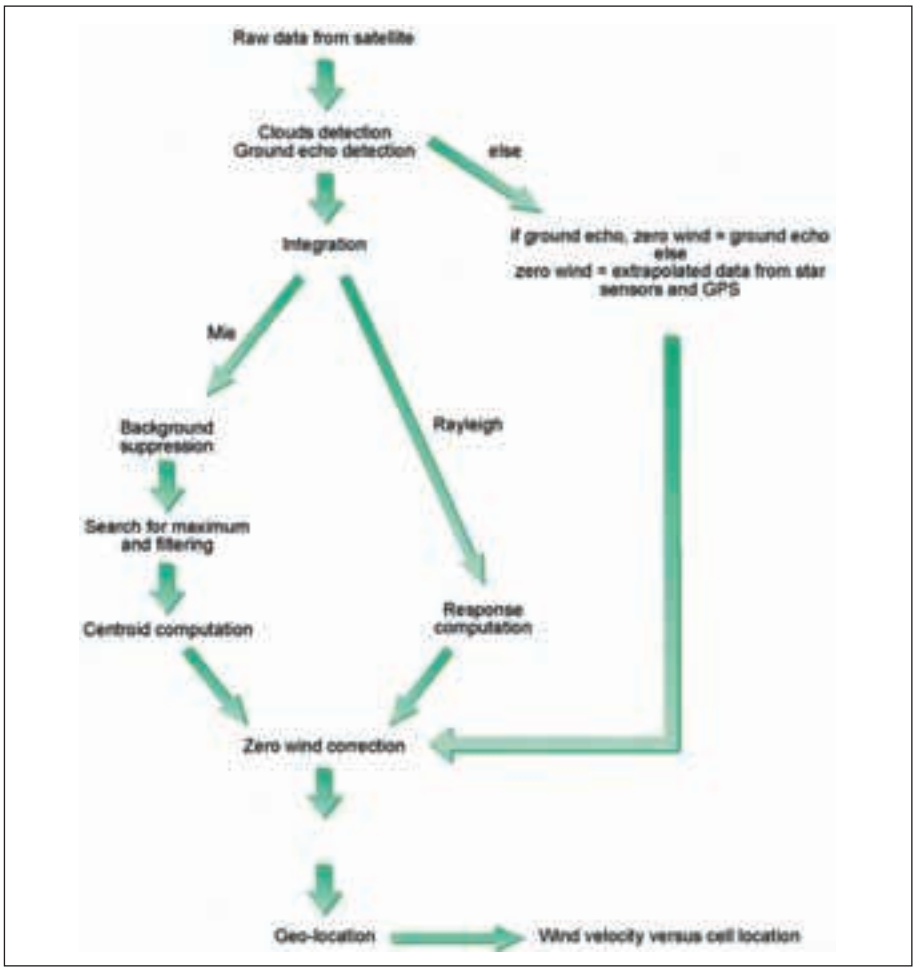

Fig. 5.3. The tasks of the ADM-Aeolus Processing Facility (APF). More sophisticated quality algorithms will be employed by the Level 2 Processing Facility (see Section 5.5).

Higher level data products

L2B data products will be assimilated by various NWP centres, e.g. ECMWF, resulting in improved wind field analyses. These wind analyses are the final product of ADM-Aeolus and will be distributed to the atmospheric research community at large.

5.2 Spectra and Doppler frequencies

The information at Level 0, shown in Figs. 5.2 and 5.3, will include all the spectral and lidar data, as well as necessary calibration and telemetry data. The spectral data basic accumulation on a shot-to-shot basis takes place in the primary detectors of the lidar. Per measurement (3.5 km integration distance), 50 laser shots are accumulated. That means that at each altitude, the cloud and clear-air returns will be mixed. For example, an accumulation of 200 independent shots (i.e., a 14 km ADM-Aeolus track) in an air layer with only 1% cloud cover would give a probability of a cloud-contaminated recording of ~ 87%. Moreover, convective clouds are broken and associated with large wind variability. Therefore, it is preferable to accumulate few shots at lidar detector level at one time, rapidly read this out for processing, and then to repeat the short accumulation sequence. Eventually, for the computation of one wind observation, several measurements (14) are carefully integrated in order to achieve a representative mean HLOS

wind. As such, some control can be exerted on the observation error while integrating the measurement spectra.

The extraction of Doppler frequencies from integrated spectra and recordings in the APF will be carried out using already prototyped software. They are based on algorithms taking theoretical evaluations and knowledge of atmospheric variability and its impact on measurements into account. The extraction requires modest levels of computing power, will be extremely rapid, and will provide processed data (Level 1B) without any significant delay. The basic outputs of such spectral processing will include Doppler frequency shift, strength of particle signal, strength of molecular signal, strength of noise background, assessment of statistical error, assessment of systematic or bias error, proportion of cloud contaminated data and proportion of null results. The Doppler shift derived from the Rayleigh channel then needs to be corrected for atmospheric temperature and pressure broadening. This is done by the Level 2B processor (Section 5.5).

5.3 Quality control

5.3.1 Errors

With respect to the error assessment of derived Doppler frequencies, two aspects need to be considered; namely statistical and systematic errors.

The main statistical error arises from the fluctuating photon-count numbers in the accumulated recordings. This can be dealt with by the algorithms estimating the instrument performance. In particular, for the Mie channel these essentially random statistical errors will be mainly dependent on the strength of the primary backscattered signal. The quality control algorithms will provide guidance on the reliability as well as the statistical errors in the individual measurements.

On the other hand, systematic errors in the derivation of the wind velocity component and height assignment can arise in a number of ways (Stoffelen *et al.*, 2002). Vertical error correlation and profile bias can be introduced by non-uniform particle distributions over a range gate providing an altitude assignment error. The assessment of aerosol signal strength and warning of severe stratification will provide a valuable safeguard against faulty assignment of altitude. Moreover, the Mie range gate resolution may be increased in the height range, where large location errors frequently appear, in order to correct such errors (see Stoffelen *et al.*, 2002).

Another source of this error arises from any inaccuracies in the spacecraft pointing and velocity restitution. The smaller the temporal scale of the random variations, the more damaging its effect will be. For ADM-Aeolus, the effect has been reduced by an appropriate selection of the instrument configuration and LOS. A good restitution of the LOS reduces the potentially large systematic HLOS wind errors. Additionally, a height calibration check will be performed on the ground return over land and sea.

5.3.2 Geolocation and ground returns

As emphasised above, precise knowledge of spacecraft pointing, position and velocity will be important in minimising systematic and bias errors in the derivation of the measured winds.

Ground returns must be considered with care. For example, signals from vegetation – crops, trees etc. – are likely to be considerably broadened by local movement, while those from moving targets will clearly give bias errors. The sea surface is the most obvious example, in which the wave spectra develop until the most dominant waves have the same speed as the local mean wind. At low surface wind speeds (creating small or no waves) the surface backscatter is too low (Menzies *et al.*, 1998). As such, proper calibration over water surfaces is very complex. Obviously, the most reliable ground returns come from bare mountain,

desert and snow-field type surfaces in calm wind conditions, i.e., in the absence of blowing snow or sand particles close to the surface.

Obstruction of the Earth's surface by cloud or fog and the subsequent absence of a ground return are additional limitations because reliable ground-truth returns may not always be as frequent as desired. The resulting errors have been taken into account in the error analyses and have been demonstrated to remain within acceptable limits. Moreover, even in the absence of a ground return, wind-shear profiles can be assimilated rather than absolute wind profiles. This will only slightly reduce performance, since effectively one vertical level is lost.

5.4 Importance of clouds

The impact of clouds on measurement capability deserves closer examination. Atmospheric transmission is hindered by the presence of clouds. On the other hand, since clouds are effective scatterers, cloud top returns provide generally strong return signals. Nevertheless, as mentioned above, the interpretation of such an above-cloud clear signal may be complicated due to the cloud dynamics. In stratiform clouds, the internal dynamics are mainly isotropic and small in magnitude, i.e. with a variability of only a few tenths of a meter per second. In convective clouds, however, cloud dynamics are anisotropic and much larger in amplitude. Here, the vertical windspeed distribution is very skewed (log-normal) and can locally be as large as 20 m s^{-1} in extreme cases (Lorenc *et al.*, 1992). Returns near convective cloud tops will thus be difficult to interpret and give a biased estimate of the mean flow. On the other hand, an anvil will often shield the strongest convective vertical motion.

By applying a criterion to reject cloud-contaminated and noisy measurements, the probability of clear-air returns is increased. Additional information about the atmospheric characteristics in the clear (Rayleigh) and cloudy (Mie) air can be inferred from the measurement data using aerosol and cloud detection algorithms as described in Section 5.6, and improved wind-profile observations can result from this.

For example, a 50% cloud cover within an observation will generally result in slightly over 50% cloud- contaminated primary recordings at the cloud level, which can be identified from the estimated Mie and Rayleigh SNR values. This cloud occurrence results in a somewhat degraded Rayleigh performance over the 50 km integration length. On the other hand, the Mie recordings from the ~ 50% cloudy returns can potentially improve the mean-wind estimate at the cloud level, if both integrated detector readouts are combined in the processing. This will be done at the Level 2/PF (see Section 5.5).

To facilitate the derivation of a volume-mean HLOS wind, Stoffelen and Marseille (1998) suggest separating cloud from clear-air returns in the processing in line with the above. Then, within a 50 km integration cluster, cases with anomalously large LOS wind or photon count variability can be detected and assigned for dedicated processing or even rejection. Research and development is ongoing to develop algorithms that effectively extract the useful information content of the measurements in these cases.

An example of lidar measurements from LITE in a tropical storm complex shows that even in cases of deep convection some cloud penetration is still possible (see Fig. 5.4).

5.5 Geophysical algorithm optimisation and monitoring

The ECMWF will develop and host the Level 2/PF (Fig. 5.2). NWP centres have a great capability to calibrate, validate, and monitor observing systems (see e.g., Stoffelen, 1998, for the ERS scatterometer). The heterogeneous data of the GOS is assimilated in such a way into a meteorological model that a

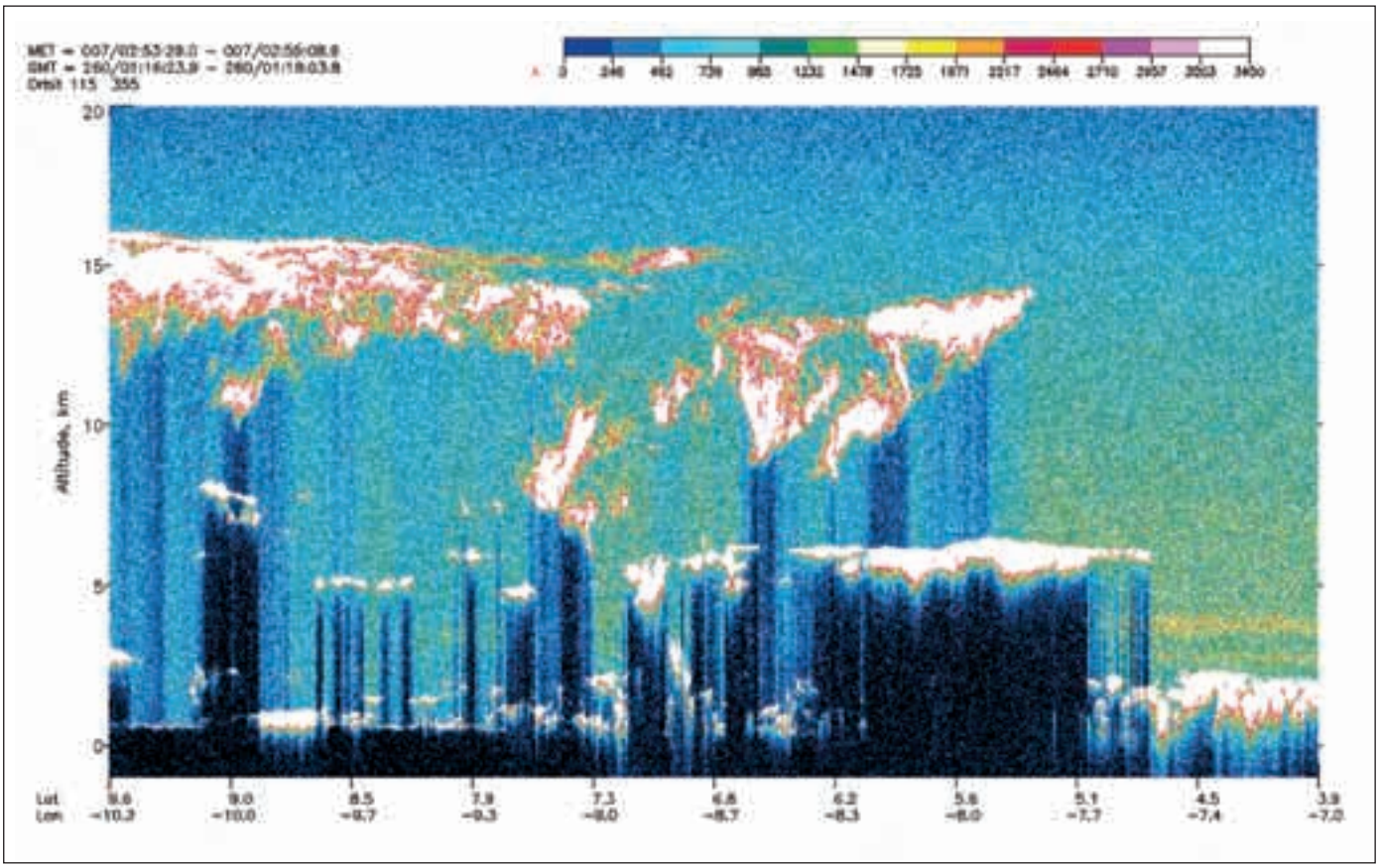

Fig. 5.4. Lidar measurements in a tropical storm complex from LITE at a wavelength of 355 nm providing some insight into the cloud penetration and DWL processing properties in extremely cloudy and dynamic situations (Courtesy, NASA). The colour scale represents the intensity of the return signal in digitiser counts.

relatively uniform quality is achieved (see Chapter 3). The comparison of the NWP-field to the observations is conducted in the observation space, that is, an observation operator is applied which translates the NWP field into an expected observation. For ADM-Aeolus, this means that the wind field is projected onto the direction of the lidar horizontal line-of-sight, and the model temperature and pressure fields are combined to obtain the Mie and Rayleigh responses. The error characteristics of the meteorological model are monitored closely by comparing it against the observations of the GOS, and therefore provide a well-known contribution in the comparison. As such, the meteorological model-state can be compared to any Doppler Lidar wind profile, and within a few hours sufficient statistics can be gathered to make judgements on the characteristics of the wind observations. The scope of the comparisons can be refined to test the ADM-Aeolus system and algorithm optimisation aspects (e.g. Stoffelen, 1998). From that moment on, useful calibration, validation, and monitoring activities can be started at the meteorological centre, and the stability of the ADM-Aeolus system assessed. For this purpose, the DWL data are collocated in near-real time with the meteorological model, but also with other related observations (i.e. radiosonde, scatterometer, cloud motion winds, and aircraft reports in the case of a DWL). This will be useful to verify and characterise instrument performance, and, more particularly, the performance in complex and heterogeneous atmospheric scenes. It is then possible to assess the representativeness and information content of the derived wind component profiles in such cases, and to adapt the observation operator (Level 2 processor) accordingly.

One more obvious and general effect that will be verified is the atmospheric temperature and pressure dependence of the Rayleigh receiver sensitivity. At the Level 1 processing stage, molecular winds are derived on the basis of a calibration curve giving the response of the Rayleigh channel as a function of the radial wind velocity. This curve is computed from calibration data under the assumption that the spectrum of the Rayleigh return light is known; its shape is assumed Gaussian with a fixed width. In reality, the width of the spectrum will vary as a function of the temperature, its shape will be modulated by the Brillouin scattering effect which is a function of both pressure and temperature, and some residual Mie light may contaminate the Rayleigh signals. For all these reasons, the response of the Rayleigh receiver must be corrected before Rayleigh winds can be assimilated. As far as pressure and temperature are concerned, the correction will use *a priori* information provided by the first-guess forecast field. Moreover, residual temperature and pressure sensitivities of the Rayleigh wind will be computed.

5.6 Ancillary products

In some cases, atmospheric spatial variability effects (shear, cloud, and aerosol) encountered during shot accumulation could cause vertical error correlation after the data processing. Such effects will be investigated in the development of the wind-profile retrieval or by performing sensitivity analysis of the DWL observation operator. In useful signal conditions it will be possible to estimate the atmospheric wind or the signal-to-noise ratio variability along the line of accumulation or integration. This would be useful not only for quality control, but also a useful byproduct to determine areas with atmospheric turbulence and cloud.

In addition to line-of-sight velocity measurements, the ADM-Aeolus space-based DWL will be able to provide information on cloud characteristics over the depth of the atmosphere, as well as aerosol measurements in the troposphere by exploiting atmospheric backscatter measurements. These include:

— cloud cover
— cloud top height (notably cirrus top and base)
— identification of multilayer clouds
— optical thickness
— profiles of aerosol extinction-to-backscatter

Other information that could be retrieved from the measurements is:

— a measure of wind variability, e.g. caused by clear-air turbulence
— tropopause and PBL height by simultaneous inspection of simultaneous aerosol and wind profiles

The properties of these secondary products are determined by the requirements for the wind-profile product. The vertical resolution of the secondary products is the same as the one used for the velocity measurements. The horizontal resolution of the information is 3.5 km (or possibly down to 1 km), depending on the shot-accumulation strategy. The development of these ancillary products has been taken up in parallel to the development of the primary ADM-Aeolus wind product.

At present, cloud properties are prognostic variables in some atmospheric models, but will be even more so in the future. Moreover, aerosol variables are currently being considered for implementation in NWP models. In a four-dimensional data-assimilation scheme, some of the DWL cloud and aerosol

products may be assimilated directly in the atmospheric analysis. This cloud and aerosol information is relevant for radiative-transfer calculations in the model, particularly information regarding the overlap of subsequent vertical cloud layers (see also Chapter 7). Tropopause and PBL height may also be validated against forecast and general circulation models. Moreover, DWL cloud top winds are a unique validation of cloud-motion winds measured by geostationary and polar-orbiting satellites. When the tropospheric combined aerosol and wind products are inserted as tracers in the data-assimilation system, this will not only benefit radiative-transfer calculations, but also chemistry computations. This in turn may be helpful for ADM-Aeolus data processing.

5.7 Improved wind field analyses

When the calibration, validation, quality assessment, and monitoring activities are fully in place, meteorological centres will start to produce meteorological analyses and forecasts including DWL data, in parallel to their reference operational suite where DWL profiles are not used (control). The first-guess field incorporating past DWL observations will then be compared to the most recent observations in the GOS, in parallel with similar comparisons of the control first-guess (see Chapter 3). Thus, an assessment will be made of the improvement in the first guess due to the DWL data. A similar validation will be performed on the experiment and control forecasts.

If the DWL data prove beneficial for the analyses and forecasts, they will be incorporated into the operational suite. Obviously, monitoring activities will be crucial at this point, because a corruption of the analyses and forecasts due to an instrument anomaly has to be avoided. The Level 2/PF (ECMWF) will use the collocated observation and first guess field products in order to validate and improve the processing. In turn, the improvements in the processing or quality assessment will be of benefit to the assimilation at the meteorological centres, thus providing a direct feedback loop. The operational use of the data signifies the most successful demonstration of ADM-Aeolus, since forecast impact is generally only achieved after an improvement in the meteorological analyses. The scientific community at large will use these analyses to perform atmospheric circulation or tracer advection studies. A proper analysis of the atmospheric state and transport properties is fundamental for studying the Earth's climate system on several spatial and temporal scales, as outlined in Chapters 2 and 3. Atmospheric analyses are increasingly used to study the complex climate system, and re-analysis projects aim at providing consistent long-term series (ERA15, ERA40).

5.8 Conclusions

The concept of scientific data processing presented in this chapter is the most effective means of implementing the processing of the DWL observations. It relies on the infrastructure already in place at major meteorological centres. This is expected to be the most efficient way of establishing the required means for the end-to-end processing (including quality control and validation) of ADM-Aeolus. ADM-Aeolus will accelerate the development of tailor-made processing algorithms and would considerably enhance the feasibility-assessment of a full-scale ADM-Aeolus follow-on DWL system measuring three-dimensional winds for better determining atmospheric dynamics.

6. Validation of ADM-Aeolus

The validation of ADM-Aeolus started in the early 1990s with the development of several experimental Doppler lidar systems and the conducting of experimental campaigns to test and compare the various possible technologies. The VALID 2 campaign (see Section 6.1) was one of them. Over a period of four weeks, several heterodyne and direct detection lidars were operated concurrently and their data were compared against well-characterised instruments measuring wind (radiosonde, profiler radar). The comparison proved that the concept of direct detection was suitable for measuring reliable winds at long ranges. This was one of the arguments leading ESA to select this technology for the ADM-Aeolus mission.

The precise design of the ADM-Aeolus lidar and the associated signal and data processing techniques will be tested during several pre-launch campaigns by flying an airborne prototype - known as the ALADIN Airborne Demonstrator (A2D). With technical characteristics close to ADM, the A2D will be operated in real conditions and acquire signals representative of the spaceborne application. The measurement results will be used to confirm the instrument concept, to improve operations and signal processing, and to develop the quality control schemes necessary to reach the high reliability needed for the spaceborne lidar data.

A few months after the launch of ADM-Aeolus, the validation of the flight model and its fine-tuning will be the object of dedicated field campaigns. During the campaigns, the ADM-Aeolus measurements will be compared to collocated measurements by ground-based or airborne observing systems. In parallel, operational data will be monitored using an atmospheric model, first offline, then on-line (see also Chapter 3). Off-line, the monitoring consists of systematically comparing observations against the equivalent analysed model fields, and building statistics on the departures. On-line, the observations are assimilated and statistics on the precision are routinely derived (typically on a monthly basis). These statistics can be used to trace the quality of the instrument performance.

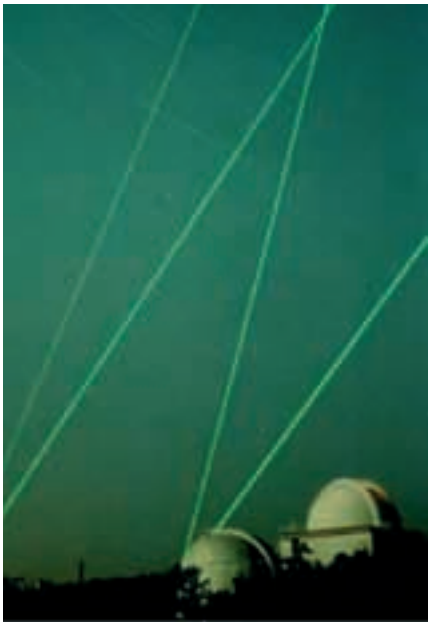

Fig. 6.1. Laser beams at the Observatoire de Haute Provence illuminating the sky during VALID-2

6.1 Concept validation: the VALID 2 campaign

The VALID 2 campaign (Delaval *et al.*, 2000) was carried out in the South of France in June-July 1999. Four different lidars were deployed and operated on the same site (the Observatoire de Haute Provence – Fig. 6.1) during a period of four weeks. Also available on the site were a wind profiling radar and a radio-sounding system, both giving 'ground truth' winds against which the other systems were compared. The four lidar systems were:

— an infrared Heterodyne Doppler Lidar (HDL) based on CO_2 laser technology operating at 10.6μm (Drobinski *et al.,* 1998),
— a near-infrared HDL operating at 2 μm,
— a dual channel direct detection lidar (DC DDL) operating at 532 nm (Souprayen *et al.*, 1999a, b), and
— a fringe imaging direct detection lidar (FI DDL) operating at 532 nm.

They were operated under different light (day/night) and meteorological conditions (weak to strong winds), thus enabling a characterisation of their respective performances over a wide range of noise and wind conditions.

Amongst the four Doppler lidars, the two direct detection systems are particularly relevant to ADM-Aeolus. The DC DDL system contains the same dual Fabry-Perot receiver system as the Rayleigh channel of ADM-Aeolus, while the fringe-imaging technique is conceptually similar to the ADM-Aeolus Mie receiver.

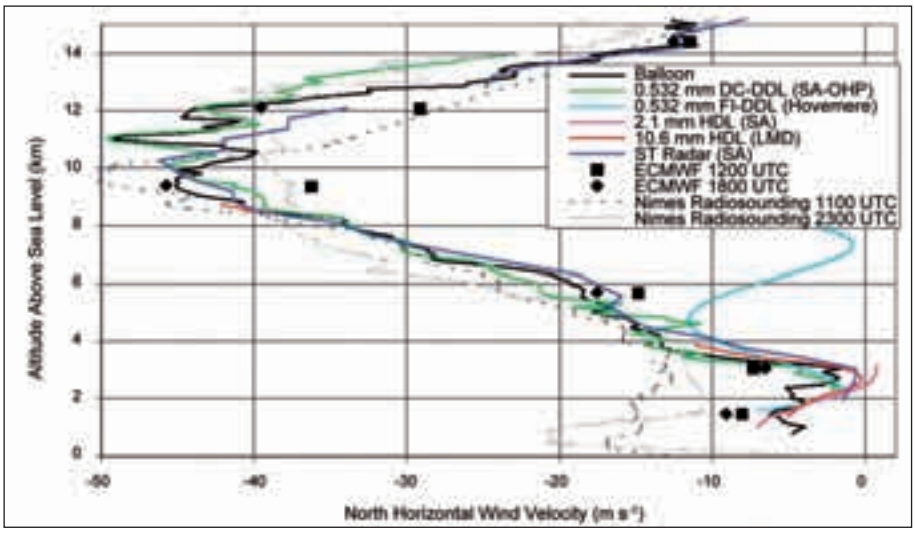

Fig. 6.2. The north-south wind component versus height, measured on 23 July 1999 (from 1500 to 1600 UTC) by the wind profiler (Strato-Tropospheric Radar), the radiosonde (balloon) and three lidars.

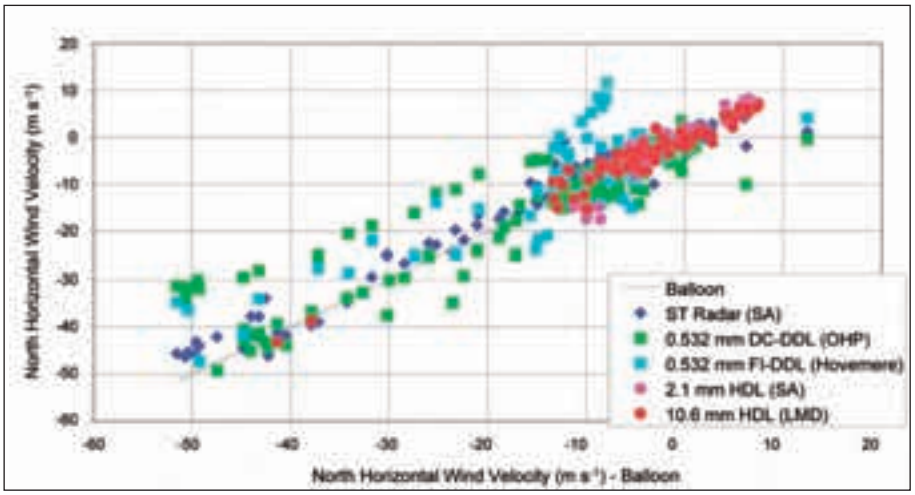

Fig. 6.3. Scatter plot of the north-south wind components measured by the four lidar systems, the radiosondes and the radar wind profiler deployed for the duration of the VALID 2 campaign (12 to 23 July 1999). The radiosonde winds on the x-axis are taken as the reference.

Fig. 6.2 displays the north-south wind component versus height, measured by three of the lidars (the fringe imaging system was not working at that time), for a particular time window (23 July 1999, from 1500 to 1600 UTC). The figure shows a good agreement between the DC DDL, the radiosonde and the wind profiler, which demonstrates the instruments abilities to perform reliable wind measurements up to high altitudes.

Fig. 6.3 shows a comparison of the measured lidar and radiosonde north-south wind components. They show a good agreement over a large dynamic range. The lidar measurements exhibiting a large departure from the radiosonde were analysed individually, and it was shown the differences could be attributed to spatial representativeness errors caused by the drifting of the radiosondes far from the Observatoire de Haute Provence.

6.2 ADM-Aeolus Validation

The pre-launch validation of the ADM-Aeolus lidar started in 2005 with ground tests and test flights of an airborne version of the satellite instrument – the ALADIN airborne demonstrator A2D (Paffrath, 2006). The A2D was developed from critical subsystems breadboarded during phase B of the project by EADS-

Table 6.1. Comparison of A2D and ALADIN characteristics.

	Satellite ALADIN	*A2D*
transmitter	Nd:YAG, tripled, diode-pumped	(as ALADIN)
wavelength	355 nm	(as ALADIN)
operation	burst-mode	continuous
repetition rate	100 Hz	50 Hz
energy pulse	120 mJ	70 mJ
laser linewidth	< 50 MHz (FWHM)	ditto
freq. stability	4 MHz rms over 7s	4 MHz rms over 14s
telescope Ø	1.5 m	0.2 m
receiver FOV	19 μrad	100 μrad
receiver aerosol	fringe imaging Fizeau interferometer, 16 channels	(as ALADIN)
receiver molecules	double edge Fabry-Perot interferometer, 2 channels, sequential	(as ALADIN)
detection	accumulation CCD, quantum efficiency 0.85	(as ALADIN)
nadir angle	35°	20°
altitude	408 km	10 km
min. vertical resolution	250 m	300 m
platform speed	7600 m s^{-1}	200 m s^{-1}

Astrium and DLR (Deutsches Zentrum für Luft- und Raumfahrt (Reitebuch *et al,* 2004; Durand *et al.,* 2006). The validation is planned in two phases, with a ground campaign performed in October 2006 and two airborne campaigns in 2007 and 2008. Measurements during a wide range of meteorological conditions will provide information about the capabilities of the space-based system. The measurements will be analysed and used for the testing of the level 1 and level 2 processing algorithms. The post-launch validation phase will start a few months after launch, once the instrument has been successfully turned on for operation, and the initial calibration has been performed. As mentioned in the introduction of this chapter, when the ADM-Aeolus data are produced operationally, they will be systematically compared to predicted meteorological fields, enabling the estimation of error statistics. These statistics will be used to check that the specifications are met and to verify the processing algorithms.

6.2.1 Validation of the Aladin Airborne Demonstrator – A2D

6.2.1.1 Comparison of A2D with ALADIN

Similar to the space model, the A2D incorporates the laser and the receiver breadboard that was developed in parallel to the phase B of the project. The objective is to operate the A2D on ground and aboard the DLR Falcon 20 research aircraft. This is done to test the measurement concept in a downward looking configuration as from space, to validate the processing software on real data, and to study the impact of real atmospheric heterogeneities on the data quality. Fig. 6.4 shows how the instrument is mounted inside the aircraft.

The major characteristics of ALADIN and the A2D are listed in Table 6.1. It can be seen that the two lidars are very similar, demonstrating that the results obtained by the A2D will be directly applicable to the spaceborne ALADIN instrument. The major differences between the two systems relate to the carrier flying at different altitudes and speeds. Flying on an aircraft with a maximum altitude not exceeding 12 km, the A2D will not be able to probe the atmosphere at high altitudes above the tropopause, whereas ALADIN is expected to provide unique wind measurements throughout the whole troposphere and lower stratosphere. On the other hand, the relatively slow carrier speed of the aircraft will permit the sounding of the atmosphere with a much finer horizontal resolution. This will be

Fig. 6.4. The ALADIN Airborne Demonstrator – A2D – inside the DLR Falcon 20 during test flights in October 2005. Courtesy of DLR.

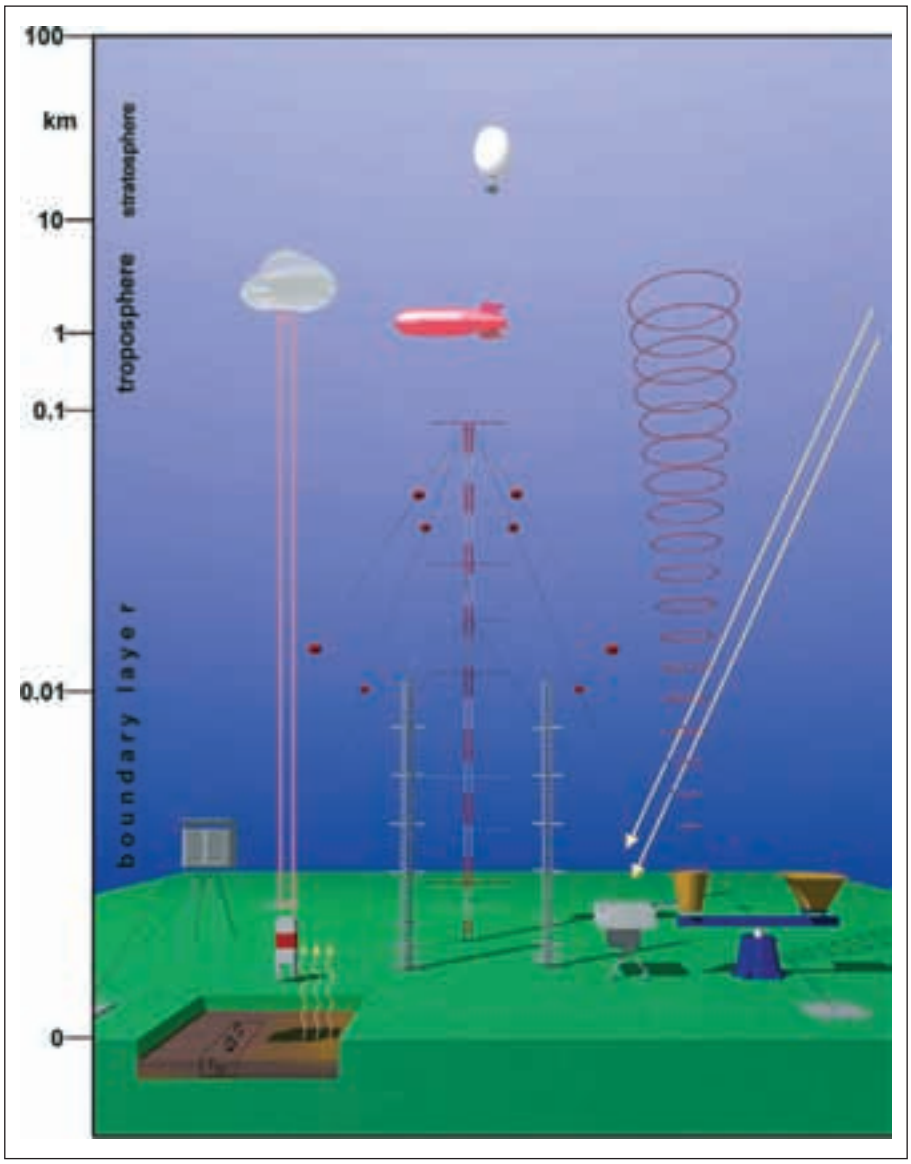

Fig. 6.5. The Lindenberg Column – the basic instrumentation consists of a 482 MHz wind profiler with RASS (Radio Acoustic Sounding System) (wind up to 16 km, temperature up to 3 km), a 1290 MHz wind profiler (wind up to 1.5 km) and a 35.5 GHz cloud radar (vertical velocity). This is complemented by a laser ceilometer (clouds up to 12 km altitude, aerosol backscatter in boundary layer), a microwave radiometer (profiles of water vapour and temperature up to 10 km). In addition, there are a 355 nm Raman-lidar for profiles of water vapour during night and a sun and star photometer (optical depth day and night). This is complemented by 4 routine radiosondes per day and a tethered balloon system. From Neisser *et al.*, 2002. Copyright 2002 E. Schweizerbart'sche Verlagsbuchhandlung oHG. Reproduced/modified by permission of E. Schweizerbart'sche Verlagsbuchhandlung oHG.

of great help for analysing the impact of small-scale atmospheric heterogeneities on the relatively coarse resolution for the ALADIN performances.

6.2.1.2 Ground-based validation

Two ground-based campaigns of the A2D were performed in October 2006 and July 2007. During two periods of several weeks, the A2D was deployed at the Meteorological Observatory of the German Weather Service at Lindenberg, Germany (Fig. 6.5). The campaigns were conducted under the supervision of the "Institut für Physik der Atmosphäre" at DLR (DLR-IPA). The radial velocity profiles of the lidar were systematically compared to wind measurements by the operational radar wind profiler of the observatory, by radiosondes, and by the DLR 2 μm Doppler lidar. The radar wind profiler data have been monitored for many years, so its error characteristics are known (Steinhagen *et al.*, 1998). Additional instruments were used to characterise the optical properties of the atmosphere, such as the aerosol lidar from the University of Munich, the DWD

Table 6.2. Overview of the instrumentation that will be used during the A2D ground-based and airborne campaigns.

Campaign	*Location*	*Time*	*Instruments*
AGC ADM-Aeolus Ground Campaigns	DWD Lindenberg	2 x 4 weeks October 2006 July 2007	- A2D (DLR) - 2µm Doppler-Lidar (DLR) - Aerosol lidar MULIS (University Munich) - Raman lidar RAMSES (DWD) - 482 MHz Windprofiler Radar (DWD) - 1290 MHz Windprofiler (DWD) - Laser Ceilometer (DWD) - 35.5 GHz Cloud Radar (DWD) - Sun Photometer (DWD) - 4 operational radiosondes per day + 10 additional (DWD)
AC01 ADM-Aeolus Airborne Campaign 1	overflights of DWD Lindenberg and other sites	15 days autumn 2007	- A2D and 2µm Doppler-Lidar aboard the DLR Falcon - DWD Lindenberg instruments as in AGC
AC01 Aeolus Airborne Campaign 2	North-Atlantic or Tropics	17 days autumn 2008	- A2D and 2µm Doppler-Lidar aboard the DLR Falcon - Additional instruments, if ACO2 is linked to another campaign

Raman lidar and sun-photometers, thus permitting a complete validation of the photon budget of the instrument (Table 6.2). A first objective was to check that the statistics of the detected signals (signal strength, the number of photons in channels A and B of the double Fabry-Perot, the number of photons on the 16 CCD elements of the Mie channel or the SNR) are in agreement with the performance predictions from end-to-end simulations. This implies that a proper calibration of the instrument (the transmission through the various optical elements has to be known) has been done by validating the entire calibration cycle designed for the space-borne instrument. After this has been successfully done, the raw data are processed with the algorithms developed for the ground segment of ADM-Aeolus adapted to the ground-based A2D case. The quality of the processed data is analysed at different stages (Level 1B, 2A, 2B). A particular emphasis is put on the evolution of the performances as a function of the SNR, as well as the degrading impact of atmospheric heterogeneities like wind or backscatter gradients along the line-of-sight.

6.2.1.3. A2D – First Airborne Campaign

In fall 2007, the A2D was integrated aboard the DLR Falcon 20 (see Fig. 6.6) together with the 2 µm Doppler lidar from DLR (Köpp *et al.*, 2004; Weissmann *et al.,* 2005) to test the A2D in a first 15-day airborne campaign. The quality of the A2D data will be determined by comparisons to the ground-based data (see Table 6.2), thus enabling the characterisation of errors associated with the moving platform (attitude, bearings, speed). Flights with similar objectives as for the ground-based campaign were performed to assess the performance of the instrument for different atmospheric conditions. The purpose was to fly above weather patterns known for both their heterogeneity and their critical impact on the evolution of the weather (fronts, jets), and test the ability of the airborne instrument to make useful measurements there. A particular emphasis was put on the ability of the algorithms to detect the weather features that prevent the instrument from making useful measurements (e.g. cloud and aerosol contamination), and possibly correct the data.

Fig. 6.6. The DLR Falcon 20 in flight. Courtesy of DLR.

6.2.1.4 A2D – Second Airborne Campaign

A second airborne campaign will follow in autumn 2008. As for the first airborne campaign, the A2D will fly aboard the DLR Falcon 20 together with the DLR 2-μm Doppler lidar. The purpose will be to elaborate further on the analysis of the ability of the system to make useful measurements in critical areas of the atmosphere. The target regions and the particular features to be studied are still to be determined. A dedicated experimental campaign could be organised, but the most favourable option would be flights during an already planned field experiment (see Table 6.2). During such campaigns, a large instrumental set-up is deployed that combines a wide variety of ground based and airborne sensors, giving a description of the state of the atmosphere with an unusual wealth of detail. Moreover, simulation experiments are carried out with atmospheric models, during which the observations are used to produce the best possible estimates of the atmospheric state. All this information would certainly be of great value when analysing the observations of the lidar and help in the determination of their quality.

The objective of the airborne ADM-Aeolus experiment will be to produce data that can be processed by the operational processing chain developed for ADM-Aeolus (with adaptations for the airborne case), test the quality control procedure, and analyse the performances of the instrument in the real, heterogeneous atmospheric conditions that the spaceborne instrument is most likely to encounter.

6.2.2 Validation of the spaceborne system

After ADM-Aeolus has been successfully launched and put into operation, the inflight validation will start. Traditionally, the validation of an instrument already in space comprises several types of parallel activities. One type consists of carrying out field experiments during which independent ground-based or airborne observations and the space-based data are compared and analysed. A second type consists of comparing the space-based data with weather predictions, either offline or routinely as part of a monitoring activity.

Fig. 6.7. The WIND instrument embarked on the DLR Falcon. Courtesy of DLR.

6.2.2.1 Field experiments

The most direct way of validating an observation system is to compare its observations against observations from other, proven sensors. For ADM-Aeolus, the difficulty is to obtain comparable observations. ADM-Aeolus observations are representative of the actual wind field on a spatial scale of only 50 km. Comparable observations have thus to be co-located with ADM-Aeolus footprint to less than 50km. This can hardly be achieved with a ground-based system. An option is to use an airborne system. Several airborne Doppler lidars exist in Europe, namely the 10 μm WIND (Wind Infrared Doppler lidar, Werner *et al.*, 2001; Reitebuch *et al.*, 2001, Reitebuch *et al.*, 2003) and the 2 μm Doppler lidar at DLR or the A2D mentioned above. At the moment, these instruments can fly onboard the DLR Falcon 20. The possible installation of WIND aboard the CNRS (Centre National de la Recherche Scientifique) Falcon 20 is currently planned and could be a viable option by the time ADM-Aeolus is in orbit. Fig. 6.7 shows the WIND instrument embarked on the DLR Falcon.

For the validation, the airborne Doppler lidar would fly one leg along the orbit of the satellite, making measurements of wind vector or radial wind velocity in the same atmospheric volumes. By averaging airborne data to the spatial resolution of ADM-Aeolus (50 km), it should be possible to produce observations of similar representativity, which can thus be compared directly to ADM-Aeolus data. The total duration of the observation campaign needed to achieve a relevant validation is still to be determined. It should include flights over many different types of typical weather features to assess the behaviour of the spaceborne instrument in a large variety of weather conditions and the capacity of the processing chain to cope with them.

6.2.2.2 Routine Validation Against Meteorological Analysis

NWP data assimilation systems provide accurate estimates of the state of the atmosphere at any time and place of an observation (see Chapter 3). They seek to optimally combine the available sources of information provided by the operational observation networks, as well as the governing laws of the state of the atmosphere implemented by the numerical models. The resulting synthesis of observations and model information is called the analysis.

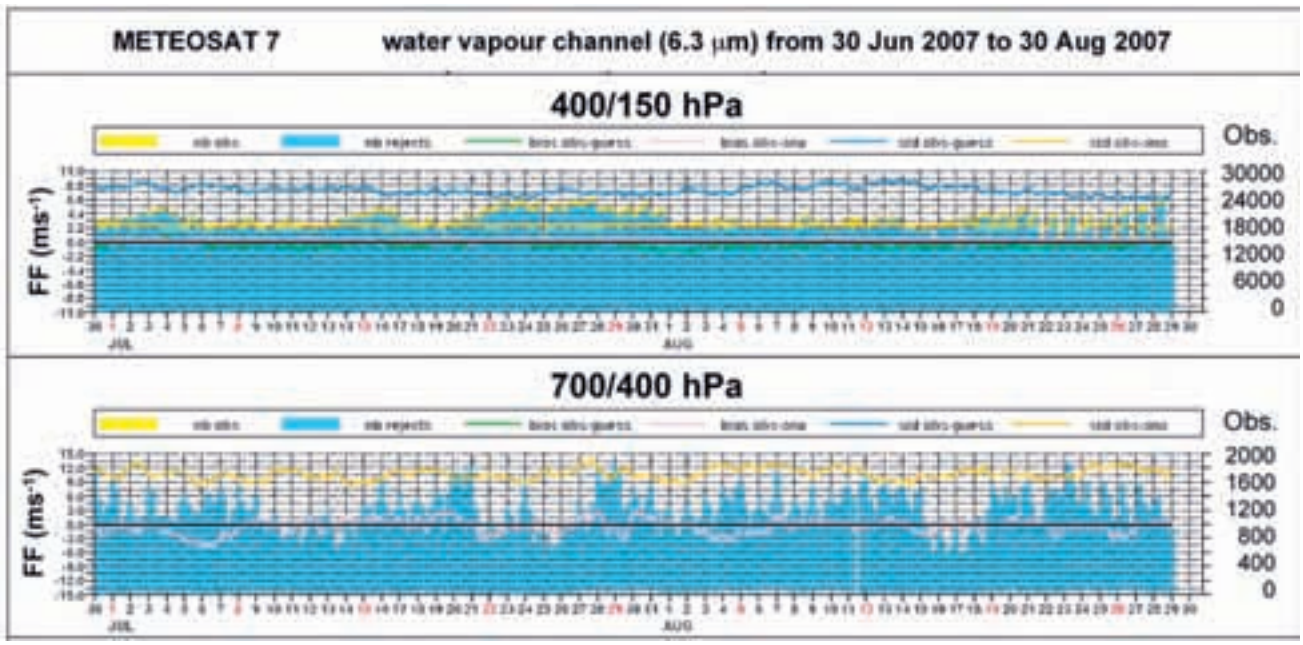

Fig. 6.8. Monitoring by the French global NWP system ARPEGE of the wind observations derived from Meteosat-7 water-vapour channel between the 30th of June 2007 and the 30th of August 2007 in the 150 hPa to 400 hPa (top) and 400 hPa to 700 hPa (bottom) altitude ranges. Orange shaded area: number of observations available to the assimilation. Light blue shaded area: number of observations rejected by the assimilation process. Green curve: bias of observations versus first guess (m s^{-1}). Magenta curve: bias of observations versus analysis (m s^{-1}). Dark blue: standard deviation of observations versus first guess (m s^{-1}). Orange: standard deviation of observations versus analysis (m s^{-1}).

NWP analyses are extensively used for validation and routine monitoring of satellite observations. Based on all available atmospheric observations, NWP analyses are the best estimate of the state of the atmosphere at a given time. The analysis field and the observations are then compared, and the differences are accumulated over a period of time. The comparison can reveal biases in the observations, giving an indication of the typical magnitude of random errors, and identifying gross errors. Routine monitoring of this kind is implemented for a wide range of observing systems at most major NWP centres.

For ADM-Aeolus, the analysis wind field will be projected onto the direction of the lidar horizontal line-of-sight, and the temperature and pressure fields will be used to obtain the Mie and Rayleigh responses. The differences between the calculated and actual observations are due to errors in the observing instrument, the data processing, and the NWP. The statistical structure of NWP errors is relatively well known and characterised. The residual error can be attributed to the instrument and/or data processing deficiencies. Its statistical characteristics can help determine the error parameters. The error parameters are then used by the analysing system to obtain the appropriate weight of the new information in the initial assimilation trials.

The validation by the NWP analyses will start in an offline mode during the validation field experiments. Vertical profiles of wind, temperature and pressure at the location corresponding to the airborne observations will be extracted from NWP fields and processed as described above.

It is planned that a systematic comparison with NWP analysis will be implemented and run during the first months of ADM-Aeolus operations. All available, quality-checked ADM-Aeolus data will be compared to NWP analyses. Statistics will be derived in terms of bias and standard deviation. The results will help fine-tune the processing chains, check that the specified performance is achieved, and compare it to the performance of the other observation systems producing similar observations. This is done in order to establish their respective merits.

After a few months of 'passive' NWP validation, the operational assimilation of ADM-Aeolus data can start, provided that the data quality is consistently good. The assimilation systems will then produce monthly statistics of the analysis versus observation differences and comparisons with *in situ* wind observations, thus permitting powerful monitoring of the quality of ADM-Aeolus data throughout the entire lifetime of the instrument.

An example of routine validation using radiosondes is shown in Fig. 3.6. Another example is shown in Fig. 6.8. The figure summarises the monitoring statistics from the French global NWP system ARPEGE (Action de Recherche Petite Echelle Grande Echelle - French climate model) of the wind observations derived from Meteosat 7 water vapour channel between 30 June 2007 and 30 August 2007, in the altitude intervals 150 hPa to 400 hPa, and 400 hPa to 700 hPa. The number of rejected observations is close to the number of available observations because many observations are redundant (closer in time and space than the model space and time resolutions), or because their height assignment is wrong (this is particularly visible in the 700 hPa to 400 hPa height interval, where wind gradients are strong in the atmosphere – so the sensitivity to the height assignment is larger). It can be seen that the statistics were rather stable throughout the entire period. They are a good indication of the precision reached by the observation system. A sudden temporary degradation of the statistics indicates a degradation of the observation system rather than a noticeable failure of the forecasting system.

7. Expected impact of ADM-Aeolus wind, cloud and aerosol observations

7.1 Impact in a range of applications

Meteorological observations are an essential component of NWP. In operational practice, a wide variety of observations are assimilated into computer models to provide accurate simulation in near-real time of the ever changing state of the atmosphere (see Chapter 3). The data assimilation process provides comprehensive 'analyses' of the atmosphere serving as the starting point ('initial condition') for numerical weather forecasts. The ADM-Aeolus mission has been designed to demonstrate an impact of space based wind-profile measurements on NWP and climate re-analyses. The ADM-Aeolus aerosol and cloud products are expected to improve our knowledge about the three-dimensional structure and transports of clouds and aerosols, as well as their radiative and optical properties.

The actual impact of the real ADM-Aeolus data will be investigated and assessed during the operational phase of the mission using state of the art data assimilation systems in both global and regional applications. Later on, and for many years after the end of the mission, the ADM-Aeolus data will contribute to climate re-analyses, and to specific processes studies on atmospheric motions. In anticipation of the actual ADM-Aeolus data, preparatory impact studies have been performed through simulation. Simulations range from theoretical studies using idealised data and simple models, to studies that seek to emulate the future full capability of the ADM-Aeolus instrument and its impact on NWP. Simulations of specific weather events, where the development of an intense storm is very sensitive to the initial conditions, will also be carried out.

7.2 Wind accuracy in numerical weather prediction

As explained in Section 3.2.2, the data impact in NWP is often evaluated in terms of the incremental improvement obtained by adding the new data type to a baseline (reference) system, e.g. a current operational system. The measured impact will, in that case, depend on the accuracy and distribution of the new data type relative to the accuracy and distribution of data in the existing GOS, and to some extent also on the capabilities of the data assimilation system itself (Dumelow, 2003; WMO, 2004). An illustration of the accuracy to which the global wind field is currently known is shown in Fig. 7.1. The figure shows an estimate of the standard deviation of error in the east-west wind component at 250 hPa (approximately 10 km) in the ECMWF analyses. The distribution of errors is a product of atmospheric wind variability on the one hand, and the availability of accurate observations, on the other. We see that wind analysis errors are small in data dense areas (e.g. North America, Europe, Japan and Australia) and in regions with little wind variability (e.g. parts of the sub-tropics). Wind errors tend to be large in most parts of the tropics (for reasons discussed in Chapter 2), in the storm-tracks over ocean (southern oceans, N. Pacific, N. Atlantic) and along the sub-tropical jet extending from the southern Mediterranean region to northern China. It is in these areas, where current data assimilation systems have relatively high wind uncertainties, that the main analysis impact can be expected from ADM-Aeolus wind profile data.

There is a body of evidence documenting that wind-profile measurements are very important to NWP: Atlas *et al.* (1985) showed that wind data are more effective than temperature data in controlling analysis error. This has more recently been confirmed by Bouttier and Kelly (2001). The impact of existing radiosonde and pilot wind profiles has been tested in data-denial experiments (Cress and Wergen, 2001), showing that North American wind-profile data improve weather forecasting for Europe. Similarly Cardinali *et al.* (2003) demonstrated a clear positive analysis and forecast impact of wind and temperature profiling data from ascending and descending aircraft (ACAR - Aircraft Communication Addressing and Reporting system and AMDAR - Aircraft Meteorological DAta

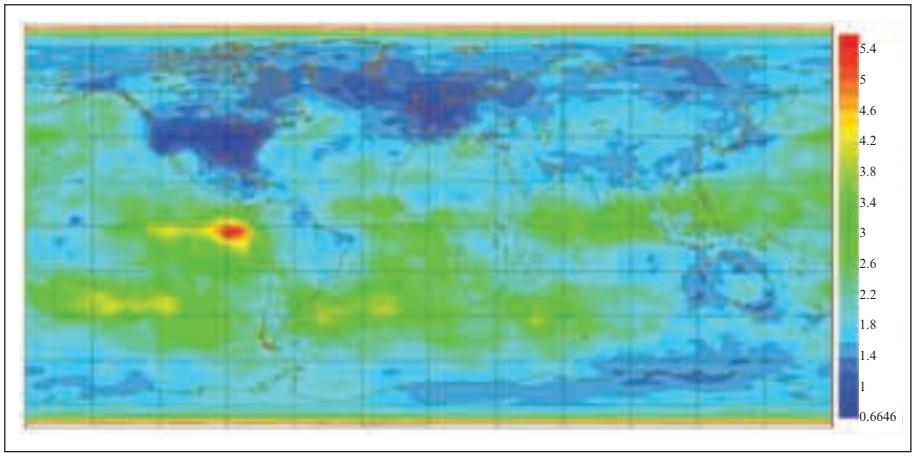

Fig. 7.1. An estimate of wind analysis uncertainty (east-west wind component at 250 hPa, in m s^{-1}) in the Autumn-2001 version of the ECMWF data assimilation system showing maxima in the tropics, and the oceanic storm track regions. Errors tend to be smaller in data-dense regions and where wind variability is less. The estimate is based on the spread between the ten members of an ensemble of assimilations, 1-31 October 2000 (Fisher, 2003a).

Relay). Investigations of specific intense storm developments over the North Atlantic have shown that they are sensitive in particular to wind data (Hello *et al*., 2000) obtained from cloud imagery (CMW - cloud motion winds). However, ADM-Aeolus wind profiles differ from conventional wind observations in two important respects:

— the data availability and the quality of the ADM-Aeolus data depends on the cloud and aerosol distributions in the atmosphere,
— ADM-Aeolus measures one component of the wind-vector, only, along the instrument's line of sight (LOS).

For these reasons, extensive ADM-Aeolus-specific impact studies have been performed.

Recent studies with assimilated measurements from the DLR airborne Doppler lidar, obtained during the Atlantic THORPEX Regional Campaign (A-TreC) in 2003, show a significant impact on analyses as well as on the 2-4 day forecast for the ECMWF global model (Weismann and Cardinali, 2007).

7.3 Simulation of ADM-Aeolus measurements and their accuracy

The accuracy of the ADM-Aeolus wind measurements will not be uniform. The SNR will primarily depend on the intensity of the backscattered laser light, which in the Mie channel depends on the presence and thickness of clouds (Becker *et al*., 1996; Astin and Kiemle, 2003) and the concentration of aerosol, and in the Rayleigh channel on the density of air. It is expected that the ADM-Aeolus instrument will receive sufficient backscatter from the layers of clear air above clouds, from cloud-top layers, from layers in and below thin clouds, and from layers with sufficient aerosol in the lower parts of the atmosphere. For each level in the vertical, Fig. 7.2 shows the relative proportions (%) of good ADM-Aeolus wind retrievals from cloud (blue), aerosol (green) and molecular returns (yellow, see legend) and the proportion of poor data (red) due to insufficient signal-to-noise ratio (simulations by Marseille *et al*., 2001).

It is important to consider whether ADM-Aeolus will provide significant numbers of high-quality data in the meteorologically most interesting regions, i.e. where incipient storms tend to occur and where storm systems develop. These so-called 'sensitive areas' tend to be associated with high cloud cover (McNally, 2002). Therefore, the yield and quality of ADM-Aeolus wind profiles have been investigated (Tan and Andersson, 2005) through detailed simulations, given

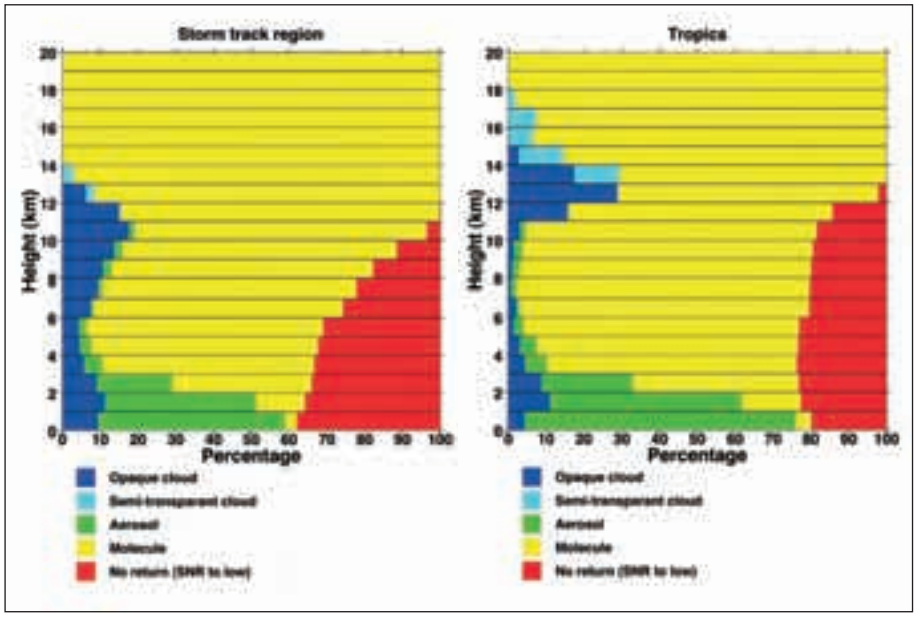

Fig. 7.2: Simulated signal-classification, showing relative frequencies (%) for five classes (see legend) for a storm-track region (left) and the tropics (right), for ADM-Aeolus wind retrievals in one km thick layers from the surface to 20 km. The large percentage of clear-air molecular returns (yellow) is partly due to ADM-Aeolus's ability to detect winds through thin clouds and in gaps between clouds. From Marseille *et al*. (2001).

realistic cloud distributions and climatological estimates of aerosol concentration (Vaughan *et al*., 1995).

The simulations of backscatter and instrument performance have been carried out using the LIPAS (Lidar Performance Analysis Simulator) software (Veldman *et al*., 1999; Marseille and Stoffelen, 2003). Given as input vertical profiles of atmospheric parameters (temperature, pressure, wind speed and direction, cloud fraction and aerosol concentration) LIPAS outputs simulated ADM-Aeolus HLOS winds as well as corresponding estimates of measurement accuracy. The user specifies parameters such as the observation resolution, shot-accumulation length and pulse repetition frequency. Various sources of instrument error (random and systematic) are modelled according to instrument specifications. Other biases, e.g. laser pointing errors and height assignment errors arising from non-uniform aerosol distributions, are modelled by LIPAS. The main outputs from LIPAS are profiles of simulated ADM-Aeolus observations at a user-specified resolution, together with estimated random, systematic and representativeness errors. LIPAS provides estimates of ADM-Aeolus observation accuracy as a sum of observation error and representativity error variances. Thus, LIPAS provides the simulated measurements and their accuracy, as required for realistic impact studies.

Examples of LIPAS simulations of the expected yield of ADM-Aeolus winds (from Tan and Andersson, 2004) are shown in Fig. 7.3. The coloured markers show the percentage of good quality data i.e. those meeting the mission-specified accuracy requirement in terms of random error. This is shown separately for wind retrievals from the Raleigh (molecular) channel in the mid-troposphere (top), and for the Mie (aerosol) channel near the surface (lower panel). These simulations are for the period 10 January to 28 February 2003 and are based on cloud cover as provided by the ECMWF forecast model at full operational resolution (T511, or ~ 40 km), climatological aerosol distributions from (Vaughan *et al*., 1995), and other meteorological inputs from the ECMWF model. We see that the yield of good data is high (>50%, green markers) in most regions, even in the storm-tracks in the mid-troposphere. The yield is low (red markers) mainly in the most persistently cloudy regions, i.e. the ITCZ (Inter-Tropical Convergence Zone),

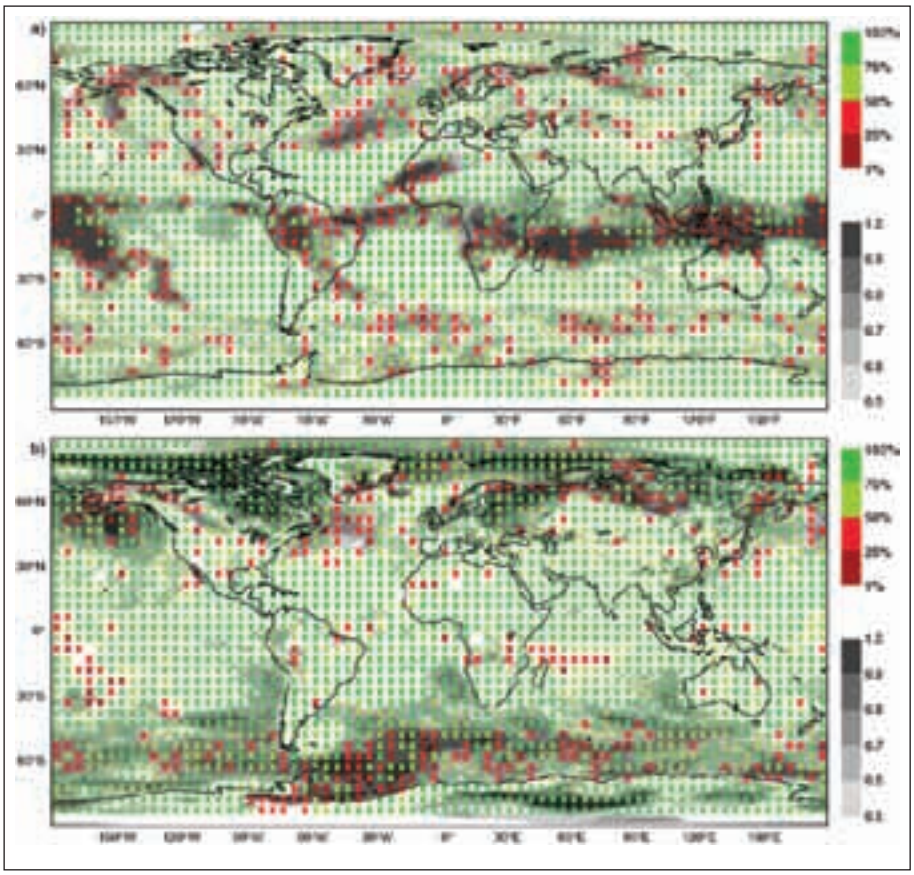

Fig. 7.3. Simulated ADM-Aeolus yield of good quality data for (a) the Rayleigh (molecular) channel at 4–5 km and (b) for the Mie (aerosol) channel at 0.5–1 km, in terms of percentage of good data in each 5 by 5 degree box meeting mission requirements as represented by green and red markers (see legend). Based on simulations through the period 10 January to 28 February 2003. Grey shading shows ECMWF cloud cover at 4–6 km (a) and 0–3 km (b) within the study period. White areas shows less than 0.5 cloud cover. (Adopted from Tan and Andersson, 2004).

and at low levels in the storm-tracks. At higher levels, (not shown) the yield of good data is near complete.

Simulated Impact

Over time, several Observing System Simulation Experiments (OSSEs) for various DWL concepts have been conducted (Atlas and Emmitt, 1991; Rohalty and Krishnamurti, 1993; Baker *et al*., 1995; Atlas *et al*., 2003; Masutani *et al*., 2004) and specifically for an ADM-Aeolus-like concept (Stoffelen and Marseille, 1998; Marseille *et al*., 2001; Stoffelen *et al*., 2006). The impact of single HLOS winds (like ADM-Aeolus, Stoffelen *et al*., 2005a) has been contrasted with that of a scanning instrument, or dual instrument concepts with different viewing geometries. The conclusion has generally been that clear positive NWP impact should be expected, even from a single HLOS DWL, and that significantly larger impact could be obtained from enhanced (but more costly) instrument concepts (Riishøjgaard *et al*., 2004; and comments by Stoffelen *et al*., 2005b). In the study by Masutani *et al*. (2004) four different DWL configurations were studied in a set of OSSEs. The experiments were based on a T213 resolution 31-level simulation of the atmosphere provided by ECMWF for a period in February 1993. Apart from all the conventional data, DWL data were simulated and assimilated in the NCEP data assimilation system. The impact of adding the DWL data was measured with respect to the control experiment, which used all the conventional data but not the simulated DWL data. All four DWL configurations resulted in a measurable positive impact.

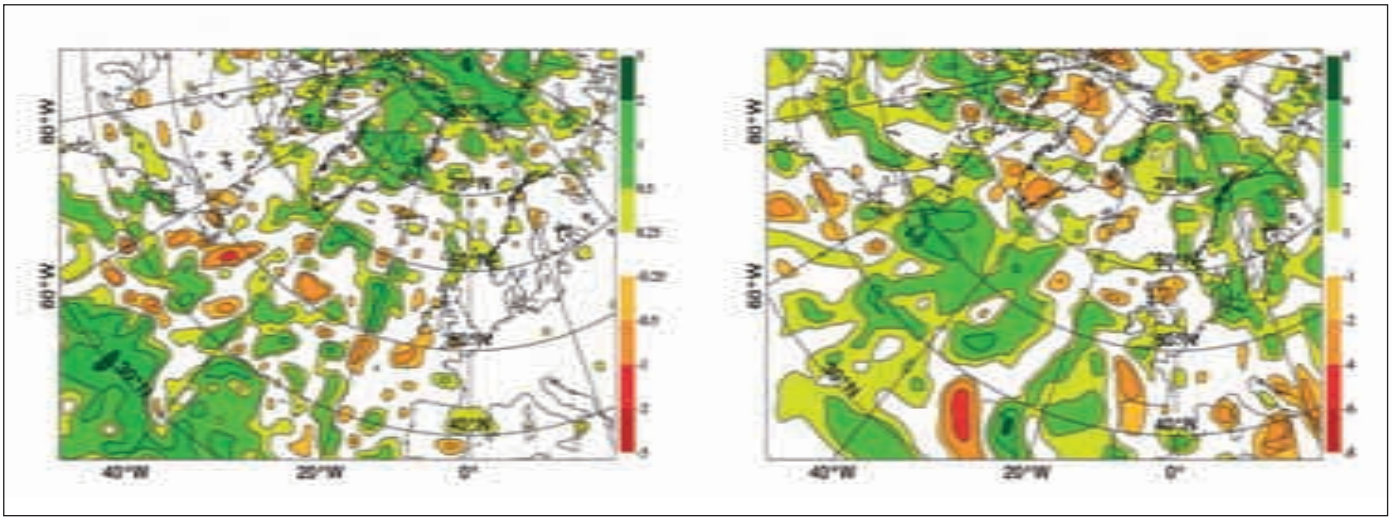

Fig. 7.4. Impact of 500 hPa lidar observations on the wind field over Europe and the North Atlantic, represented by the difference (m s^{-1}) in RMS error between a data assimilation experiments without and one with simulated ADM-Aeolus data, for (left) the analysis and (right) a 4-day forecast, averaged over 15 cases. Shaded green areas denote a positive impact, and red areas a negative impact. The lidar data have a positive impact on the 4-day forecast over Europe and the North Atlantic. From Stoffelen *et al.* (2006). This figure is reproduced/modified by permission of The Quarterly Journal of the Royal Meteorological Society.

7.3.1 ADM-Aeolus observing system simulation experiments, extra-tropics

The impact of an ADM-Aeolus-like instrument in an OSSE scenario (Stoffelen *et al*., 2006) is shown in Fig. 7.4, for the North Atlantic and Europe, in terms of difference in RMS error between an experiment without the ADM-Aeolus data and one with, for analysis and forecast error. Substantial positive impact (green shading) is shown in the wind analysis accuracy (left panel) over the Atlantic, where there is a general lack of wind observations without the ADM-Aeolus data. The forecast impact (right hand panel) is also positive, but this result is much more uncertain due to the limited OSSE period (only 15 days), especially for forecasts longer than a couple of days and for regional (as opposed to hemispheric) verification areas. However, the scatter diagram (Fig. 7.5) showing 4-day forecast impact for the extra-tropical Northern Hemisphere (north of 20°N) demonstrates that the positive result is statistically significant for the Northern Hemisphere as a whole, as the scatter of data points (representing impact) is well separated from the diagonal line representing neutral result. Stoffelen *et al*. (2006) reported that the average impact of the ADM-Aeolus-like lidar data on medium-range forecast in the OSSE was about 0.25 days, i.e. 6 hours, in the Northern Hemisphere (north of 20°N). Put in the context of Fig. 2.9, this result indicates that the ADM-Aeolus could provide similar benefit to NWP as that from the radiosonde network.

7.3.2 Tropics

In the tropics, the wind field is dominated by equatorial waves forced by convection (see discussion in Chapter 2). The spatial structure of tropical wind errors is therefore fundamentally different from those at higher latitudes (Žagar *et al*., 2004b; 2005), which is an important consideration in tropical data assimilation. We have seen from Fig. 7.1 that wind analysis errors are large in the tropics. This is partly because of the difficulty in predicting the convection and its influence on the wind field. It is also because of the current lack of direct wind measurements there, and because it is difficult to infer wind field information from the available temperature (or mass) information in the tropics (Žagar *et al*., 2004a). The Masutani *et al*. (2004) OSSE study (mentioned above) showed a very clear positive impact in the tropics from all four tested DWL configurations.

The assimilation of equatorial waves by HLOS wind observations has been studied by Žagar (2004). The question was how well a typical idealised tropical wind and mass field could be reconstructed using various sets of observational

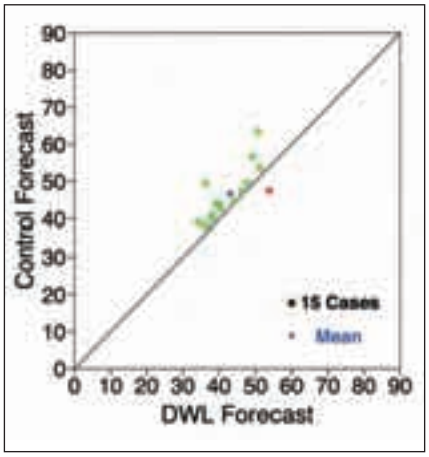

Fig. 7.5. RMS of the 4-day forecast error for the assimilation using simulated ADM-Aeolus data (x-axis) plotted against corresponding results from a control assimilation without the ADM-Aeolus data (y-axis), in terms of 500 hPa geopotential height (m) for the Northern Hemisphere north of 20°N. Circles indicate each of the 15 individual forecasts, in green when ADM-Aeolus is beneficial and red when not. The cross represents the mean over the 15 cases. This is a fairly limited data set but still significant as the cluster of data points is well separated from the diagonal line representing a neutral result. From Stoffelen *et al*. (2006). This figure is reproduced/modified by permission of The Quarterly Journal of the Royal Meteorological Society.

data. In particular, the benefit of tropical HLOS winds was assessed by comparing their data assimilation impact with that of full wind vector and mass information. A summary of the results is reproduced in Fig. 7.6. The figure suggests that HLOS wind observations provide valuable supplemental information to the existing satellite mass field measurements. The mass data (h) alone do not reproduce the wind field very well. Although the new wind information is incomplete (single-component wind) it improves the analysis of tropical wave motions, especially when it is used together with the mass data (the experiment labelled 'h & los' in the figure).

7.3.3 Impact assessment using ensemble simulations

The global impact of ADM-Aeolus data has most recently been investigated through assimilation ensemble experiments (Tan and Andersson, 2004). This is a novel approach that is being developed and applied for the first time in these ADM-Aeolus simulations. Previous work with assimilation ensembles has had a different focus, namely diagnostic studies of errors in assimilation systems, leading at ECMWF to improved specification of background error covariances (Fisher, 2003a) and a revised humidity analysis formulation (Hólm *et al*., 2002) and investigation of tropical mass-wind balance relationships (Žagar *et al*., 2005). Such work has implications for NWP exploitation of ADM-Aeolus data but does not in itself attempt to quantify data impact. Tan and Andersson extended the assimilation ensemble method to assess the impact of different observations types: simulated ADM-Aeolus data and, for calibration purposes, radiosonde plus wind profiler data. This has required the generation of new ensembles that differ in the observations made available for assimilation. Three ensembles were generated, and each ensemble consisted of 4 independent members; each member was run for the period 10 January to 28 February 2003. The three ensembles differed in the observations that were assimilated as follows:

— Control: All observational data used as in the 2004 ECMWF operational system,
— ADM-Aeolus: As Control with simulated ADM-Aeolus data added,
— 'No-Sondes': As Control but radiosondes and wind-profilers were removed.

Statistics, such as the spread within a particular ensemble, were compiled for the period 16 January to 28 February 2003 (to disregard common initial conditions). A beneficial impact of observational data corresponds to a reduction in ensemble spread. Comparison of the Control and 'No-Sondes' ensembles permits essential calibration of the results, and facilitates a relative assessment of ADM-Aeolus and radiosonde impacts. Development of the approach was motivated by two significant advantages over the traditional OSSE approach for assessing the impact of anticipated data. The first is that the method is based on real observations, thus obviating the need to simulate observations other than the anticipated new data (ADM-Aeolus in this case). The second is that, whereas OSSE results are difficult to interpret because of uncertainties surrounding the role of simulation biases, the situation is not so severe in the assimilation ensemble approach. This is because the ensemble approach has permitted the development of diagnostics based on relative differences between ensemble members, cancelling systematic biases.

The results (Fig. 7.7) suggest that the main benefits from ADM-Aeolus (compared to Control) for analysed wind fields will be found over ocean regions in both hemispheres and in the tropics, and over parts of central Asia. These regions have been identified in Chapter 2 as priority areas for improvement. The benefits seen in analysed fields lead to benefits in forecasts as well (Fig. 7.8).

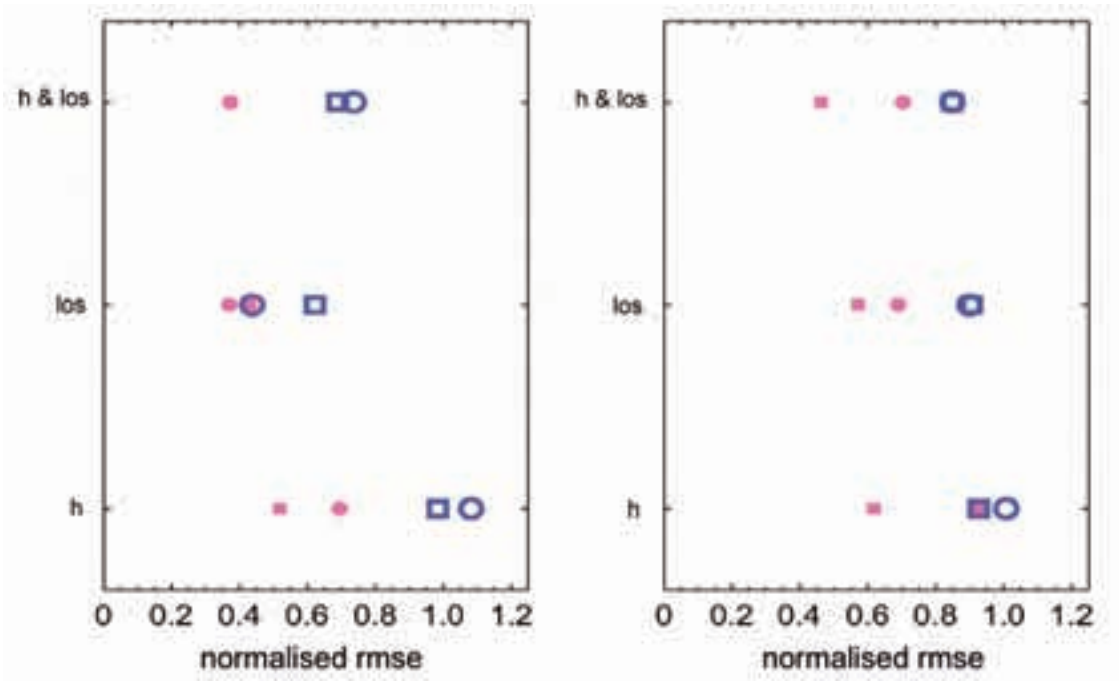

The graph shows the ensemble spread between 12-hour forecasts, averaged over the tropics, for the Control, ADM-Aeolus and 'No-Sondes' ensembles. A global calibration factor close to two is required to obtain the correct overall magnitude corresponding to actual wind uncertainties in the ECMWF system. It is evident that the impact of simulated ADM-Aeolus data compares favourably with radiosonde/wind-profiler data. Apart from the small differences between the curves for ADM-Aeolus and Control between 1000 and 850 hPa, all other differences are found to be significant according to Student's T-test ($p < 0.001$). The results are largely in agreement with what has been discussed in this chapter in terms of expected ADM-Aeolus impact. The large impact in the tropics is noteworthy. It is likely that the ADM-Aeolus wind data help determine the moisture-convergence at low levels in the region of the ITCZ, as well as the divergent outflow in the upper troposphere. It is hoped that the ADM-Aeolus data will help maintain a more correct intensity of the Hadley circulation than is currently the case at ECMWF (Andersson *et al.*, 2005) in the operational system and ERA-40 climate re-analyses.

Fig. 7.6. Root mean square error (rmse) of the zonal wind (left) and the meridional wind (right) components, for various 3DVAR (circles) and 4DVAR (squares) experiments of multiple equatorial waves. The values are scaled by the rmse of the background field. Experiments with different observations are marked by the following symbols: height data (h), ADM-Aeolus LOS winds (los), and height data and ADM-Aeolus LOS winds (h & los). The results are shown for a perfect background covariance matrix (magenta) and an imperfect background error covariance matrix including only equatorial Rossby and westward-propagating equatorial inertio-gravity waves (blue). In most cases, the best tropical wind analysis is obtained when ADM-Aeolus LOS wind data is used in combination with height data. After Žagar (2004).

7.3.4 Information Content

The results just presented suggest that the impact of simulated ADM-Aeolus data is comparable to the impact of radiosondes plus wind-profilers in terms of assimilation ensemble spread. In this section, we complement this result with an assessment in terms of information content. Practical methods for computing information content (Degrees of Freedom for Signal - DFS) in the observations and analyses have recently been developed (Cardinali *et al.*, 2004; Fisher, 2003b) within the context of the global 4D-Var assimilation system. The results for each of the main current observing systems, as obtained by Cardinali *et al.* (2004), are reproduced here in Fig. 7.9. Large DFS is obtained from satellite sounding data particularly in terms of temperature in the stratosphere (e.g. AIRS and

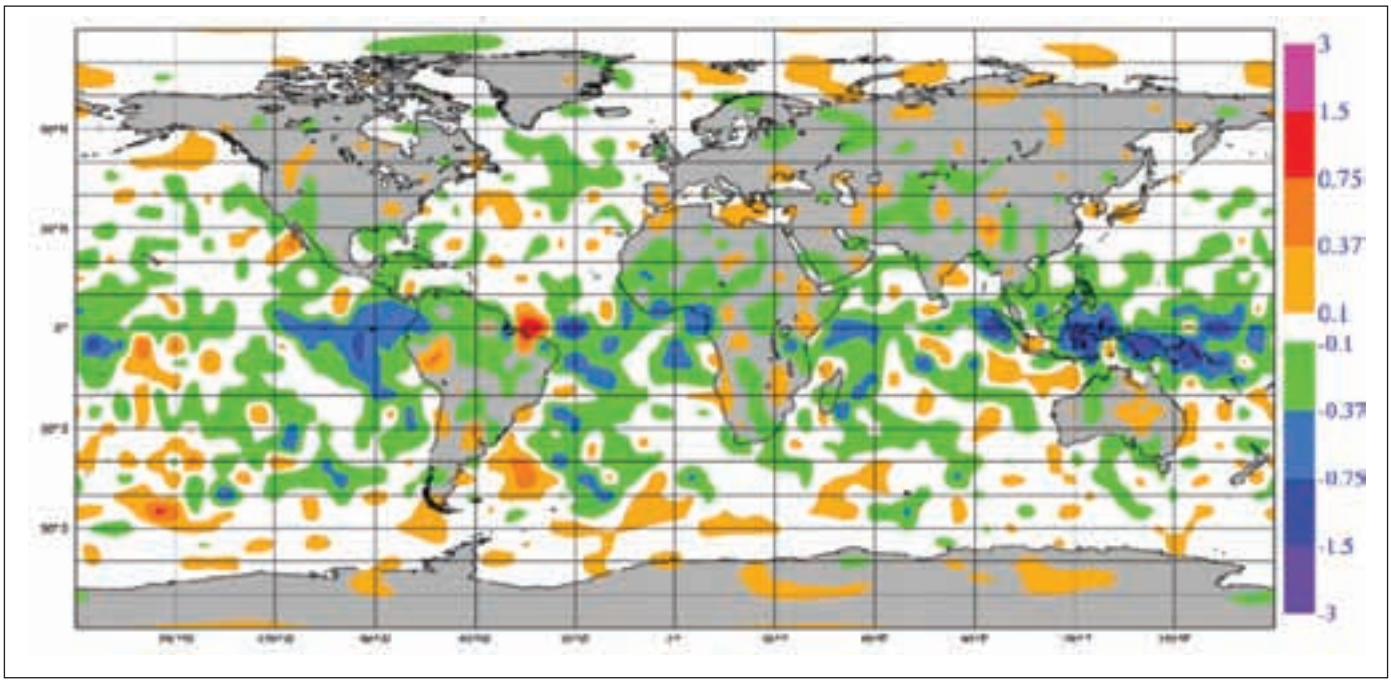

Fig. 7.7. Impact in terms of 200 hPa zonal wind component (m s^{-1}) of ADM-Aeolus wind profile data as deduced from the difference in data assimilation ensemble spread between two ensembles: Control and ADM-Aeolus. Green (orange) shading (see legend) indicates that the ensemble spread, i.e. the analysis error, is reduced (increased) using the ADM-Aeolus data. Shading in the range -0.1 to 0.1 is suppressed. Adopted from Tan and Andersson (2004).

AMSU-A) and humidity in the troposphere (AMSU-B, AIRS, HIRS, SSM/I, GOES, and Meteosat). The profiling observing systems that ADM-Aeolus can most usefully be compared with are represented by TEMP (radiosondes), PILOT (wind profiles) and AIREP (aircraft measurements) in the diagram. Using the method of Fisher (2003b), information content was computed for each of the experiments Control, ADM-Aeolus and 'No-Sonde', defined above. It was found that in terms of wind information in these experiments (Table 7.1), radiosondes plus wind profilers provide 3153 DFS and ADM-Aeolus 2454 DFS. These results are in keeping with the expected quantity, accuracy and coverage of the simulated ADM-Aeolus data. Unlike radiosondes, ADM-Aeolus contributes most of its information in regions that are currently poorly observed, i.e. over ocean regions in both hemispheres and throughout the tropics.

7.4 Aerosol and clouds

The ADM-Aeolus wind information is derived from the Doppler shift in the backscattered laser signal, whereas the signal strength is related to the encountered aerosol and cloud distributions (and molecules). A range of ADM-Aeolus ancillary data products on clouds and aerosol can therefore be envisaged, as detailed in Chapter 5. The separation between aerosol and cloud information can be performed through classification and thresholding algorithms. The main advantage of lidar (active) instruments in this context is that they can distinguish the multiple cloud and aerosol layers that typically exist in the atmosphere. Other (passive) satellite sensing techniques currently in use are limited to an integrated view all atmospheric layers. For reasons explained in Chapter 4, ADM-Aeolus will provide aerosol and cloud profiles with a 1 km vertical resolution throughout the troposphere and 500 m in the layers nearest ground, with intermittent along-track coverage due to its burst-mode operation.

The lidar cloud data shown in Fig. 7.10 (Palm *et al.*, 2005) have been obtained from the GLAS instrument (the Geoscience Laser Altimeter System) on the Ice, Cloud, and land Elevation Satellite (ICESat). It shows clouds along a northbound

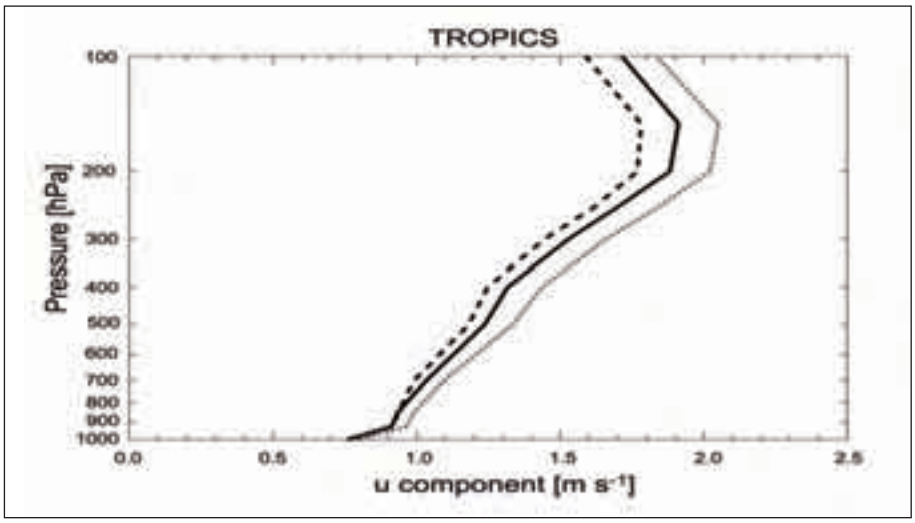

Fig. 7.8. East-west wind component (m/s) 12 h forecast errors, estimated from data assimilation ensembles, and averaged over a one-month period. The lines show results from three different data assimilation ensemble experiments: Control - the 2004 observing system (solid), 'No-Sonde' - radiosondes and wind profilers removed (dotted), and ADM-Aeolus - simulated ADM-Aeolus data added (dashed line). From Tan and Andersson (2004).

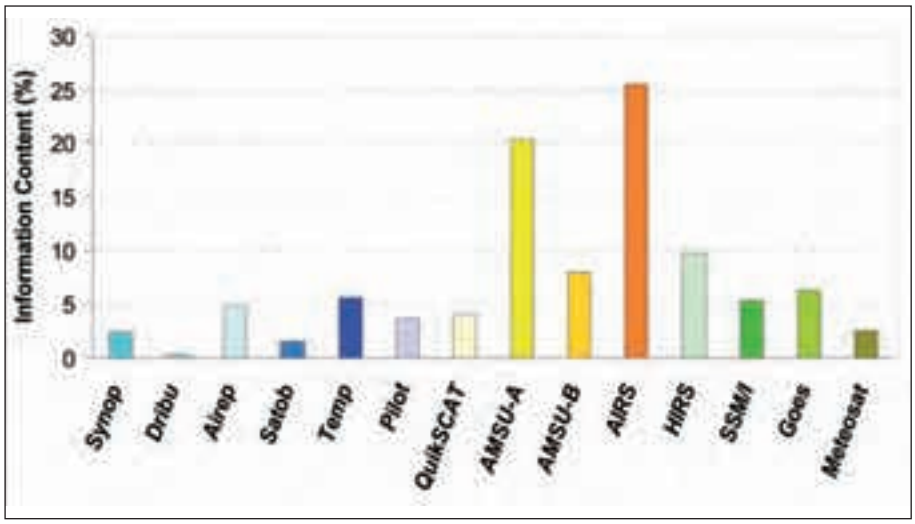

Fig. 7.9. Information content in each of the main components of the global observing system, in ECMWF's operational data assimilation system (from Cardinali *et al.*, 2004). Much of the information is obtained from satellite sounding data such as that from polar-orbiting instruments AMSU-A/B, AIRS, HIRS and SSMI and the geostationary GOES and Meteosat, and pertains largely to tropospheric humidity and stratospheric temperature. QuikSCAT is a polar-orbiting scatterometer instrument measuring surface wind speed over the ocean – for further explanations, see Chapter 2. It is expected that ADM-Aeolus will provide a contribution similar to that of the radiosonde network (labelled TEMP). This figure is reproduced/ modified by permission of The Quarterly Journal of the Royal Meteorological Society.

orbit from near Antarctica to the Canary Islands and has been overlaid with the 48-hour forecast cloud fraction (contoured) from the ECMWF model. The figure illustrates the utility of spaceborne lidar cloud-data for model validation. Systematic comparisons of this kind were done by Miller *et al*. (1999) using LITE data. Improved modelling of the vertical extent and position of clouds and cloud optical thickness is crucial for the modelling of radiative heating, which is an important component of the energy budget at the surface, in the atmosphere, and in the presence of clouds. This is an important aspect in climate modelling that seeks to estimate the effects of anthropogenic forcing on the climate system. Satellite lidars such as ADM-Aeolus can provide vertically resolved information that can help improve modelling of clouds and aerosol, and serve as validation.

The CALIPSO satellite, which is part of NASA's so called A-Train constellation of satellites (Stephens *et al*., 2002), carries a cloud- and aerosol-profiling lidar measuring at 532 and 1064 nm, with high vertical resolution. ADM-Aeolus can in some respects serve as a CALIPSO follow-on. An example of first lidar backscatter measurements from CALIPSO is shown in Fig. 7.11. Scene classification algorithms are applied to CALIPSO data to distinguish

Table 7.1. Information content in TEMP (radiosonde) and PILOT winds and ground-based wind profiler data from the surface to 55 hPa and in simulated ADM-Aeolus single line-of-sight data, in data assimilation experiments with the ECMWF 4D-Var system.

Data	*TEMP+PILOT winds to 55 hPa*	*ADM-Aeolus line of sight winds*
Number of data	74682	28979
DFS	3153	2454
Data per DFS	23.7	11.8

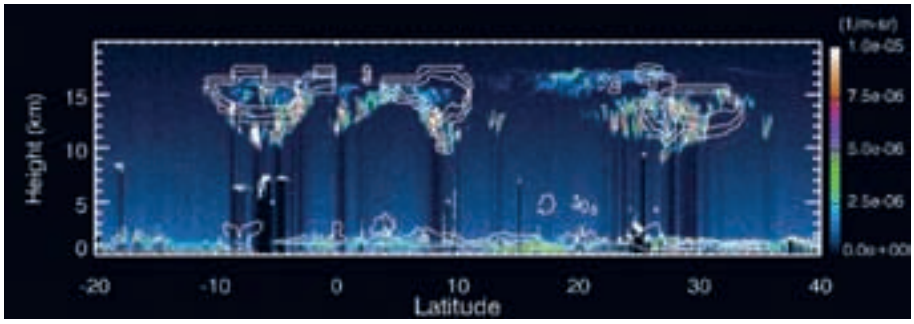

Fig. 7.10. Comparison between lidar cloud measurements from the GLAS instrument on the ICESat mission (colour shaded) and 48-hour forecast cloud fraction from the ECMWF model (contoured), for a northbound orbit (left to right) from near Antarctica to just north of the Canary Islands. From Palm *et al*. (2005). Copyright 2005 American Geophysical Union. Reproduced/modified by permission of American Geophysical Union.

clear-air, clouds and aerosol from ground-returns and data with insufficient signal-to-noise ratio. An exciting result from the CALIPSO "first light" measurements is the detection of volcanic aerosols from the eruption at the Caribbean Island Montserrat in May 2006.

The Global Monitoring for Environment and Security (GMES) joint initiative of the European Commission and ESA emphasises the importance of research on atmospheric composition and transport of pollution at regional and global scales. It identifies, for example, that enhanced monitoring of aerosol distributions is required for improved prediction of air quality. A capability for global monitoring of aerosol will be developed at ECMWF in the coming years, as a contribution to GMES. It is expected that ADM-Aeolus will be able to provide crucial information on the vertical distribution of aerosol along the satellite track. Passive remote sensing methods (imagers, such as AVHRR, MODIS, MISR and POLDER), on the other hand, can provide excellent horizontal coverage, but little, or no information on the vertical distribution.

Pure backscatter lidar approaches to aerosol retrieval are problematic due to ambiguities in separating backscatter and attenuation; it is only through combination of active and passive remote sensing data and physical models of aerosol evolution, sources and sinks, that some information on aerosol type and related parameters (such as size distribution, chemical composition and optical properties) can be deduced (Kahn *et al*., 2004). ADM-Aeolus, however, is the first high spectral resolution lidar in space capable of independently measuring attenuation and backscatter. ADM-Aeolus can get the two quantities because there are two channels measuring two independent quantities. The backscattering coefficient and the attenuation from the molecules can be accurately modelled (it depends on the temperature through a well known equation) - so there remain only two unknowns: the particle backscatter and attenuation coefficients.

7.5 Anticipated ADM-Aeolus impact - summary

An up-to-date summary of the impacts from the main current observation types over the northern and southern hemisphere extra-tropics and tropics has been compiled by WMO based on the results presented at the third WMO workshop on

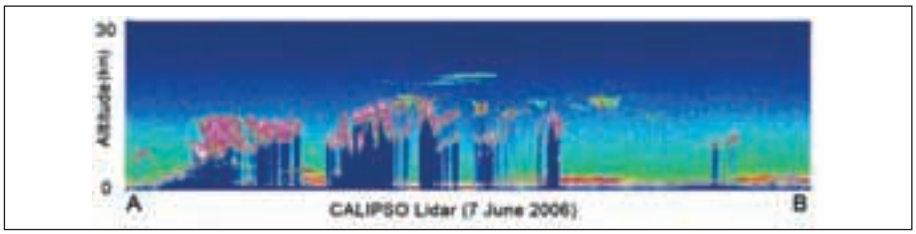

Fig. 7.11. A lidar profile from the CALIPSO spacecraft from 7 June 2006, specifically the 523 nm Total Attenuated Backscatter. The orbit covers eastern Asia, Indonesia and Australia. In the lower right corner changing surface elevation of the Australian continent can be seen. Just above the surface, a layer of aerosol particles is shown in shades of orange and red. The greenish-yellow and blue colours indicate the lidar signal reflected from air molecules. Thin tropical cirrus clouds are shown in greenish-blue, at a height of 12 to 15 km. At an altitude of about 20 km, a volcanic plume from the eruption of Soufriere, Montserrat in the Caribbean Sea on 20 May 2006 is seen. Credit: NASA Langley Research Center.

observation impact (WMO, 2004). Its summary table is reproduced here as Table 7.2. The results are expressed in terms of gain in large-scale forecast skill at short and medium-range. The gains have been assessed in observing system experiments by adding the observing system to all others used routinely in the assimilation. Since the number of observing systems routinely used varies considerably from centre to centre, this marginal gain may also vary considerably from one study to the other. The arrows indicate this range of impacts. It is implied that the magnitudes of the impact depend upon the model and assimilation scheme used, upon the impact variable and also the forecast range.

It is reasonable to expect that the future ADM-Aeolus data will show a similar range of impacts depending on the model and assimilation schemes in use, and on which other observing systems will be available for assimilation within the ADM-Aeolus time frame: 2008–2010. Current estimates indicate that ADM-Aeolus will provide similar amounts of information to an assimilation system as the global radiosonde observing system, in terms of DFS. Taking into account the geographical distribution of available wind information, and the expected yield of good-quality ADM-Aeolus data, it is expected that the main impact will be obtained over the oceans in both hemispheres, and in all regions of the tropics. This is generally supported by the available earlier OSSE results, briefly summarised in this chapter.

Table 7.2 shows that current NWP derives most benefit from radiosondes in the Northern Hemisphere and from satellite temperature sounding instruments, globally. In the coming years, additional second-generation satellite sounders with higher vertical resolution will become available, and will to a limited extent also indirectly contribute to the wind analysis accuracy. The scatterometer coverage and accuracy will improve, contributing to the lower-tropospheric wind analysis. It is thus expected that the need for global direct wind measurements will remain almost unchanged before the arrival of ADM-Aeolus. The studies performed with current state-of the-art data assimilation systems should therefore be relevant in anticipation of the real data. Improvements to data assimilation techniques may conceivably benefit some data types more than others but at present there is no reason to suspect that ADM-Aeolus data will benefit less than other observing systems from such work. In particular, improvements in the description of the background error covariances in the tropics and for the non-rotational part of the wind-error in mid-latitudes could further enhance the impact of the ADM-Aeolus single-component winds.

When trying to place the future ADM-Aeolus in the context of the WMO-table, we need to take the data distribution of the two observing systems into account. It is then reasonable to expect that ADM-Aeolus will have smaller impact than radiosondes in the northern Hemisphere extra tropics but larger impact in the Southern Hemisphere. In the tropics, where the need for direct wind measurement is the greatest, it is expected that ADM-Aeolus will show its biggest benefit.

Table 7.2. Summary of data impact. Current contributions of some parts of the existing observing system to the large-scale forecast skill at short and medium range. From WMO (2004).

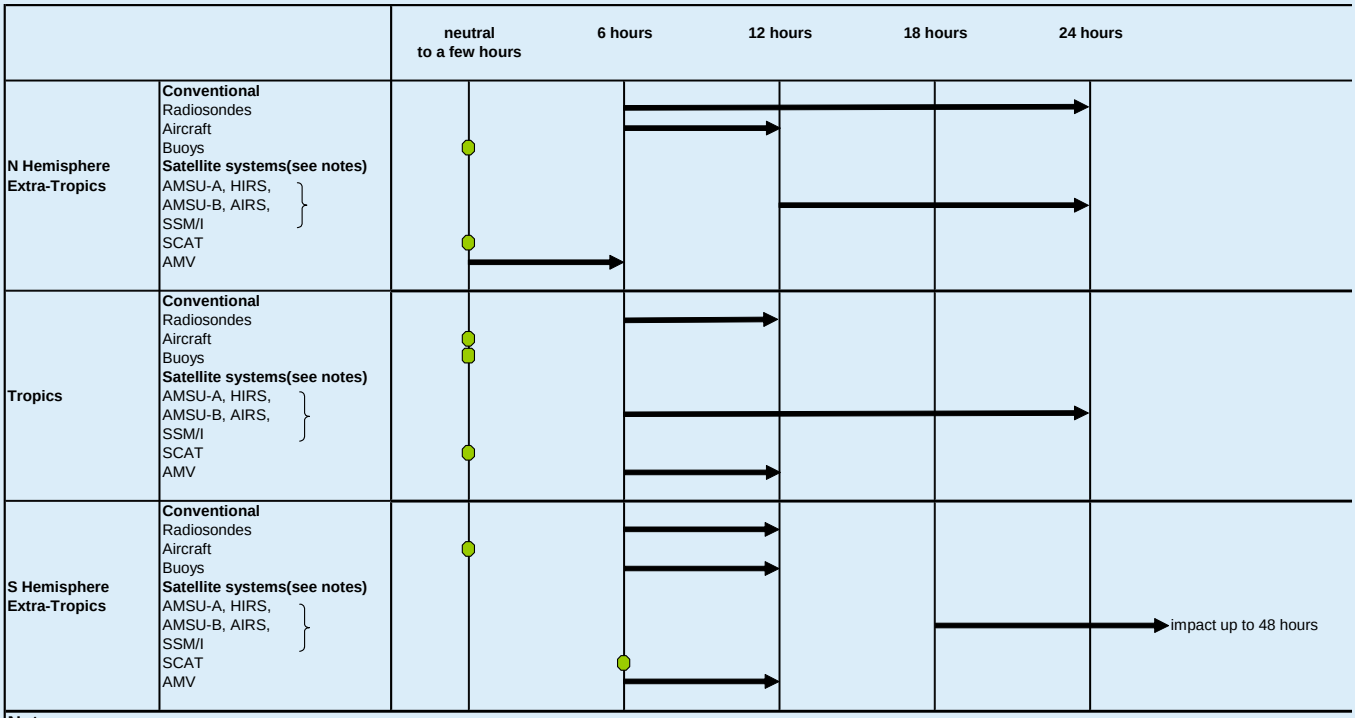

Notes:

1. SATELLITE SYSTEMS

AMSU-A.....The dominant and more largely used sub-system
HIRS.....Less important than AMSU-A, useful complement for humidity
AMSU-B.....Not used yet in many centres: important for humidity over land
AIRS.....Evaluation just starting (equivalent to one AMSU-A)
SSM/I.....Important impact on humidity fields (esp. tropics and SH)

2. OBSERVATION PARAMETER TYPE

Surf. Pressure Ps.....Important to anchor model Ps. (large model biases otherwise)
Surf. Wind.....Less important than Ps, useful complement (see SCAT)
Wind profiles.....…The more important information to observe, esp. in the tropics

3. EVOLUTION OF THE RELATIVE IMPACT OF VARIOUS OBSERVATION TYPES

Compared to results obtained at previous workshops
(i) ….…….The relative impact of satellite data has increased
(ii)……..…….Consequently, the relative impact of radiosonde data has decreased
(iii)……..……The impact of aircraft data has slightly increased

8. Conclusions and outlook

The Atmospheric Dynamics Mission, ADM-Aeolus, is currently being developed by the European Space Agency within its Living Planet Programme. ADM-Aeolus will demonstrate the capability of a spaceborne Doppler wind lidar to accurately measure wind profiles in the troposphere and the lower stratosphere (0–27 km). The mission thus contributes to resolving one of the main identified deficiencies of the current Global Observing System. From the backscattered, frequency-shifted laser light it will be possible to obtain about 3 000 globally distributed profiles of horizontal line-of-sight winds daily and with good vertical resolution. The accuracy of ADM-Aeolus winds, in most cloud-free regions and above thick clouds, is expected to be comparable to that of radiosonde wind measurements.

The ADM-Aeolus laser will emit a narrow linewidth, 355 nm pulse directed at a 35º-slant angle towards the atmosphere. The laser light is then backscattered by molecules (Rayleigh-Brillouin scattering) and aerosols (Mie scattering) from layers throughout the troposphere and the lower stratosphere. The strength of the return signal, and thus the quality of the derived wind, will depend on the cloudiness and, in the lower troposphere, also on the aerosol loading. In overcast situations, good quality wind observations will be obtained down to the cloud top. The mission also provides ancillary information on aerosol concentration and cloud top height.

The ADM-Aeolus wind profiles will find wide application in NWP and climate studies, improving the accuracy of numerical weather forecasting, advancing our understanding of tropical dynamics and processes relevant to climate variability and climate modelling. With a target launch date in late 2009, work has already been initiated preparing for the future realtime assimilation of ADM-Aeolus wind data into operational NWP models. At mid-latitude, the largest impact is expected on those regions where the forecast performance is known to be particularly sensitive to the accuracy of the initial conditions. In particular, a beneficial impact on the prediction of severe storm events is expected and further investigated. For the tropics, the focus of current investigations is on defining the appropriate mass/wind relationships for effective assimilation of the ADM-Aeolus wind data in state of the art data assimilation systems (e.g. Žagar *et al*., 2004 a, b; Žagar, 2004).

During its projected three-year lifetime, ADM-Aeolus will demonstrate the feasibility of global wind field measurement from space. Based on the results obtained with ADM-Aeolus, future operational missions may be built, fully exploiting the concept of spaceborne Doppler wind lidars.

References

ACIA, 2004: *Impacts of a Warming Arctic - Arctic Climate Impact Assessment*. Cambridge University Press, pp 144.

Andersson, E., J. Haseler, P. Undén, P. Courtier, G. Kelly, D. Vasiljevi, C. Brankovi, C. Cardinali, C. Gaffard, A. Hollingsworth, C. Jakob, P. Janssen, E. Klinker, A. Lanzinger, M. Miller, F. Rabier, A. Simmons, B. Strauss, J. N. Thépaut and P. Viterbo, 1998: The ECMWF implementation of three dimensional variational assimilation (3D-Var). Part III: Experimental results. *Quart. J. Roy. Meteor. Soc.*, 124, 1831–1860.

Andersson, E., P. Bauer, A. Beljaars, F. Chevallier, E. Hólm M. Janisková, P. Kållberg, G. Kelly, P. Lopez, A. McNally, E. Moreau, A. J. Simmons, J-N. Thépaut and A. M. Tompkins, 2005: Assimilation and modeling of the atmospheric hydrological cycle in the ECMWF forecasting system. *Bull. Amer. Meteor. Soc.*, 86, 387–402.

Arrhenius, S., 1896: On the influence of carbonic acid in the air upon the temperature of the ground. *The London, Edinburgh and Dublin Philosophical Magazine and Journal of Science*, 41, 237-276.

Astin, I. and C. Kiemle, 2003: Space-borne clear air lidar measurements in the presence of broken clouds. *Annales Geophysicae*, 21, 639–647.

Atlas, 1997: Atmospheric observations and experiments to assess their usefulness in data assimilation, *J. Meteor. Soc. Japan*, 75, 111–130.

Atlas, R. and G. D. Emmitt, 1991: Implications of several orbit inclinations for the impact of LAWS on global climate studies. *Proc 2nd Symp. on "Global Change Studies"*, New Orleans, LA, *Amer. Meteor. Soc*., 28–32.

Atlas, R., E. Kalnay, W. E. Baker, J. Susskind, D. Reuter and M. Halem, 1985: Observing system simulation experiments at GSFC. *Proc. NASA Symposium on "Global wind measurements"*, Columbia, MD, NASA, 65–71.

Atlas, R., G. D. Emmitt, J. Terry, E. Brin, J. Ardizzone, J. C. Jusem and D. Bungato, 2003: Recent observing system experiments at the NASA DAO. *Proc. AMS 7th Symposium on "Integrated Observing Systems"*, 9-13 February 2003, Long Beach, CA.

Baker, W. E. and co-authors, 1995: Lidar-Measured Winds from Space: A Key Component for Weather and Climate Prediction, *Bull. Am. Meteor. Soc.*, 76, 869–888.

Becker, B. D., H. Roquet and A. Stoffelen. 1996: A simulated future atmospheric observation database including ATOVS, ASCAT, and DWL, *Bull. Amer. Meteor. Soc.*, 77, 2279–2294.

Bengtsson, L., M. Ghil and E. Källén., 1981: *Dynamic Meteorology, Data assimilation methods.* Springer Verlag, pp s330.

Bengtsson L, K.I. Hodges and S. Hagemann , 2004: Sensitivity of large-scale atmospheric analyses to humidity observations and its impact on the global water cycle and tropical and extratropical weather systems in ERA40, *Tellus Series A*, 56, 202–217.

Bjerknes J and H. Solberg, 1922: Life cycle of cyclones and the polar front theory of atmospheric circulation. *Geof. Publ.*, 3, 1–18.

Bouttier, F. and G. Kelly, 2001: Observing-system experiments in the ECMWF 4D-Var data assimilation system. *Quart. J. Roy. Meteor. Soc.,* 127, 1469–1488.

Brandefelt, J., E. Källén, 2004: The response of the Southern Hemisphere atmospheric circulation to an enhanced greenhouse gas forcing. *J. Climate*, 17, 4425–4442.

Brink van den, H.W., G.P. Können and J.D. Opsteegh, 2004: Statistics of extreme synoptic-scale wind speeds in ensemble simulations of current and future climate, *J. Climate*, 17, 4564–4574.

Budyko, M.I. and Y. A. Izrael (editors) 1991: *Anthropogenic climate change*. The University of Arizona Press, Tucson (English translation of Russian original text), pp 485.

Carnell, R.E. and C.A. Senior, 1998: Changes in mid-latitude variability due to increasing greenhouse gases and sulfate aerosols. *Climate Dynamics*, 14, 369–383.

Cardinali, C., L. Isaksen and E. Andersson, 2003: Use and impact of automated aircraft data in a global 4D-Var data assimilation system. *Mon. Wea. Rev.*, 131, 1865–1877.

Cardinali, C., S. Pezzulli and E. Andersson, 2004: Influence matrix diagnostic of a data assimilation system. *Quart. J. Roy. Meteor. Soc,* 130, 2767–2786.

Centre National d'Etudes Spatiales, 1988: *BEST – scientific objectives and preliminary definition of a satellite mission dedicated to GEWEX and Global Change,* pp 58.

Cess, R.D. and co-authors, 1990: Intercomparison and interpretation of climate feedback processes in 19 atmospheric general circulation models. *J. Geophys. Res*., 95, 16601–16615.

Courtier, P., P. Gauthier, F. Rabier, P. Flamant, A. Dabas, F. Lieutaud, and H. Renault, 1992: Study of preparation for the use of Doppler wind lidar information in meteorological assimilation system*s*; *ESA-CR(P)-3453*, pp 82.

Courtier, P., E. Andersson, W. Heckley, J. Pailleux, D. Vasiljevic, M. Hamrud, A. Hollingsworth, F. Rabier and M. Fisher, 1998: The ECMWF implementation of three-dimensional variational assimilation (3D-Var). Part I: Formulation. *Quart. J. Roy. Meteor. Soc.* 124, 1783–1807.

Cress A. and W. Wergen, 2001: Impact of profile observations on the German Weather Service's NWP system, *Meteor. Z.*, 10, 91–101.

Cress A, and W. Wergen, 2002. Dynamical aspects of the life cycle of the winter storm 'Lothar' (24-26 December 1999). *Quart. J. Roy. Meteor. Soc*, 128 (580), 405–429 Part B, January 2002.

Daley R., 1991: *Atmospheric data analysis*. Cambridge University Press, Cambridge, UK, pp 460.

Delaval A., P. Flamant, C. Loth, A. Garnier, C. Vialle, D. Bruneau, R. Wilson, D. Rees, 2000 : *Valid 2 : Performances Validation of Direct Detection and Heterodyne Detection Doppler Wind Lidars*. ESA contract study report, TIDC-CR-7200, pp 82.

Delecluse, P., M.K. Davey, Y. Kitamura, S.G.H. Philander, M. Suarez and L. Bengtsson, 1998: Coupled general circulation modeling of the tropical Pacific. *J. Geophys. Res.,* 103, 14357–14373.

Douglass A.R., M.R. Schoeberl, R.B. Rood and S. Pawson, 2003: Evaluation of transport in the lower tropical stratosphere in a global chemistry and transport model, *J. Geophys., Res*., 108, Art. No. 4259.

Drobinski, P., R. A. Brown, P. H. Flamant, and J. Pelon, 1998: Evidence of organized large eddies by ground-based Doppler lidar, sonic anemometer and sodar, *Bound.-Layer Meteor.,* 88, 343–361.

Dumelow, R., 2003: Overview of observing system experiments. *Proc. ECMWF Seminar on "Recent Developments in Data Assimilation for Atmosphere and Ocean"*, 8–12 Sept 2003, Reading, U.K., 97–124.

Durand, Y., Chinal, E., Endemann, M., Meynart, R., Reitebuch, O., Treichel, R., 2006: ALADIN Airborne Demonstrator: a Doppler Wind Lidar to prepare ESA´s Aeolus Explorer Mission. *Proc. SPIE Optics and Photonics*, 6296, 13-17 August 2006, San Diego.

European Space Agency (ESA), 1989: ALADIN – Atmospheric Laser Doppler Instrument, Doppler Lidar Working Group, *ESA SP-1112,* pp 45.

European Space Agency (ESA), 1995: ESA Doppler Wind Lidar Workshop, 20-22 September 1995, ESTEC, Noordwijk, The Netherlands, *ESA WPP-05*, pp 312.

European Space Agency (ESA), 1996: Atmospheric Dynamics Mission, Reports for Assessment, *ESA SP-1196(4)*, pp 70.

European Space Agency (ESA), 1998: The Science and Research Elements of ESA's Living Planet Programme, *ESA SP-1227*, pp 105.

European Space Agency (ESA), 1999: Atmospheric Dynamics Mission, Reports for Selection, *ESA SP-1233(4),* pp 157.

Fisher, M., 2003a: Background error covariance modelling. *Proc. ECMWF Seminar on "Recent Developments in Data Assimilation for Atmosphere and Ocean"*, 8-12 Sept 2003, Reading, U.K., 45–64.

Fisher, M., 2003b: Estimation of entropy reduction and degrees of freedom for signal for large varaitional analysis systems. *ECMWF Tech. Memo.*, 397, pp 18.

Gibson, J.K., Kållberg, P., Uppala, S., Nomura, A., Hernandez, A., Serrano, E., 1997: ERA description. ECMWF re-analysis project report series, 1, 71pp. Available from ECMWF, Shinfield Park, Reading, Berks. RG2 9AX, England.

Gordon, C.T., L. Umscheid, L. and K. Miyakoda, 1972: Simulation experiments for determining wind data requirements in the tropics. *J. Atmos. Sci*., 29, 1064–1075.

Håkansson, M, 2001: *Determination of Atmospheric Wind Statistics. ESA-CR(P)-4329*, pp 23.

Hello, G., F. Lalaurette and J.-N. Thépaut, 2000: Combined use of sensitivity information and observations to improve meteorological forecasts: A feasibility study applied to the "Christmas Storm". *Quart. J. Roy. Meteor. Soc.*, 126, 621–647.

Hollingsworth, A. and P. Lönnberg, 1987: The statistical structure of short-range forecast errors as determined from radiosonde data. Part I: The wind field. Part II: The covariance of height and wind error, *Tellus*, 38A, 111–136 and 137–161.

Hólm, E., E. Andersson, A. Beljaars, P. Lopez, J-F. Mahfouf, A. J. Simmons and J.-N. Thépaut, 2002: Assimilation and modeling of the hydrological cycle: ECMWF's status and plans. *ECMWF Tech. Memo*., 383, pp 55.

Holton, J.R., P.H. Haynes, M.E. McIntyre, A.R. Douglass, R.B. Rood, and L. Pfister, 1995: Stratosphere-troposphere exchange, *Rev. of Geoph.*, 33 (4), 403–439.

Holton, J.R. 2004: *An introduction to dynamic meteorology* (fourth edition). Elsevier Academic Press, pp 535.

Ide K., P. Courtier, M. Ghil, and A.C. Lorenc, 1997. Unified notation for data assimilation: operational, sequential and variational. *J. Meteor. Soc. Japan*. 75, 1B, 181–189.

Ingmann, P., L. Isaksen, A. Stoffelen and G.-J. Marseille, 1999: On the Needs, Requirements and Feasibility of a Space-borne Wind Profiler, *Proc. of 'Fourth International Winds Workshop'*, EUMETSAT, *EUM P 24*, 199–206.

IPCC, 2001: *Climate Change 2001. The scientific basis*. Cambridge University Press, pp 881.

Jones, P. D. and Moberg, A., 2003 Hemispheric and large-scale surface air temperature variations : An extensive revision and update to 2001. *J. Climate*, 16, 206–223.

Kållberg, P., and S. Uppala, 1999: Impact of Cloud Motion Winds in the ECMWF ERA15 Reanalysis, *Proc. of 'Fourth International Winds Workshop',* Eumetsat, EUM P 24, 109–116.

Kahn, R. A. and Co-authors, 2004: Aerosol data sources and their roles within PARAGON. *Bull. Amer. Meteor. Soc.*, 85, 1511–1522.

Kalnay, E., Kanamitsu, M., Kistler, R., Collins, W., Deaven, D., Gandin, L., Iredell, M., Saha, S., White, G., Woollen, J., Zhu, Y., Chelliah, M., Ebisuzaki, W., Higgins, W., Janowiak, J., Mo, K.C., Ropelewski, C., Wang, J., Leetmaa, A., Reynolds, R., Jenne, R., and Joseph, D., 1996: The NCEP/NCAR 40 year re-analysis project. *Bull. Amer. Meteor. Soc*., 77, 437–471.

Kelly, G.A., 1997: Influence of observations on the Operational ECMWF System, *WMO Bulletin*, 46, 336–342.

Kistler, R., E. Kalnay, W. Collins, S. Saha, G. White, J. Wollen, M. Chelliah, W. Ebisuzaki, M. Kanamitsu, V. Kousky, H. van den Dool, R. Jenne and M. Fiorino, 2001: The NCEP-NCAR 50-year re-analysis: monthly means CD-ROM and documentation. *Bull. Amer. Meteor. Soc.*, 82, 247–267.

Köpp, F., S. Rahm, and I. Smalikho, 2004: Characterization of aircraft wake vortices by 2-μm pulsed Doppler lidar. *J. Atmos. Oceanic Technol.*, 21, 194–206.

Lahoz, W.A., R. Brugge, D.R. Jackson, S. Migliorini, R. Swinbank, D. Lary and A. Lee, 2005: An observing system simulation experiment to evaluate the scientific merit of wind and ozone measurements from the future SWIFT instrument. *Quart. J. Roy. Meteor. Soc.*, 131, 503–523.

Lim, H.-S. and Ho, C.-H., 2000: Comparison of Tropical Rainfall Between the Observed GPCP Data and the Assimilation Products of ECMWF, NCEP/NCAR, and NASA-GEOS-1. *J. Meteor. Soc. Japan,* 78, 661–672.

Lindzen, R., Chou, M-D. and A.Y. Hou, 2001: Does the Earth have an adaptive infrared iris? *Bull. Amer. Meteor. Soc*., 82, 417–432.

Liu, Z.-Q and F. Rabier, 2002. The interaction between model resolution, observation resolution and observation density in data assimilation: a one-dimensional study. *Quart. J. Roy. Meteor. Soc*., 128, 1367–1386.

Lorenc, A.C., 1986: Analysis methods for numerical weather prediction, *Quart. J. Roy. Meteor. Soc.,* 112, 1177–1194.

Lorenc, A.C., R.J. Graham, I. Dharssi, B. Macpherson, N.B. Ingleby and R.W. Lunnon, 1992: *Preparation for the use of Doppler wind lidar information in meteorological assimilation systems;* ESA-CR(P)-3454, pp 90.

Marseille, G.-J., A. Stoffelen, F. Bouttier, C. Cardinali, S. de Haan and D. Vasilijevic, 2001: *Impact assessment of a Doppler wind lidar in space on atmospheric analyses and numerical weather prediction.* Final Report of ESA Contract No 13018/98/NL/GD.

Marseille, G.-J. and A. Stoffelen, 2003: Simulation of wind profiles from a space-borne Doppler wind lidar. *Quart. J. Roy. Meteor. Soc*., 129, 3079–3098.

Masutani, M., S. J. Lord, J. S. Woolen, W. Yang, H. Sun, T. J. Kleespies, G. D. Emmitt, S. A. Wood, B. Katz, R. Treadon, S. Greco and J. Terry, 2004: Global OSSE at NCEP. *Proc AMS 8th Symposium on Integrated observing and assimilation system for atmosphere, ocean and land surface,* Seattle, 10-14 January 2004.
http://ams.confex.com/ams/84Annual/techprogram/paper_69441.htm.

McNally, A. P. 2002: A note on the occurrence of cloud in meteorologically sensitive areas and the implications for advanced sounders. *Quart. J. Roy. Meteor. Soc.*, 128, 2551–2556.

Menzies, Robert T., David M. Tratt, and William H. Hunt, 1998: Lidar In-space Technology Experiment measurements of sea surface directional reflectance and the link to surface wind speed, *Appl. Optics*, 37, (24), 5550–5559.

Meteorological Society of Japan, 1997: Special Issue on 'Data Assimilation in Meteorology and Oceanography: Theory and Practice', *J. Meteor. Soc. Japan*, 75, No.1B.

Miller, S. D., G. L. Stephens and A. C. M. Beljaars, 1999: A validation of the ECMWF prognostic cloud scheme using LITE. *Geophys. Res. Lett.*, 26, 1417–1420.

Minschwaner, K., and A.E. Dessler, 2004: Water vapor feedback in the tropical upper troposphere: Model results and observations, *J. Climate*, 17, 1272–1282.

National Aeoronautical and Space Administration (NASA), 1987: LAWS – laser atmospheric wind sounder, Instrument Panel Report, *Earth Observing System* Volume IIg, NASA TM 86129.

Neisser, J., W. Adam, F. Beyrich, U. Leiterer, H. Steinhagen, 2002: Atmospheric boundary layer monitoring at the Meteorological Observatory Lindenberg as a part of the 'Lindenberg Column': Facilities and selected results. *Meteor. Z.* 11, 241–253.

Nielsen, N.W. and B.H. Sass, 2003: A numerical, high-resolution study of the life cycle of the severe storm over Denmark on 3 December 1999, *Tellus,* 55, 338–351.

Noda, A., K. Yoshimatsu, S. Yukimoto, K. Yamaguchi, and S. Yamaki, 1999: Relationship between natural variability and CO_2 -induced warming pattern: MRI AOGCM Experiment. *10th Symposium on Global Change Studies* , 10-15 January 1999, Dallas, Texas. American Meteorological Society, Boston. Mass, pp 359–362

Paffrath, U., 2006: *Performance assessment of the Aeolus Doppler wind lidar prototype.* DLR Forschungsbericht 2006-12, ISSN 1434-8454,138 p.

Palm, S.; A. Benedetti, J. Spinhirne, 2005: Validation of ECMWF global forecast model parameters uing GLAS atmospheric channel measurements, *Geophys. Res. Lett.*, 32, L22S09, doi: 10.1029/2005/GL023535

Pierrehumbert, R.T. and R. Roca, 1998: Evidence for control of Atlantic subtropical humidity by large scale advection. *Geophys. Res. Lett*., 25, 4537–4540.

Räisänen, J., 2001: CO_2 -induced climate change in CMIP2 experiments. Quantification of agreement and role of internal variability. *J. Climate*, 14, 2088–2104.

Rabier, F., A. McNally, E. Andersson, P. Courtier, P. Undén, J. Eyre, A. Hollingsworth and F. Bouttier, 1998: The ECMWF implementation of three dimensional variational assimilation (3D-Var). Part II: Structure functions. *Quart. J. Roy. Meteor. Soc.*, 124, 1809–1829.

Randel W.J., R.R. Garcia RR and F. Wu, 2002: Time-dependent upwelling in the tropical lower stratosphere estimated from the zonal-mean momentum budget, *J. Atmos. Sci*, 59, 2141–2152.

Reitebuch O., C. Werner, I. Leike, P. Delville, P. Flamant, A. Cress, D. Engelbart, 2001: Experimental validation of wind profiling performed by the airborne 10-µm heterodyne Doppler lidar WIND, *J. Atmos. Oceanic Technol.*, 18, 1331–1344.

Reitebuch, O., Volkert, H., Werner, Ch., Dabas, A., Delville, P., Drobinski, Ph., Flamant, P. H., Richard, E., 2003: Determination of air flow across the Alpine ridge by a combination of airborne Doppler lidar, routine radio-sounding and numerical simulation, *Quart. J. Roy. Meteor. Soc.* 129, 715–728.

Reitebuch, O., Chinal, E., Durand, Y., Endemann, M., Meynart, R., Morancais, D., Paffrath, U., 2004: Development of an airborne demonstrator for ADM-Aeolus and campaign activities. *22nd Int. Laser Radar Conference (ILRC 2004)*, Matera, Italy, ESA SP-561, 1007–1010.

Riishøjgaard, L. P., R. Atlas and G. D. Emmitt, 2004: The Impact of Doppler Lidar Wind Observations on a Single-Level Meteorological Analysis. *J. Appl. Meteorol.*, 43, 810–820.

Rodgers, C.D., 1976. Retrieval of atmospheric temperature and composition from remote measurements of thermal radiation. *Rev. of Geophys.*, 14, 4, 609–624.

Rohalty, G. D. and T. N. Krishnamurti, 1993: An observing system simulation experiment for the Laser Atmospheric Wind Sounder (LAWS). *J. Appl. Meteor.*, 32, 1453–1471.

Schoeberl M. R., A. R. Douglass, Z. Zhu, and S. Pawson, 2003: A comparison of the lower stratospheric age spectra derived from a general circulation model and two data assimilation systems. *J. Geophys. Res.*, 108 (D3), 4113.

Simmons A.J. and A. Hollingsworth, 2002. Some aspects of the improvement in skill of numerical weather prediction. *Quart. J. Roy. Meteorol. Soc*, 128, 647–677.

Slingo J.M., and A. Slingo, 1988: The response of a general circulation model to cloud long-wave radiative forcing. I: Introduction and initial experiments. *Quart. J. Roy. Meteorol. Soc.*, 114, 1027–1062.

Souprayen C., A. Garnier, A. Hertzog, A. Hauchecorne, and J. Porteneuve, 1999a: Rayleigh-Mie Doppler wind lidar for atmospheric measurements. I. Instrumental setup, validation, and first climatological results. *Appl. Optics*, 38, 2410–2421.

Souprayen C., A. Garnier, and A. Hertzog, 1999b: Rayleigh–Mie Doppler wind lidar for atmospheric measurements. II. Mie scattering effect, theory, and calibration. *Appl. Optics*, 38, 2422–2431.

Steinhagen, H., J. Dibbern, D. Engelbart, U. Görsdorf, V. Lehmann, J. Neisser, J. Neuschaefer, 1998: Performance of the first Euopean 482 MHz Wind Profiler Radar with RASS under operational conditions. *Meteor. Z.,* 7, 248–261.

Stephens, G. L. and Co-authors, 2002: The CLOUDSAT mission and the A-Train. *Bull. Amer. Meteor. Soc.*, 83, 1771–1790.

Stoffelen, A., 1998: *Scatterometry,* Thesis Utrecht University, ISBN 90-393-1708-9.

Stoffelen, A. and G.-J. Marseille, 1998: *Study on the utility of Doppler wind lidar for numerical weather prediction and climate.* ESA-CR(P)-4198, pp 56.

Stoffelen, A., P. Flamant, M. Håkansson, E. Källén, G.-J. Marseille, J. Pailleus, H. Schyberg and M. Vaughan, 2002: *MERCI – Measurement Error and Correlation Impact on the Atmospheric Dynamics Mission,* Final Report of ESA Contract No 15192/01/NL/MM.

Stoffelen, A., J. Pailleux, E. Källén, J. M. Vaughan, L. Isaksen, P. Flamant, W. Wergen, E. Andersson, H. Schyberg, A. Culoma, R. Meynart, M. Endemann and P. Ingmann, 2005a: The atmospheric dynamics mission for global wind measurement. *Bull. Amer. Meteor. Soc.*, 86, 73–87.

Stoffelen, A., G.-J. Marseille, E. Andersson and D. G. H. Tan, 2005b: Comments on "The Impact of DWL Observations on a Single-Level Meteorological Analysis" by L. P. Riishøjgaard, R. Atlas, and G. D. Emmitt. *J. Appl. Meteor,* 44*,* 1276–1277

Stoffelen, A., G.-J. Marseille, F. Bouttier, D. Vasiljevic, S. de Haan, and C. Cardinali, 2006: ADM-Aeolus Doppler wind lidar Observing System Simulation Experiment. *Quart. J. Roy. Meteor. Soc.,* 132, 1927–1947.

Tan, D. G. H. and E. Andersson, 2004: *Expected benefit of wind profiles from the ADM-Aeolus in a data assimilation system.* Final Report for ESA contract 15342/01/NL/MM. Available from ESA. pp 62.

Tan, D. G. H. and E. Andersson, 2005: Simulation of the yield and accuracy of wind profile measurements from the Atmospheric Dynamics Mission (ADM-Aeolus), *Quart. J. Roy. Meteor. Soc.,* 131, 1737–1757.

Timmermann, A., J. Oberhuber, A. Bacher, M. Esch, M. Latif, and E. Roeckner, 1999: Increased El Niño frequency in a climate model forced by future greenhouse warming. *Nature*, 398, 694–696.

Uppala, S. M. *et al.*, 2005: The ERA-40 re-analysis, *Quart. J. Roy. Meteor. Soc.,* 131, 2961–3012.

Vaughan, J. M., D. W. Brown, C. Nash, C. B. Alejandro, and G. G. Koenig, 1995: Atlantic atmospheric aerosol studies 2. Compendium of airborne backscatter measurements at 10.6 μm. *J. Geophys. Res.*, 100, 1043–1065.

Veldman, S. M., A. Stoffelen, G. J. Marseille, J. van Es, H. A. Knobhout and E. A. Kuijpers, 1999: *Lidar Performance Analysis Simulator (LIPAS)*, ESA CR(P)-4290, pp 50.

Walser, A., D. Luthi and C. Schar, 2004: Predictability of precipitation in a cloud-resolving model, *Mon. Wea. Rev.*, 132, 560–577.

Weissmann, M., Busen, R., Dörnbrack, A., Rahm, S., Reitebuch, O., 2005: Targeted Observations with an Airborne Wind Lidar. *J. Atmos. Oceanic Technol.*, 22, 1706–1719.

Weissmann, M.; C. Cardinali (2007): Impact of airborne Doppler lidar observations on ECMWF forecasts, *Quart. J. Roy. Meteorol. Soc.*, 133, 107–116.

Werner C., P.H. Flamant, O. Reitebuch, C. Loth, F. Köpp, P. Delville, J. Streicher, P. Drobinski, S. Rahm, B. Romand, E. Nagel, C. Boitel, M. Kleir, D. Bruneau, H. Herrmann, A. Dabas, 2001: WIND Instrument. *Opt. Eng.*, 40, 115–125.

Wernli, H., S. Dirren, M.A. Liniger and M. Zillig, 2002: Dynamical aspects of the life cycle of the winter storm 'Lothar' (24-26 December 1999), *Quart. J. Roy. Meteor. Soc.*, 128, 405–429.

Wheeler, M. and Kiladis, G. N., 1999: Convectively coupled equatorial waves: analysis of clouds and temperature in the wavenumber-frequency domain, *J. Atmos. Sci.,* 56, 374–399.

Winker, D. M., Couch, R. H., and McCormick, M. P., 1996: An overview of LITE: NASA's Lidar In-space Technology Experiment, *Proc. IEEE*, 84, 2, 164–180.

World Meteorological Organisation (WMO), 1996: *Guide to Meteorological Instruments and Methods of Observation,* 6th edition, WMO-No. 8, Secretariat of the World Meteorological Organisation, Geneva, Switzerland.

World Meteorological Organisation (WMO), 2002: Statement of Guidance How Well Satellite Capabilities Meet WMO User Requirements in Several Application Areas. *WMO Satellite Reports SAT-26,* WMO/TD No. 1052.

World Meteorological Organisation (WMO), 2003: *Affiliate and CEOS Member Requirements. Mission and Instrument Database* (CD-ROM). Version 2.5, February 2003.

World Meteorological Organisation (WMO), 2004: *Proceedings of the 'Third WMO Workshop on the Impact of various observing systems on Numerical Weather Prediction',* WMO/TD No. 1228, pp 329.

Yang, G.-Y., B.J. Hoskins and J. Slingo, 2003: Convectively coupled equatorial waves: A new methodology for identifying wave structures in observational data, *J. Atmos. Sci.*, 60, 1637–1654.

Žagar, N., 2004: Assimilation of equatorial waves by line of sight wind observations. *J. Atmos. Sci.*, 61, 1877–1893.

Žagar, N., Gustafsson, N. and Källén, E., 2004a: Dynamical response of equatorial waves in a variational data assimilation. *Tellus*, 56A, 29–46.

Žagar, N., Gustafsson, N. and Källén, E.,2004b: Variational data assimilation in the tropics: the impact of a background error constraint. *Quart. J. Roy. Meteor. Soc.*, 130, 103–125.

Žagar, N., E. Andersson and M. Fisher, 2005: Balanced tropical data assimilation based on study of equatorial waves in ECMWF short-range forecast errors. *Quart. J. Roy. Meteor. Soc.* 131, 987–1011.

Acronyms and abbreviations

A2D	ALADIN Airborne Demonstrator
ADM-Aeolus	Atmospheric Dynamics Mission - Aeolus
ADMAG	ADM-Aeolus Mission Advisory Group
AC01	Aeolus Airborne Campaign 1
AC02	Aeolus Airborne Campaign 2
ACAR	Aircraft Communication Addressing and Reporting system
ACG	Aeolus Ground Campaign
ACIA	Arctic Climate Impact Assessment
AIREP	WMO Code for Aircraft Report
AIRS	Atmospheric Infrared Sounder
ALADIN	Atmospheric Laser Doppler Instrument
AMDAR	Aircraft Meteorological DAta Relay
AMSU-A	Advanced Microwave Sounding Unit - A
AMSU-B	Advanced Microwave Sounding Unit - B
AMV	Atmospheric Motion Vector
AOCS	Attitude and Orbit Control System
AOGCM	Atmosphere-Ocean General Circulation Model
APF	Aeolus Processing Facility
ARPEGE	Action de Recherche Petite Echelle Grande Echelle (French climate model)
AVHRR	Advanced Very High Resolution Radiometer
BC	Before Christ
BEST	Bilan Energétique du Système Tropical
BRC	Basic Repeat Cycle
CALIPSO	Cloud-Aerosol Lidar and Infrared Pathfinder Satellite Observation
CCD	Charged-Coupled Device
CMW	Cloud Motion Winds
CNES	Centre National d'Etudes Spatiales
CNRS	Centre National de la Recherche Scientifique
DC DDL	Dual Channel Direct Detection Lidar
DE	Double Edge
DFS	Degrees of Freedom for Signal
DLR	Deutsches Zentrum für Luft- und Raumfahrt
DLR-IPA	DLR - Institut für Physik der Atmosphäre
Dnepr	Russian/Ukrainian launcher
DWD	Deutscher Wetter Dienst
DWD-MOL	DWD - Meteorologisches Observatorium Lindenberg
DWL	Doppler Wind Lidar
ECMWF	European Centre for Medium-range Weather Forecasts
ERA	ECMWF Reanalysis
ERA15	ECMWF 15-years Re-analysis
ERA40	ECMWF 40-years Re-analysis
ERS	European Remote-sensing Satellite
ESA	European Space Agency
ESOC	European Space Operations Centre
FI DDL	Fringe Imaging Direct Detection Lidar
FOV	Field-Of-View
FWHM	Full-Width at Half-Maximum
GLAS	Geoscience Laser Altimeter System
GLOW	Goddard Lidar Observatory for Winds
GMES	Global Monitoring for Environment and Security
GOES	Geostationary Operational Environmental Satellites
GOS	Global Observing System

GPS	Global Positioning System
HDL	Heterodyne Doppler Lidar
HIRS	High resolution Infrared Radiation Sounder
HLOS	Horizontal Line-Of-Sight
ICESat	Ice, Cloud, and land Elevation Satellite
IPY	International Polar Year
ISS	International Space Station
ITCZ	Inter-Tropical Convergence Zone
L1	Level 1
L1A	Level 1A
L1B	Level 1B
L2	Level 2
L2B	Level 2B
L2C	Level 2C
LAWS	Laser Atmospheric Wind Sounder
Level 2/PF	Level 2 Processing Facility
LIDAR	LIght Detection And Ranging
LIPAS	LIdar Performance Analysis Simulator
LITE	Lidar-In-space Technology Experiment
LOS	Line-Of-Sight
MC	Multi-Channel
MERIS	MEdium Resolution Imaging Spectrometer
Meteosat	Meteorological Satellite
MIM	Munich Institute of Meteorology
MISR	Multiangle Imaging SpectroRadiometer
MODIS	MODerate resolution Imaging Spectroradiometer
MSLP	Mean Sea Level Pressure
NASA	National Aeronautics and Space Administration
NASA-GSFC	NASA – Goddard Space Flight Center
NCAR	National Center for Atmospheric Research
NCEP	National Center for Environmental Prediction (USA)
NESDIS	National Environmental Satellite, Data and Information Service
NH	Northern Hemisphere
NOAA	National Oceanic and Atmospheric Administration
NWP	Numerical Weather Prediction
OSE	Observation System Experiment
OSSE	Observation System Simulation Experiment
PBL	Planetary Boundary Layer
PDF	Probability Density Function
P_{ge}	Probability of gross error
PILOT	WMO Code for Conventional Wind Sounding
PLH	Power Laser Head
PLL	Phase Lock Loop
POLDER	POLarization and DirEctionality of Reflectances
QC	Quality Control
QuickSCAT	Quick Scatterometer
RASO	RAdio SOundings
RASS	Radio Acoustic Sounding System
RMS	Root Mean Square
Rockot	Russian launcher
S/C	SpaceCraft
SH	Southern Hemisphere
SNR	Signal-to-Noise Ratio

SSM/I	Special Sensor Microwave / Imager
tbd	to be determined
TEMP	WMO Code for Conventional Wind, Temperature and Humidity Sounding
TT&C	Telemetry, Tracking and Command
UTC	Universal Time Coordinated
UV	Ultra-Violet
VALID 2	Performance VAlidation of direct detection and heterodyne detection Doppler LIDars campaign
Vega	European launcher
V_{HLOS}	line-of-sight wind speed estimation
V_S	search-window wind speed range
V_{true}	true mean speed
WIND	Wind INfrared Doppler lidar
WMO	World Meteorological Organisation
WWW	World Weather Watch
σ_{LOS}	standard deviation of the LOS wind speeds
3D-Var	Three-Dimensional VARiational analysis
4D-Var	Four-Dimensional VARiational data assimilation

European Space Agency
Agence spatiale européenne

ESA Communication Production Office
ESTEC, PO Box 299, 2200 AG Noordwijk, The Netherlands
Tel. +31 71 565-3408 Fax +31 71 565-5433